Physics of Failure as a Technology Enabler for Electrical Machines in Transportation

Reliability-Oriented Design of Low Voltage Insulation Systems



Vincenzo Madonna

Power Electronics, Machines and Control Group

University of Nottingham

This Thesis is submitted for the degree of

Doctor of Philosophy

Nottingham April 2020

I would like to dedicate this Thesis to my family.

Declaration

I hereby declare that the contents of this Thesis are original. The presented material is the result of my own work, carried out under the guidance and supervision of Dr. Paolo Giangrande, Prof. Michael Galea and Prof. Chris Gerada.

Vincenzo Madonna

April 2020

Acknowledgements

This work was funded by the INNOVATIVE doctoral programme. The INNOVATIVE programme is partially funded by the Marie Curie Initial Training Networks (ITN) action (project number 665468) and partially by the Institute for Aerospace Technology (IAT) at the University of Nottingham.

This work was also supported by the University of Nottingham's Propulsion Futures Beacon.

Abstract

In modern electrical machines there is an-ever-increasing push towards high power density and efficiency, which are thus considered as main design objectives. On the other hand, electrical machines used in certain applications, such as in the transport industry, are also required to be highly reliable and robust. In order to achieve the much needed power density performances, “extra” stresses are being experienced by the insulation systems of these machines, often resulting in accelerated components degradation and compromised system-level reliability figures. In general, the lifetime consumption evaluation and the reliability assessment of electrical machines components, including the insulation system, are still evaluated through outdated methods. These are often based on historical data and adopt constant failure rates, derived by statistically post-processing the failure times of a large number of built prototypes. This is of course a very time-consuming and expensive process. In application fields such as automotive and aerospace, the reliability assessment procedures can then negatively affect the development timeline of an electrical product, especially for certification.

This Thesis therefore argues for the development of new processes, based on comprehensive physics of failure methodologies, for assessing the lifetime consumption and degradation of insulation systems for electrical machines. This will enable the electrical machine designer to make reliability considerations a main design objective, right from the very start of the design process. As a result of this work, this Thesis also shows how the proposed advanced philosophy will allow manufacturers to design insulation systems without relying on outdated, traditional “safety factors” and over-engineering concepts.

The proposed processes focus on the development of new lifetime prediction models for electrical machines. The core of the Thesis is focused on thermal considerations and stresses. The novel models, developed in this work, seek to achieve significant improvements in terms of accuracy of lifetime prediction, by combining the cumulative damage law with the conventional Arrhenius model. The Thesis also includes considerations on partial discharges and ensuing insulation electrical stresses.

Contents

Contents

Contents xi
List of Figures xv
List of Tables xix
Nomenclature xxi
List of Publications xxv
Chapter 1 Introduction 1
1.1 Transportation Electrification 1
1.2 Towards Reliability-Oriented Design of Electrical Machines 3
1.3 Fault-Tolerant Electrical Machines 5
1.4 Reliability of Electrical Machines 7
1.5 Main Contributions of the Thesis 8
1.6 Thesis Outline 9
1.7 Concluding Remarks 10
Chapter 2 Thermal and Electrical Aging in Low Voltage EMs Insulation 11
2.1 Overview of Insulation Stress Factors 11
2.2 Thermal Aging 14
2.3 Extrinsic Electric Stress 17
2.4 Concluding remarks 23
Chapter 3 Thermal Modelling of Electrical Machines 25
3.1 Lumped Parameter Thermal Network 25
3.2 Thermal Model of a Natural Air Cooled Motor 28
3.2.1 The case-study motor 28
3.2.2 Modelling with natural air cooling 30
3.2.3 LPTN fine-tuning 34
3.2.4 Considerations an limits of the LPTN 38
3.3 Thermal Model of a Liquid Cooled Traction Motor 40
3.3.1 The machine at hand 40
3.4 Concluding remarks 46
Chapter 4 Thermal Aging in Continuous Duty Electrical Machines 48
4.1 Problem Definition 49

4.2 Thermal Accelerated Aging Tests at Constant Temperature 49
4.2.1 Specimens Description 50
4.2.2 Test Campaign Description 53
4.2.3 Test Campaign Results 56
4.2.4 Discussion 61
4.2.5 Arrhenius Plot: Conventional Approach 64
4.2.6 Arrhenius Plot: Weibull Distribution Evaluation at the Design Temperature 66
4.3 Case-Study: Aerospace Environmental Control System 69
4.4 Concluding Remarks 73
Chapter 5 Insulation Thermal Aging in Variable Duty Electrical Machines 75
5.1 Problem Statement 75
5.2 Proposed Lifetime Prediction Model 77
5.3 Experimental Validation 82
5.3.1 Test Setup Description 82
5.3.2 Aging temperature profiles definition and end of life 83
5.3.3 Results and Discussion 86
5.4 Case-Study: Helicopter Actuator 90
5.5 Case-Study: Traction Motor 94
5.6 Case-Study: Propulsion Motor for UAV 98
5.6.1 Mission profile and reliability constraint 99
5.6.2 Conventional Design Approach 100
5.6.3 Physics of Failure – Based Design Approach 102
5.7 Concluding Remarks 107
Chapter 6 Partial Discharges in Low Voltage Electrical Machines 109
6.1 Problem Statement 109
6.2 Power Electronics and Electrical Machines Insulation 110
6.3 Insulation Sub-Systems Analysis 114
6.3.1 Premise on the Paschen's law 115
6.3.2 Turn to Turn Insulation 116
6.3.3 Phase to Phase Insulation 118
6.3.4 Phase to Ground Insulation 119
6.4 Experimental Validation 120
6.4.1 Indirect PDIV Measurement in Low Voltage EMs 120
6.4.2 Turn to Turn PDIV Measurement 126

6.4.3 Phase to Phase PDIV Measurement 131
6.4.4 Phase to Ground PDIV Measurement 133
6.5 Case-Study: Rail Traction Motor 135
6.6 Concluding Remarks 139
Chapter 7 Conclusions and Future Work 141
7.1 Summary 141
7.1.1 Thermal Analysis of Electrical Machines 141
7.1.2 Thermal and Thermally-Induced Insulation Stress 142
7.1.3 Partial Discharges 143
7.2 Main Achievements and Recognition 143
7.3 Future Work 144
References 147

List of Figures

Figure 1.1 – Evolution of electrical power need (grey: short- to medium-range aircraft and black: medium- to long-range aircraft). 2

Figure 1.2 – Insulation sub-systems in a typical low voltage EM [32]. 5

Figure 1.3 – Double three-phase drive architecture and power segmentation approach. 6

Figure 1.4 – Thesis structure and link among Chapters. 10

Figure 2.1 – Paschen's curve for air. 18

Figure 2.2 –Single period of the phase to phase voltage waveform in a PWM-fed EM (qualitative representation) [71]. 19

Figure 3.1 – Geometry and winding layout of a PMSM for EMA applications. 28

Figure 3.2 – LTPN representing $1/12^{th}$ of the PMSM for EMA applications. 30

Figure 3.3 – Circumferential heat path in the stator back iron. 31

Figure 3.4 – Simplified slot shape. 32

Figure 3.5. Volumetric iron loss distribution for the EMA PMSM operating at rated condition. 34

Figure 3.6 – Experimental setup for the LPTN fine tuning. 36

Figure 3.7 – Comparison between measured and estimated winding temperature profiles at different current levels. 38

Figure 3.8 – Geometry of the traction PMSM. 41

Figure 3.9 – End-winding cooling through liquid-carrying pipe. 42

Figure 3.10 – Complete hydraulic circuit of the traction PMSM. 42

Figure 3.11 – 7-Nodes LPTN of the traction PMSM. 43

Figure 3.12 – Instrumented motorette used for the traction motor's LPTN tuning/validation. 45

Figure 3.13 – Measured vs. LPTN-predicted hot-spot temperature profiles for slot (s) and end-winding (ew). 45

Figure 4.1 – Specimens used for the thermal accelerated lifetime tests. 51

Figure 4.2 – Thermal endurance plot of the used magnet wire (manufacturer). 51

Figure 4.3 – Motorette's winding layout. 52

Figure 4.4 – Flow-chart of the testing campaign. 54

Figure 4.5 – Weibull probability plot of failure times for twisted pairs aged at 250 °C (top sub-plot), 270 °C (middle sub-plot) and 290 °C (bottom sub-plot). 58

Figure 4.6 – Weibull probability plot of failure times for coils aged at 250 °C (top sub-plot), 270 °C (middle sub-plot) and 290 °C (bottom sub-plot). 59

Figure 4.7 – Weibull probability plot of failure times for motorettes at 250 °C (top sub-plot), 270 °C (middle sub-plot) and 290 °C (bottom sub-plot). 60

Figure 4.8 – Size effect sensitivity analysis for scale factor computation at 250 °C... 62

Figure 4.9 – Size effect sensitivity analysis for scale factor computation at 270 °C... 62

Figure 4.10 - Size effect sensitivity analysis for scale factor computation at 290 °C. 63

Figure 4.11 – Arrhenius plot (thermal endurance curve) for the coils specimens. 65

Figure 4.12 – Weibull plot of the accelerated thermal aging data (coils specimens). . 67

Figure 4.13 – Parallel Weibull fit of the accelerated thermal aging data (coils specimens)..... 67

Figure 4.14 –Arrhenius plot for coils specimens reporting three percentiles of failure time. 68

Figure 4.15 –30 kW PMSM for ECS compressor: magnetic flux density map and field lines at rated operating condition. 70

Figure 4.16 –Thermal endurance curve and percentiles for design temperature. 71

Figure 4.17 –Weibull CDF (i.e. unreliability) of the case-study PMSM insulation. ... 71

Figure 5.1 – Generic temperature profile. 78

Figure 5.2 – Loss of life fraction computation. 79

Figure 5.3 – A scheme of the proposed methodology for the thermal insulation lifetime estimation under dynamic temperatures. 81

Figure 5.4 – Coils hung to a PTFE rod inside the fume hood. 83

Figure 5.5 – Diagram of the experimental test setup. 83

Figure 5.6 – Experimental temperature profile TP#1. 84

Figure 5.7 – Experimental temperature profile TP#2. 85

Figure 5.8 – Flow diagram of the testing procedure. 85

Figure 5.9 – Weibull probability plot of cycles to failure for TP#1 (top sub-plot) and TP#2 (bottom sub-plot). 86

Figure 5.10 – Arrhenius-Miner model implemented in Simulink. 87

Figure 5.11 – Loss of life fraction for the temperature profile TP#1. 87

Figure 5.12 – Loss of life fraction for the temperature profile TP#2. 88

Figure 5.13 – Optical microscope enlargement for specimens aged with TP#1 at the end of their life..... 89

Figure 5.14 – Stress-strain curves of Torlon® polyamide-imide resin at various temperatures [130]. 90

Figure 5.15 – Diagram of the helicopter landing gear EMA. 91
Figure 5.16 – Landing gear EMA mission profile. 91
Figure 5.17 – Temperature profile TP#EMA. 92
Figure 5.18 – Loss of life relative to the 63.2% percentile of the Weibull distribution for TP#EMA. 92
Figure 5.19 – Weibull CDF of cycles to failure for TP#EMA. 93
Figure 5.20 – Extra-urban European driving cycle EUDC. 95
Figure 5.21 – Hot-spot temperature profile for the case-study traction PMSM operating with the EUDC driving cycle. 95
Figure 5.22 – Loss of life relative to the 63.2% percentile of the Weibull distribution for TP#AU-NC applied for 1 h. 97
Figure 5.23 – Loss of life relative to the 63.2% percentile of the Weibull distribution for TP#AU-C applied for 1 h. 97
Figure 5.24 – UAV mission profile and required power at the EM shaft – the speed is 10,000 rpm. 99
Figure 5.25 – Outer rotor BLDC motor. 101
Figure 5.26 – Peak and continuous torque for Prototype A at base speed. 102
Figure 5.27 – Peak and continuous torque for Prototype B at base speed. 103
Figure 5.28 – Magnetic flux density and field lines in overload condition (i.e. take-off). a) Prototype A, b) Prototype B. 103
Figure 5.29 – LPTN-estimated hot-spot temperature for Prototype B during a single mission profile. 104
Figure 5.30 – Weibull probability plot of the specimen's time to failure. 105
Figure 5.31 – Weibull survival probability plot of the tested specimens. 106
Figure 5.32 – 3D view of the designed prototypes (left-hand side Prototype B and right-hand side Prototype A). 107
Figure 5.33 – Proposed reliability-oriented design of electrical machines. 108
Figure 6.1 – (a) Simplified circuit representation of PEC, cable and EM implemented in LTspice® and (b) simulation outcome for t_r=50 ns and 5 m cable length. 112
Figure 6.2 – Overvoltage factor vs. cable length for different rise times (10, 20, 30 and 50 ns). 112
Figure 6.3 – Turn to turn voltage and propagation delay for short rise time PECs. 114
Figure 6.4 – Model employed for the turn to turn insulation analysis. 117
Figure 6.5 – Turn to turn electrostatic FE simulation at V_{peak}=740 V, using a magnet wire with 0.4 mm diameter and GR1 insulation. 118
Figure 6.6 – Turn to turn electric field distribution along the wire enamel surface for 1) V_{peak}=740 V and 2) V_{peak}=520 V. 118
Figure 6.7 – Model employed for the phase to phase insulation analysis. 119
Figure 6.8 – Model employed for the phase to ground insulation analysis. 120

Figure 6.9. Non-ideal insulating material model. a) Circuit schematic, b) Vector diagram. 122
Figure 6.10. Test voltage influence on the tanδ measurement..... 123
Figure 6.11. Direct PDIV detection on an industrial induction motor..... 124
Figure 6.12. Direct vs. indirect PDIV measurement on phase to ground insulation. 125
Figure 6.13. Direct vs. indirect PDIV measurement on phase to phase insulation.... 125
Figure 6.14. Direct vs. indirect PDIV measurement on turn to turn insulation. 126
Figure 6.15 – Test setup for the direct measurement of turn to turn PDIV in twisted pairs. 127
Figure 6.16 – Schematisation of magnet wire coated with a silver layer for capacitance measurement. 128
Figure 6.17 – Magnet wire coated with a silver layer for capacitance measurement. 129
Figure 6.18 – Test setup for the measurement of RPDIV. 130
Figure 6.19 – Specimen adopted for the phase to phase PDIV measurement. 132
Figure 6.20 – Measured phase to phase dielectric dissipation factor vs. applied voltage. 132
Figure 6.21 – Predicted phase to phase PDIV: electric field distribution vs. Paschen's curve. 133
Figure 6.22 – Experimental setup for the indirect measurement of phase to ground PDIV. 134
Figure 6.23 – Measured phase to ground dielectric dissipation factor vs. applied voltage. 134
Figure 6.24 – Cross-sectional view of the case-study rail traction PMSM. 135
Figure 6.25 – Rail traction PMSM slot layout for the two analysed insulation configurations. 137
Figure 6.26 – Instantaneous torque plot for the two analysed configurations, obtained through FE. 138

List of Tables

Table 1.1 – Electrical machines power density specifications for future aircraft.....3
Table 3.1 – Thermal and electrical counterparts.....26
Table 3.2 – Main geometrical dimensions of the EMA PMSM. 29
Table 3.3 – Critical thermal parameters for the analysed PMSM.....36
Table 3.4 – Main geometrical dimensions of the traction PMSM. 41
Table 3.5 – Thermal resistances (R) and capacitances (C) used in the 7-nodes LPTN 44
Table 4.1 – Properties of the adopted magnet wire. 52
Table 4.2 – Duration of the thermal exposure cycles. 54
Table 4.3 – Results summary of the accelerated thermal aging tests. 57
Table 4.4 – Weibull percentiles of failure time for a fixed shape factor β (coils specimens).....66
Table 4.5 – Main design parameters of the case-study, aerospace PMSM.....69
Table 5.1 – Comparison between experimental and estimated failure times (cycles). 88
Table 5.2 – Predicted number of cycles to failure using the Arrhenius-Miner model. 93
Table 5.3 – Main design parameters of the case-study traction PMSM. 94
Table 5.4 – Predicted time to failure for various percentiles of the Weibull distribution using the Arrhenius-Miner model. 98
Table 5.5 – Prototype A – design parameters. 100
Table 6.1 – Analysed magnet wire configurations and measured diameter/permittivity. 128
Table 6.2 – Predicted vs measured turn to turn PDIV. 129
Table 6.3 – Characteristics of the PWM pulses used for RPDIV assessment. 131
Table 6.4 – Measured (R)PDIV over a population of 5 specimens each (mean of the Weibull distribution). 131
Table 6.5 – Parameters of the rail traction drive. 136
Table 6.6 – Performances of the case-study traction PMSM according to the chosen insulation configuration. 139
Table A.1 – Convection heat transfer coefficients from CFD. A-5

Nomenclature

Abbreviations

AEA	All Electric Aircraft
BLDC	Brushless DC
CDF	Cumulative Density Function
CFD	Computational Fluid Dynamics
DSP	Digital Signal Processor
EASA	European Union Aviation Safety Agency
ECS	Environmental Control System
EM	Electrical Machine
EMA	Electromechanical Actuator
EMF	Electromotive Force
EUDC	European Driving Cycle
FE	Finite Element
GR	Grade
LPTN	Lumped Parameter Thermal Network
MEA	More Electric Aircraft
PD	Partial Discharges
PDIV	Partial Discharge Inception Voltage
PEC	Power Electronics Converter
PID	Proportional Integral Derivative
PM	Permanent Magnet
PMSM	Permanent Magnet Synchronous Machine
PTFE	Polytetrafluoroethylene
RPDIV	Repetitive Partial Discharge Inception Voltage
SP	Specimen

SQP	Sequential Quadratic Programming
TP	Temperature Profile
TS	Technical Standard
UAV	Unmanned Aerial Vehicle
VPI	Vacuum Pressure Impregnation
VSD	Variable Speed Drive

Symbols

$A\ [h]$	Pre-exponential factor of the Arrhenius Equation
$B\ [K]$	Parameter of the Arrhenius Equation
bip	Bipolar
C_d	Damage fraction
$c\ [m/s]$	Speed of light in vacuum
$c_{cu}\ [J/K/kg]$	Copper specific heat capacity
$C_{cyl}\ [F]$	Capacitance of cylindrical capacitor
class [°C]	Thermal class
$c_p\ [J/K/kg]$	Specific heat capacity
$c_{res}\ [J/K/kg]$	Resin specific heat capacity
$d_{cu}\ [kg/m^3]$	Copper mass density
$D_{in}\ [m]$	Inner diameter
dLF [h]	Loss of life fraction
$D_{out}\ [m]$	Outer diameter
$d_{res}\ [kg/m^3]$	Resin mass density
Dt [s]	Infinitesimal time interval
EF	Enhancement factor
$e_i\ [V]$	Incident wave
$e_m\ [V]$	Wave at the machine end
f [Hz]	Frequency
$F(t_i)$	Weibull CDF at time t_i
ff	Slot (copper) fill factor
ffw	Slot (wire) fill factor
$h\ [W/m^2/K]$	Convection heat transfer coefficient

HIC [°C]	Halving interval
j	Number of diagnostic sessions
J_{max} *[A/mm²]*	Maximum current density
k [W/m/K]	Thermal conductivity
$K(t_r)$	Rise time correction factor
kcu [W/m/K]	Copper thermal conductivity
kres [W/m/K]	Resin thermal conductivity
K_ψ	Measured number of cycles to failure at ψ^{th} percentile
K_ψ'	Theoretical number of cycles to failure at ψ^{th} percentile
L_{ins} *[h]*	Insulation lifetime
$L[\theta_i(t)]$ *[h]*	Insulation life at constant temperature $\theta_i(t)$
L_0 *[h]*	Reference lifetime
LF_{cycle}	Loss of life fraction at each cycle
m_b *[kg]*	Body mass
meas	Measured
N	Average number of cycles to failure
n_i	Number of cycles accumulated at stress level S_i
N_{SP}	Number of tested specimens
n_t	Number of turns
OF	Overvoltage factor
p	Pole pairs
ph-g	Phase to ground
p-p	Phase to phase
pred	Predicted
P_w *[s]*	Pulse width
Q	Slot number
R(t)	Reliability at time-instant t
R_{cond} *[K/W]*	Conduction thermal resistance
R_{conv} *[K/W]*	Convection thermal resistance
ri [m]	Inner radius of the heat path
ro[m]	Outer radius of the heat path
$R_{slotRad}$ *[K/W]*	Slot thermal resistance in the radial direction
S_i	i-th stress level

t_f *[h]*	Time to failure
tanδ	Dissipation factor
t_{liner} *[m]*	Liner thickness
t_r *[s]*	Rise time
t-t	Turn to turn
ttf [h]	Median of failure time
unip	Unipolar
unip+	Unipolar positive
V_{DC} *[V]*	DC link voltage
VF	Velocity factor
V_{peak} *[V]*	Peak voltage
$V_{ph\text{-}g}$ *[V]*	Phase to ground voltage
$V_{p\text{-}p}$ *[V]*	Phase to phase voltage
y [s]	Exposure cycle duration
Z_C *[Ω]*	Cable surge impedance
Z_M *[Ω]*	Machine surge impedance
α [h]	Scale parameter
B	Shape parameter
Δt_i *[s]*	i-th time interval
ε_e	Enamel relative permittivity
ε_e *[F/m]*	Vacuum permittivity
ε_r	Relative dielectric constant
θ [°C]	Temperature
θ_0 *[°C]*	Reference temperature
θ_i *[°C]*	Temperature during the i-th accelerated aging test
μ_r	Relative permeability
ρ_{SP}	Specimen dimension

List of Publications

Journals

1. **V. Madonna**, P. Giangrande, G. Migliazza, G. Buticchi, and M. Galea, "A Time-Saving Approach for the Thermal Lifetime Evaluation of Low Voltage Electrical Machines," *IEEE Transactions on Industrial Electronics*, 2020.
2. M. Galea, P. Giangrande, **V. Madonna**, and G. Buticchi, "Insulation systems for electrical machines: Reliability MUST become a main design objective," *IEEE Industrial Electronics Magazine,* vol. 14, no. 1, 2020.
3. **V. Madonna**, P. Giangrande, L. Lusuardi, A. Cavallini, C. Gerada, and M. Galea, "Thermal Overload and Insulation Aging of Short Duty Cycle, Aerospace Motors," *IEEE Transactions on Industrial Electronics,* vol. 67, no. 4, pp. 2618-2629, 2020.
4. **V. Madonna**, G. Migliazza, P. Giangrande, E. Lorenzani, G. Buticchi, and M. Galea, "The Rebirth of the Current Source Inverter: Advantages for Aerospace Motor Design," *IEEE Industrial Electronics Magazine,* vol. 13, no. 4, pp. 65-76, 2019
5. **V. Madonna**, P. Giangrande, and M. Galea, "Evaluation of Strand-to-Strand Capacitance and Dissipation Factor in Thermally Aged Enameled Coils for Low voltage Electrical Machines," *IET Science, Measurement & Technology,* vol. 13, no. 8, pp. 1170-1777, 2019.
6. **V. Madonna**, P. Giangrande, C. Gerada, and M. Galea, "Thermal analysis of fault-tolerant electrical machines for aerospace actuators," *IET Electric Power Applications,* vol. 13, no. 7, pp. 843-852, 2019.
7. **V. Madonna**, A. Walker, P. Giangrande, G. Serra, C. Gerada, and M. Galea, "Improved Thermal Management and Analysis for Stator End-Windings of Electrical Machines," *IEEE Transactions on Industrial Electronics,* vol. 66, pp. 5057-5069, 2019.

8. **V. Madonna**, P. Giangrande, and M. Galea, "Electrical Power Generation in Aircraft: Review, Challenges, and Opportunities," *IEEE Transactions on Transportation Electrification,* vol. 4, pp. 646-659, 2018.
9. **V. Madonna**, P. Giangrande, C. Gerada, and M. Galea, "Thermal analysis of fault-tolerant electrical machines for more electric aircraft applications," *The Journal of Engineering,* vol. 2018, pp. 461-467, 2018.

Conference Proceedings

10. **V. Madonna**, P. Giangrande, G. Migliazza, G. Buticchi, and M. Galea, "On the Thermal Insulation Qualification of Low Voltage Electrical Machines," in *IECON 2019 - 45th Annual Conference of the IEEE Industrial Electronics Society*, 2019, vol. 1, pp. 7115-7120.
11. **V. Madonna**, P. Giangrande, W. Zhao, Y. Wang, H. Zhang, and M. Galea, "Insulation Capacitance as Diagnostic Marker for Thermally Aged, Low Voltage Electrical Machines," in *2019 22nd International Conference on Electrical Machines and Systems (ICEMS)*, 2019, pp. 1-5.
12. P. Giangrande, **V. Madonna**, W. Zhao, Y. Wang, C. Gerada, and M. Galea, "Simplified Lumped Parameter Thermal Network for Short-Duty Dual Three-Phase Permanent Magnet Machines," in *2019 22nd International Conference on Electrical Machines and Systems (ICEMS)*, 2019, pp. 1-6.
13. C. Spagnolo, **V. Madonna**, S. Sumsurooah, C. I. Hill, and S. Bozhko, "Optimised low voltage loads allocation for MEA electrical power systems," in *2019 AIAA/IEEE Electric Aircraft Technologies Symposium (EATS)*, 2019, pp. 1-8.
14. **V. Madonna**, P. Giangrande, and M. Galea, "Introducing Physics of Failure Considerations in the Electrical Machines Design," presented at the *IEMDC 2019 - International Electric Machines & Drives Conference, 2019.*
15. P. Giangrande, **V. Madonna**, S. Nuzzo, C. Gerada, and M. Galea, "Braking Torque Compensation Strategy and Thermal Behavior of a Dual Three-Phase Winding PMSM During Short-Circuit Fault," presented at the *IEMDC 2019 - International Electric Machines and Drives Conference, 2019.*
16. **V. Madonna**, P. Giangrande, W. Zhao, H. Zhang, C. Gerada, and M. Galea, "On the Design of Partial Discharge-Free Low Voltage Electrical Machines," presented at the *IEMDC 2019 - International Electric Machines & Drives Conference, 2019.*

17. P. Giangrande, **V. Madonna**, S. Nuzzo, C. Spagnolo, C. Gerada, and M. Galea, "Reduced Order Lumped Parameter Thermal Network for Dual Three-Phase Permanent Magnet Machines," presented at the *IEEE WEMDCD'19 - Workshop on Electrical Machines Design, Control and Diagnostics, 2019.*
18. **V. Madonna**, P. Giangrande, W. Zhao, G. Buticchi, H. Zhang, C. Gerada*, et al.*, "Reliability vs. Performances of Electrical Machines: Partial Discharges Issue," presented at the *IEEE WEMDCD'19 - Workshop on Electrical Machines Design, Control and Diagnosis, Athens, Greece, 2019.*
19. **V. Madonna**, P. Giangrande, L. Lusuardi, A. Cavallini, and M. Galea, "Impact of thermal overload on the insulation aging in short duty cycle motors for aerospace," presented at the *2018 IEEE ESARS-ITEC*, 2018.
20. P. Giangrande, **V. Madonna**, S. Nuzzo, and M. Galea, "Design of Fault-Tolerant Dual Three-Phase Winding PMSM for Helicopter Landing Gear EMA," presented at the *2018 IEEE ESARS-ITEC*, 2018.
21. P. Giangrande, **V. Madonna**, G. Sala, A. Kladas, C. Gerada, and M. Galea, "Design and Testing of PMSM for Aerospace EMA Applications," in *IECON 2018 - 44th Annual Conference of the IEEE Industrial Electronics Society*, 2018, pp. 2038-2043.
22. **V. Madonna**, P. Giangrande, A. Walker, and M. Galea, "On the Effects of Advanced End-Winding Cooling on the Design and Performance of Electrical Machines," in *2018 XIII International Conference on Electrical Machines (ICEM)*, 2018, pp. 311-317.

Chapter 1 Introduction

This Chapter deals with the introduction of the Thesis. The main requirements for electrical machines employed in safety critical applications are outlined. The concepts of reliable and fault-tolerant electrical machines are introduced.

1.1 Transportation Electrification

In recent years, transportation electrification represents the way forward for reducing CO_2 emissions and cutting down toxic particles. At the very centre of this effort is one of the most important systems, namely the electric drive, which is typically composed of an electrical machine (EM), driven by a power electronics (PE) converter supervised by advanced control algorithms. The EM is generally a main contributor of weight and losses. Therefore, in the push towards highly electrified systems, more compact and lightweight EMs are required, particularly in aerospace and automotive applications [1, 2].

In the automotive sector, the technology readiness level is such that the internal combustion engine is already being successfully replaced by high performance EMs [3]. The first mass-produced hybrid electric car was introduced on the market by Toyota in the late ‘90s, whilst several full electric cars are nowadays commercially available from different manufacturers. Thus, the automotive sector can be considered as the precursor of modern electrification programmes. This is also partly due to all the advancements in EMs design.

At the same time, in the aerospace sector, the demand for performance optimization and the need for decreasing both operating and maintenance costs have encouraged the aircraft industry to move towards more electric solutions. With the

advent of the more electric aircraft (MEA) initiative, electric power systems are progressively taking the place of pneumatic, hydraulic and mechanical power systems [4]. Over time, this trend has led to a considerable increase of required on-board electric power, particularly for larger aircraft. This evolution is clearly shown in Figure 1.1. However, it is also true that almost three decades of work and effort on the MEA, have not yet given a definite answer to whether this initiative represents really a better solution or not at system level. So, while the aerospace community is still debating the feasibility and implementation of the MEA, a new movement, that has taken hold over the last couple of years and is creating a lot of excitement, is represented by both the hybrid gas/electric propulsion and the all-electric aircraft (AEA) [5-7]. The latter aims at completely removing the traditional air-breathing engines, which depend on the Jet-A fuel as main energy source.

Both MEA and AEA concepts rely intensively on electromechanical energy conversion through the use of EMs [8]. Whether EMs are being used for driving secondary systems such as electromechanical actuators, fuel pumps, environmental control units, auxiliaries etc., or whether being used as a primary means for propulsion, the EM role in future aircraft remains undisputed.

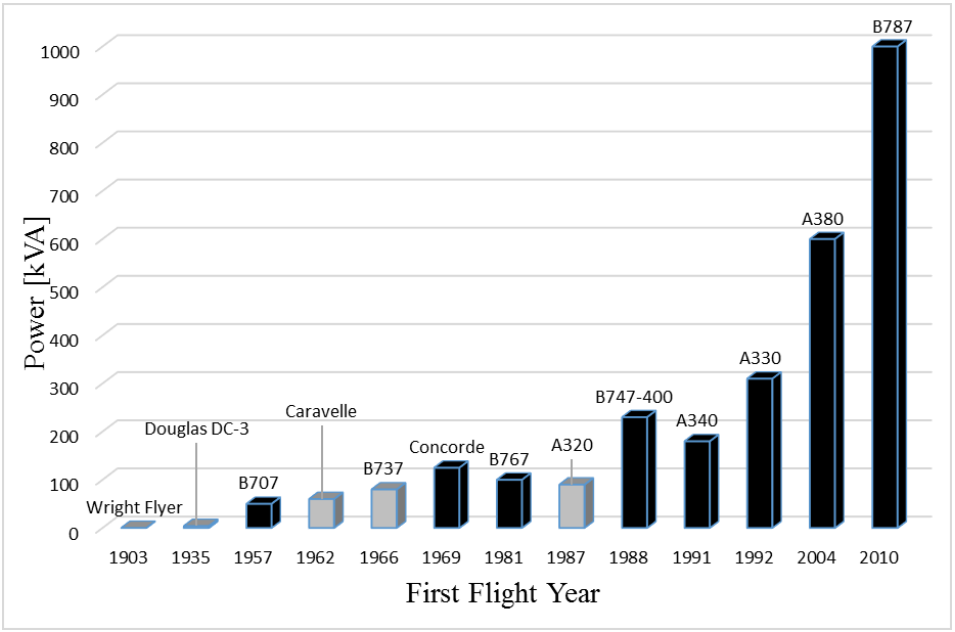

Figure 1.1 – Evolution of electrical power need (grey: short- to medium-range aircraft and black: medium- to long-range aircraft).

It is therefore clear that EMs have a central importance in transportation electrification. A primary requirement for these EMs is represented by a high level of power (and torque) per net weight and/or volume. This requirement will be even more stringent in the near future [8]. A prediction of EM power density requirements for the short-, mid- and long-term future is tabulated in Table 1.1 [9], which conforms with data and roadmaps from national [8] and international [10, 11] aerospace agencies and bodies. In line with these considerations, an in-depth historical literature review on the topic of aircraft electrification has been carried out and it is published in [9].

Table 1.1 – Electrical machines power density specifications for future aircraft

Time-lines	Predicted Power Density	Enabling Technology
By 2025	10*kVA/kg*	Liquid cooling, Low Loss Steel, High Breakdown-Strength Insulating Materials, Additive Manufacturing, Nanocomposite-Based Magnetic Materials
By 2035	20*kVA/kg*	
By 2050	40*kVA/kg*	All the above + Superconducting materials

1.2 Towards Reliability-Oriented Design of Electrical Machines

In a safety-critical system any failures might endanger human life, lead to substantial economic loss, or cause extensive environmental damage. Within the MEA framework, a number of devices/systems, powered by EMs, can be considered as safety critical (e.g. electromechanical actuators for primary and secondary flight control surfaces, landing gear extension/retraction mechanisms, fuel pumps etc.). Thus, while it is true that the industry needs to always improve and achieve even better power densities, however, this cannot compromise the reliability and lifetime of the EM. It is imperative, and also the Author's opinion, that for the aerospace industry a main goodness factor of any EM should be that characterised by its reliability figures and/or fault-tolerance capabilities.

Unfortunately, a call for reduced failure probability (often) collides with the requirement for higher power dense EMs. The most common way for improving the power to weight ratio is by either increasing the current density, and/or working at higher switching frequencies, enabling high speed operations. Both strategies directly translate in larger thermal loadings, namely power losses per unit volume, and thus enhanced stress levels. If materials and design strategies are not adapted for coping with such operating conditions, the probability of electrical failures can dramatically rise. In short, for a given machine, the price one must pay for an improved power density is accepting a higher risk of failure, or, in other words, a shorter lifetime.

In the past 20-30 years, a wide number of studies regarding EMs failure have been published [12-17]. These mainly refer to high power EMs for power plants and induction motors for industrial applications. The outcomes of these surveys are always very similar. The top two components to fail in EMs are in general the bearings and/or the stator (armature) insulation. Also, it is usually reported that electrical failures are mostly due to turn to turn insulation breakdowns [17-21]. This insulation sub-system is the one providing galvanic separation among turns belonging to the same phase.

A very important aspect of modern EMs control is however the advent of the variable speed drive (VSD), employing pulse width modulation (PWM) techniques. This type of technology, which actually completely changed the game in terms of EM controllability, has also had its major side effect, namely the added stresses and consequent failures on EM windings. A large number of premature insulation failures have been reported [19, 22-24], mostly caused by the enhanced stress that PWM waveforms cause on the insulation. This, in conjunction with the huge advancements in bearing technology, aided by their regular maintenance and overhaul scheduling, is resulting in electrical failures to become ever-more dominant. It is today perceived that in transport applications, which almost employ only PWM-driven VSDs, insulation breakdown is more common than mechanical failures such as those of the bearings.

All this clearly indicates that new design methodologies for EMs are required that do not only aim to achieve higher performance, but do so while actually improving, or at least safe-guarding, reliability and lifetime expectancies.

On these premises, it is necessary to specify that this work will analyse only failures of electrical nature that concern insulation for EMs. In particular, the focus will be on machines with rated voltage <1000 V, as they represent the primary choice for transportation application [25-31]. For the sake of clarity, a typical winding layout for such low voltage EMs is shown in Figure 1.2, where the three insulation sub-systems are depicted [32].

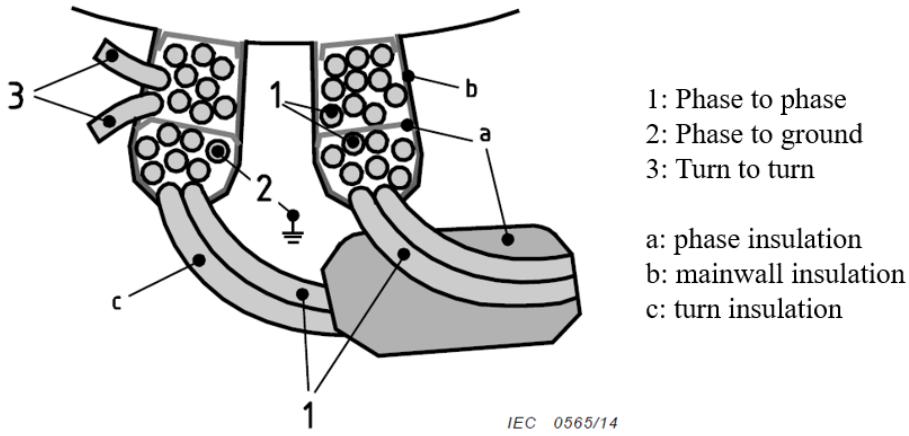

Figure 1.2 – Insulation sub-systems in a typical low voltage EM [32].

1.3 Fault-Tolerant Electrical Machines

The first strategy for guaranteeing safe operations of critical systems is represented by fault-tolerant EMs (drives) topologies [25, 31]. If specific design choices and appropriate control strategies are embraced, fault-tolerant machines can operate safely even during/after severe faults [33-36].

A machine topology widely adopted in high performance applications, due to its excellent power density capability, is the permanent magnet synchronous machine (PMSM). However, the presence of permanent magnets (PMs) is a source of concern, since the excitation field is constantly present, and then the machine is always “on”. In PMSMs, a suitable fault-tolerance level is achieved when the following constraints are met:

a. The physical separation between phases

b. Magnetic isolation between phases
c. The implicit limiting of fault currents
d. Effective thermal isolation between phases
e. Complete electrical isolation between phases

Conditions *a-d* can be simultaneously satisfied at machine level (i.e. acting on the EM design) by e.g. adopting a single layer, concentrated winding within a multi-sector magnetic structure. However, condition *e* is usually very difficult to reach, mainly because of it being inherently a system-level issue. That is, the complete drive topology (i.e. EM, power electronics and control strategy) must be carefully chosen for meeting this requirement. A drive topology which satisfies condition *e,* consists in adopting independent power supplies either for each EM phase or for each winding set, such as in double three-phase machines. This approach, known as power segmentation, allows for a true electrical isolation between phases; thus, the machine is able to operate also under extreme fault conditions such as open and short circuits. In such cases, PMSMs can still deliver the required torque by applying appropriate control strategies. A system-level scheme of a double three-phase drive, controlled through the power segmentation approach, is shown in Figure 1.3.

It is clear that the adoption of measures for fault-tolerance fulfils the requirements of safety-critical systems. Nonetheless, fault-tolerance features also bring an increment in cost, weight and system complexity, things that do not completely go hand-in-hand with the concepts of transportation electrification. Here is where the need for reliability considerations comes into play, if both (system-level) power density and lifetime requirements need to be satisfied.

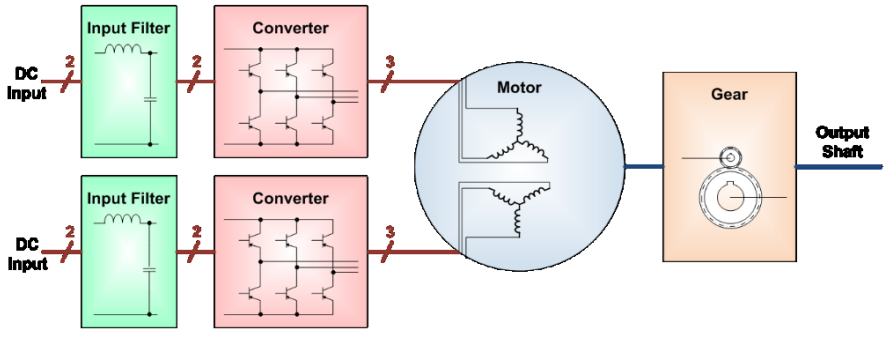

Figure 1.3 – Double three-phase drive architecture and power segmentation approach.

1.4 Reliability of Electrical Machines

Despite fault-tolerance and reliability being "sides of the same coin", they have a completely different meaning. Indeed, a system is considered reliable if it can perform its duty without failures for a specified period of time and given a set of boundary conditions (e.g. ambient temperature, humidity, pressure, vibration level etc…). Thus, it can be stated that fault-tolerance and reliability complement each other. In other words, if an EM is 100% reliable (for a given number of operating cycles/hours), it means that a 0% fault-tolerance level is required. In fact, this machine will never be subject to failures throughout its useful lifetime. This, of course, is impossible to achieve since real systems cannot have 100% reliability. Nonetheless, this theoretical explanation is useful for defining an important concept. If an EM is designed in such a way that its probability of failure, at a given time instant, is below a pre-defined threshold level (given by the specific application), then, it would be possible to reduce (if not eliminate) fault-tolerance measures. Indeed, the latter (i.e. fault-tolerance) can be seen as a methodology to compensate for a non-satisfactory reliability level. A main objective of this Thesis will be actually quantifying the probability of failure for a given insulation system operating under stated conditions.

Reliability of electrical machines ranges over a wide spectrum of disciplines. With reference to the insulation system, an EM can fail (or be subject to abnormal aging) because of thermal, electrical, ambient, and mechanical stresses. In many cases these stressing factors act simultaneously, giving rise to even higher stress levels. In order to implement a "design for reliability", it is thus necessary to have a precise knowledge (at the design stage) of the EM operating environment, mission profile, drive configuration and any additional source of stress. These can be combined in physics of failure (PoF) -based lifetime prediction models. As outcome, one can eventually predict the probability of failure after any number of operating cycles. Therefore, this design methodology allows to tune the EM design parameters in order to precisely meet reliability constraints and avoid the so-called "over-engineering". On the other hand, if the final design is already given (i.e. geometry and materials are

already chosen), then, the same models can be used for predicting the time to failure of that particular machine for a given mission profile and boundary conditions (i.e. operating environment).

It is obvious that if one can predict the number of cycles before failure, for a given EM, the design measures for fault-tolerance can be somehow "relaxed". That is, in many cases, having a lighter, cheaper and easier to control machine (drive). Therefore, paradoxically, including reliability considerations at the design stage can satisfy the other main requirements for EMs in mobile applications, i.e. high power density. The cost does not generally represent an issue in the aerospace industry, but it is a major requirement in automotive (especially for mass-produced vehicles), owing to an additional motivation for taking on-board reliability considerations in EMs design.

1.5 Main Contributions of the Thesis

The work presented in this Thesis aims in proposing a "paradigm change" in the design of EMs for transportation applications. Reliability, which was traditionally taken as a "final product" for a given EM, can become an integral part of the design process, if the models/analyses presented in this work are implemented. These are carefully selected and combined with notions of PoF, statistics and probability analysis. A design of experiments activity is carried out for choosing the most suitable specimens and testing procedures necessary to validate the discussed models. All of this for guaranteeing an optimum between accuracy, time and cost. Several works have been presented throughout the last half century analysing the insulation as a "stand-alone" system. Nonetheless, only few of them have tried to integrate the notions of dielectrics aging phenomenology in the design process of EMs. For this purpose, several "real life" case-studies are examined and presented along the Thesis, with the objective of demonstrating how the proposed models can be integrated in the study and design of EMs.

Overall, the analyses presented throughout this work argue on a radical step-change in how EMs reliability is assessed. The use of advanced methodologies is proposed, that addresses the much-needed direction change and develops a coherent

argument as to why the proposed philosophy needs to become the norm across the whole field of EMs, in the near future.

1.6 Thesis Outline

Apart from Chapter 2 (i.e. literature review) and Chapter 7 (i.e. conclusions), every other Chapter has a similar structure. It starts with the problem statement, where a brief overview on the specific "issue" to be addressed is provided. The Chapter's core is then presented, generally consisting in model(s) introduction / description. Follows the design of experiments and experimental validation / tuning. Throughout the various Chapters, several case-studies are introduced, for aiding the readers in implementing the proposed models / design procedures in real applications. The list provided below summarizes the content of each Chapter.

- Chapter 2 provides a wide literature review on insulation aging in low voltage EMs. Particular focus is given to the two main aging factors, namely, thermal and electrical.
- In Chapter 3, the thermal modelling of EMs is introduced. In fact, since part of the Thesis is focused on aging deriving from thermal effects (i.e. high temperature), this Chapter is a pre-requisite for the analysis that follows.
- Chapter 4 deals with the insulation thermal aging in continuous duty EMs (i.e. constant temperature). The Arrhenius model for thermally accelerated chemical reactions is described, validated and applied for the insulation lifetime assessment.
- In Chapter 5, the same model presented in Chapter 4 (i.e. Arrhenius) is combined to the cumulative damage law, for analysing the insulation aging in EMs operating under non-constant temperature.
- Chapter 6 focuses on insulation extrinsic electric stress. The PD phenomenology is introduced and three simplified electrostatic models

are combined to the Paschen's law for assessing whether or not an insulation is subject to PDs.

- Chapter 7 concludes the Thesis and summarizes the obtained results, providing "food for thought" for future research in the field of EMs reliability and PoF analysis.

Figure 1.4 is introduced for providing a logical link among the various Chapters, and for facilitating the reading.

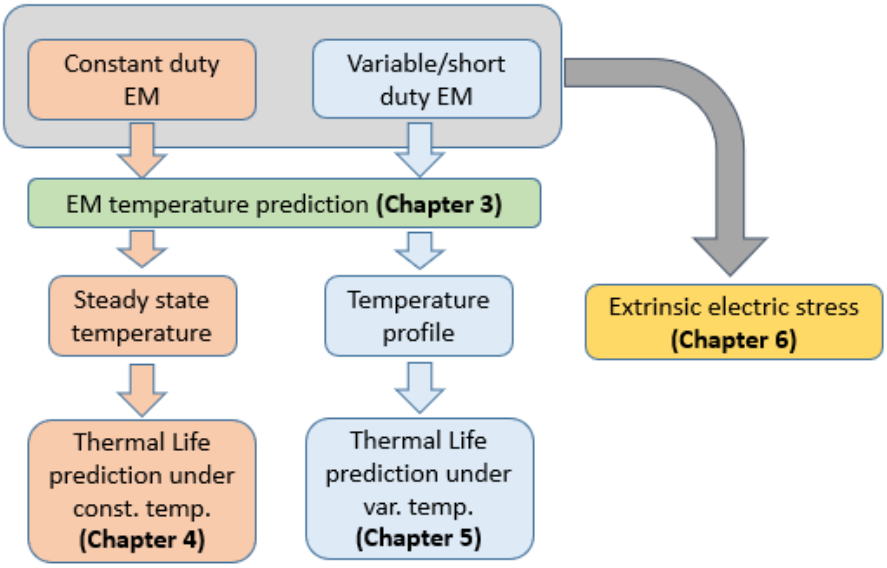

Figure 1.4 – Thesis structure and link among Chapters.

1.7 Concluding Remarks

This Chapter aimed at giving a "flavour" about the contents of this Thesis. The main concepts are briefly outlined, without going deep into details. General considerations regarding global warming, carbon emission goals, and advantages of more electrified solutions are purposely omitted. These information are easily accessible on the web to any interested readers. As already mentioned, for this purpose, a wide literature review on the topic is provided in [9].

Chapter 2 Thermal and Electrical Aging in Low Voltage EMs Insulation

This chapter presents a literature review regarding EMs insulation aging factors. A general overview about the various stresses is provided. Since this Thesis will mainly focus on thermal and extrinsic electric stresses (i.e. partial discharges), in this review, a particular emphasis will be given to these two factors.

2.1 Overview of Insulation Stress Factors

The factors that stress an EM's insulation system are generally grouped under the acronym "TEAM", namely Thermal, Electrical, Ambient and Mechanical. For some particular applications, the stress source can be also the combination between two or more of the listed factors. As stated in [37] the aging level resulting from these combinations does not follow the principle of superposition of effects. Nonetheless, if one of the aging factors is predominant above the others, it is then reasonable to employ a single-stress lifetime prediction model. This Section serves as a high-level introduction of these stresses.

Thermal stress is an insulation aging factor for both low and high voltage (i.e. >1000 V) EMs, where the composition of the materials used for their insulation systems can be either organic or inorganic. One of the first rules an EM designer learns is that "every time the insulation temperature increases by 10 °C, its lifetime is halved". As will be shown in the following, this is not "just a rule of thumb", but it is actually based on an important chemical law.

Any discussion about electrical stress, first necessitates an introduction to and definition of partial discharge (PD). PDs are electrical discharges that only partially bridge the insulation between two electrical conductors [38]. For insulation systems with organic chemical composition, the inception of PDs might lead to their rapid deterioration with consequent breakdown. The latter (i.e. organic insulation) is defined by the IEC technical standard (TS) 60034-18-41 [32] as Type I insulation. Common examples of EMs insulating materials which can be classified as "Type I" are polyamides, polyimides, polyesters and epoxies. These are often recognised by their trade names e.g. Kapton®, Nomex®, Epoxylite® etc. On the other hand, Type II insulations [39] have inorganic or mixed organic/inorganic chemical compositions, e.g. mica and fiberglass etc. Because of this feature, contrarily to Type I materials, they can, to a certain extent, withstand the PD inception. Thus, EMs equipped with Type II insulation can be said to typically withstand and survive PDs throughout their lifetime, although this will cause progressive insulation deterioration. Hoverer, the vast majority of low voltage EMs, and in particular those employed in transportation applications, adopt Type I insulation. They are thus required to not experience any PD activity throughout their whole lifetime. It is a task of the drive integrator to guarantee and verify the fulfilment of such crucial condition. This because the possibility of PD inception is not only related to the EM insulation itself, but it is also strongly influenced by the PEC characteristics, as will be clearly demonstrated in Chapter 7. Thus, in a PD-free EM it is reasonable to assume temperature as the main aging factor (eventually amplified by harsh environmental and operating conditions).

Ambient stress refers to all those factors which derive from the environment in which the EM operates. Paraphrasing [40], ambient factors in themselves do not cause aging, but when combined with other sources of stress (e.g. thermal and electrical), then they might start compromising and degrading the insulation system and its functions. In this work, they are regarded as a factor of influence rather than an aging factor. This is extremely important in aerospace, where the high altitude, and therefore the lower pressure, results in much higher probability of PD activity than when at ground level.

In transportation applications there are two main sources of mechanical stress. Mechanical vibrations and mismatches in thermal expansion coefficients among materials. Vibrations can be caused either by the machine itself, e.g. a not properly designed or aligned EM, or by external factors. The former - which include e.g. rotor unbalance, electromagnetic forces, torque ripple - can be avoided (or at least minimised) by careful design and development of quality control processes. In transportation applications, vibrations can also be a system-level factor (e.g. an EM installed on an electric or hybrid car). The reality, however, is that the effects of these vibrations on the insulation system cannot be considered as a "stand-alone" stress. Similar to "ambient" stresses, these are usually considered when combined to another aging factor. Essentially, if the insulation is already deteriorated because of thermal and/or electrical aging, then, mechanical shocks and/or vibrations can accelerate the degradation process. Another mechanical stress effect is that caused by mismatches in thermal expansion coefficients among materials. This is extremely important for high voltage EMs, where these mismatches can cause severe failures such as ground-wall delamination. This aspect is deeply investigated for low voltage EMs in [41], where it is clearly shown that for epoxy-impregnated EMs, thermal expansion mismatches can induce severe mechanical fatigue in the insulation.

Electrical stress gives a negligible contribution to the aging in low voltage, mains-fed EMs (i.e. EMs fed by 50 Hz grid, without a PEC). This is the reason why the insulation for such machines is mainly determined by mechanical considerations rather than electrical [40].

Considering all the above, then it can be concluded that for most low voltage EMs, operating in a PD-free regime, the most important insulation aging factor to consider is the thermal stress. This hypothesis is actually extremely important for this Thesis, as it defines a major aspect of the reasoning behind the development of the presented work. It is for this reason that the rest of the work will have a particular focus on thermal aspects.

On the other hand, it is also important to note that a machine/drive originally designed to be free from extrinsic electric stress, might, at some point in time, fall in a

situation where PD could be incepted because of manufacturing flaws and/or extreme operating condition (e.g. high temperature, humidity, etc…). A particular example is the presence of air cavities within the secondary insulation system (i.e. winding impregnation). Such "disturbances" need to be considered at an early stage during the insulation system design, for avoiding unexpected failures once the EM is in operation. This justifies why most of the scientific papers analysing the PD phenomenology in low voltage EMs winding, present experiments carried out on non-impregnated twisted pairs specimens, that is, assuming the worst case scenario (i.e. enamelled wires surrounded by air). Nonetheless, it is the job of EM manufacturers to try and minimise these flaws, and therefore aim at fully repeatable manufacturing processes.

2.2 Thermal Aging

High temperature is widely recognised as one of the primary causes of insulation failures in electrical machines [12-15, 42]. Most of the insulation system failures are caused by the deterioration and breaking-down of the turn to turn insulation [18, 43]. As a matter of fact, an interturn short circuit does not cause the instantaneous EM outage. It is the increase in Joule loss in the faulty/shorted turns which causes a localised temperature hot-spot, eventually leading to a deleterious chain reaction (i.e. within a short time more and more turns will be affected by the fault). This is why the winding life in a low voltage EM is assumed to correspond to that of its interturn insulation sub-system.

The first pioneering work about the effect of temperature on insulation lifetime can be found in [44] and was published in 1930. It was in this paper, that the famous "10 Degrees Rule" also known as "Montsinger's Rule", was first introduced. While the outcomes of [44] were at first criticised due to them being based on empirical studies performed on power transformers, however, then they were partially confirmed in 1947, through the work presented in [45]. In this last work, for the first time, the deterioration of electrical insulation caused by temperature is treated through the Arrhenius law. In this work, the Author confirmed and improved the work of [44], and it is actually stated

in the paper's synopsis that "*the approximate 7 to 10 degrees rule for the temperature coefficient of deterioration rate is replaced by a more accurate theoretical expression*". From a practical perspective, the most important contribution of Dakin's model of [45] is that given by (2.1) below, which states that the lifetime L_{ins} of a solid insulating material operating at absolute (thermodynamic) temperature θ can be calculated by an exponential law, where A and B are parameters depending on the material properties.

$$L_{ins} = A \cdot \exp(B/\theta) \tag{2.1}$$

If the thermal class (or any other "reference temperature") of the insulation, θ_0, is known, then (2.1) can be rearranged as in (2.2) [37], where L_0 is the life at temperature θ_0, which is generally 20,000 h if θ_0 is the thermal class.

$$L_{ins} = L_0 \cdot \exp\left[-B\left(\frac{1}{\theta_0} - \frac{1}{\theta}\right)\right] \tag{2.2}$$

From (2.1) and (2.2), Montsinger's rule can then be derived as expressed by (2.3), where *HIC* is the halving interval, which identifies the temperature increase in Celsius degrees for a corresponding 50% lifetime reduction.

$$L_{ins} = L_0 \cdot 2^{\frac{\theta_0 - \theta}{HIC}} \tag{2.3}$$

These model are generally accurate for the lifetime prediction of machines operating at constant temperature [37, 46], where there is a dominant chemical reaction involved in the insulation thermal degradation [47]. Therefore, the parameter B in (2.1) and (2.2) is directly related to the activation energy of the (dominant) reaction involved in the thermal degradation process [48], being these models based on the Arrhenius law.

If an EM is subject to dynamic loading (i.e. variable duty cycle), its insulation temperature will follow a time-dependent temperature profile. This is usually the case with EMs employed in transportation applications (e.g. traction motors, electromechanical actuators etc…). In this case, these models then need to be properly modified in order to introduce the influence of variable temperature. A lifetime model accounting for the dynamic temperature is presented in [49], where the analysis is

carried out through simulations performed on an EM for a traction application. Similarly, the impact of repeated motor starts on the insulation lifetime is evaluated and quantified in [50], where the study is focused on mains-fed induction motors. In [51] a real time insulation lifetime monitoring method is proposed. This is based on the application of the Arrhenius model and it accounts for transient operations of low voltage, organic insulated motors. Similar models have also been proposed in [52] for the analysis of insulation degradation in high voltage AC cables.

All these works base the lifetime prediction on the Arrhenius model (i.e. (2.1)) combined with the cumulative damage law [53] (or Miner's rule). This can be expressed as in (2.4), where C_d is the damage fraction, n_i is the number of cycles accumulated at stress level S_i and N_i is the average number of cycles to failure.

$$C_d = \sum_{i=1}^{k} \frac{n_i}{N_i} \tag{2.4}$$

However, it is important to note that this approach neglects the potential detrimental effect caused by thermally-induced mechanical stresses in the insulating materials deriving by dynamic loading. Mismatches in materials thermal expansion coefficients, combined with dynamic temperatures are a primary cause of premature insulation failure in large generators [54-56]. Nonetheless, in relatively-recent works [41, 57-59], it was demonstrated that even low voltage EMs might suffer thermomechanical insulation degradation if subject to dynamic thermal loading. In [41] the insulation fatigue caused by thermomechanical stress is accurately evaluated through finite element (FE) simulations as well as accelerated lifetime tests. It is found that the thermomechanical fatigue is the dominating degradation mechanism for a study-case, epoxy-impregnated traction machine. Similar results, are found in [59], where the analysis is carried out on non-impregnated coils specimens for low voltage EMs.

Considering all this, then a main component of this Thesis is to investigate and analyse the effectiveness of the Arrhenius model combined to the cumulative damage law for accurately predicting the lifetime of thermally cycled EMs insulation. The term "accurately" here indicates the ability to predict the insulation' probability of failure

through a suitable statistical distribution. Appropriate testing conditions are used in order to investigate the effects of aging stresses on particular case examples. The main highlight of all this is that most of the work is done experimentally on representative samples, with the aim of providing results as realistic as possible.

2.3 Extrinsic Electric Stress

Extrinsic aging is defined by the TS IEC 60505 [38] as "*irreversible changes of properties of an electrical insulation system caused by action of aging factors on unintentionally introduced imperfections in the electrical insulation system*". Low voltage EMs are not expected to operate under PD regime [32]. Therefore, PDs can be considered as an extrinsic electric stress factor. The "*imperfection*" [38], in this case, is the presence of air cavities (i.e. voids or air gaps) within the electrical insulation system. Thus, a high quality impregnation can minimize the probability of PDs inception [60]. PDs are incepted in air cavities when a) a first electron is available [61, 62] and b) the electric field in the cavity is above the discharge inception voltage of air (i.e. $\approx 3\ kV/mm$ at sea level pressure) [63, 64]. The inception voltage is generally modelled through the Paschen's curve, first discovered in 1899, and then confirmed experimentally in 1977 [63], which is depicted in Figure 2.1. It shows the gas (air) breakdown voltage as a function of the product between the electrodes spacing (i.e. proportional to the gap dimension) and the atmospheric pressure. This empirical curve was obtained with two plane electrodes, in which one of the two is covered by an insulating coating. It is widely adopted for the computation of the PD inception voltage (PDIV) in low voltage EMs insulation [64-66] and aerospace electrical systems [67].

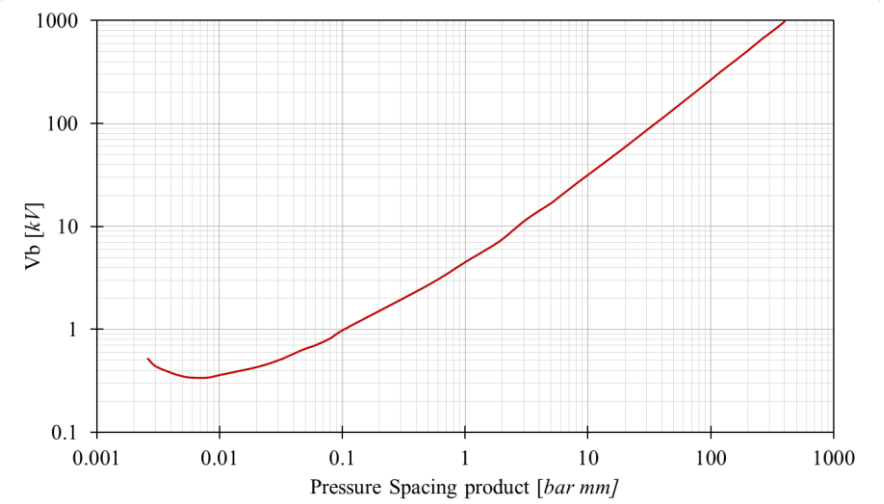

Figure 2.1 – Paschen's curve for air.

The problem of PDs in low voltage EMs, "took a turn for the worse" with the widespread of variable speed drives (VSDs) where the EM is supplied by a power electronics converter (PEC) [68-73]. VSDs are extremely effective for precisely controlling the torque and speed of EMs, through the application of PWM-modulated voltage [74-76]. Nowadays, any high performance EM operating at variable speed is fed by a PEC [34, 77-82].

The inception of PDs in a PWM-fed low voltage EM is essentially caused by the enhanced voltage level at the EM's terminals. This phenomenon arises by the multiple waveform reflection caused by impedance mismatches between the converter, feeder cable and machine. Pioneering scientific papers in this area have been published [19, 22, 24]. In these works, the problem of voltage amplification at the motor's terminals is addressed through the standard theory of transmission lines. This approach is extremely valid, so much that even technical standards for the qualification of PWM-fed motors (i.e. IEC 60034-18-41 and IEC 60034-18-42) are based on it [32, 39]. This will be the approach followed in Chapter 6 of this Thesis, which will investigate these phenomena.

Extensive research concerning the combination between PECs and PD inception in low voltage EMs has been carried out in a 3-parts work published in 2010 [71-73], and compiled together in [83]. In the first part [71], the phenomenology

associated with PECs is presented. The expected voltage waveforms at the terminals of PWM-fed motors are computed. It is stated that when the surge input impedance of the motor is considerably larger than the cable characteristic impedance, the amplitude of the voltage pulse may double. This phenomenon can be easily observed in Figure 2.2, where the qualitative phase to phase voltage waveform (single period) in a PWM-fed EM is shown. This is a critical point when considering low voltage EMs, as their surge impedance tends to be orders of magnitude larger than the connecting cable's one [84]. Chapter 6 will provide guidelines for identifying and quantifying the extent of these detrimental phenomena, according to the electric drive characteristics. In [72], the lifetime modelling of insulation systems is carried out. The negative effect of PD inception in organically-insulated enamelled wires is clearly demonstrated. The third part [73] mainly focuses on diagnostic properties and quality assessment of insulation systems to be used in PEC-fed EMs.

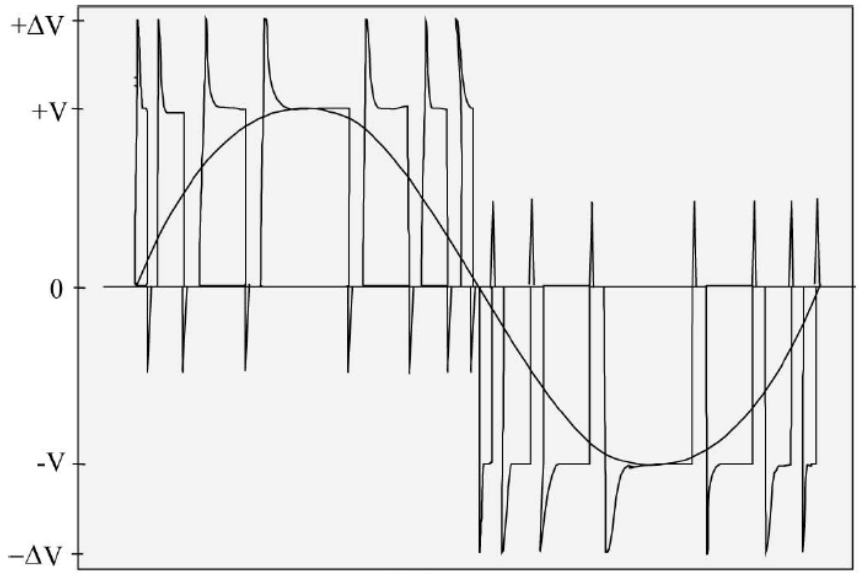

Figure 2.2 –Single period of the phase to phase voltage waveform in a PWM-fed EM (qualitative representation) [71].

A large number of recent publications deal with PD phenomenology and aging in EMs fed by modern PWM PECs [69, 85-90].

In [69], the influence of PWM waveform characteristics on the lifetime of polyamide-imide-insulated, crossed-pairs specimens is analysed. It is experimentally

demonstrated that the PD magnitude is influenced (i.e. decreases) with increasing waveform rise times. Furthermore, it is shown that a longer impulse duration causes a PD magnitude increment. Reference [85] demonstrates that the specimens' (i.e. polyamide-imide crossed pairs) lifetime, using repetitive square wave voltages decreases with increasing impulse voltage duration. These works provide extremely useful information by going in-depth into the PD phenomenology. They clarify how the characteristics of the applied waveform can strongly influence the specimen's lifetime. Nonetheless, despite the tests being performed on Type I winding samples, the Authors do not provide any information on how these data can fit into the design of insulation for an EM.

The influence of PWM/PEC parameters on the PDIV is also analysed in [86]. In this paper, it is shown that decreasing the waveform rise time, causes a reduction of the PDIV in twisted pairs specimens. The presented results are interesting from an electric drive designer perspective. Indeed, the recent trend in PECs is to move to ever-faster power modules, featuring extremely short rise PWM-modulated waveforms. This means that a short waveform rise front, produced by a fast switching converter, should, from a phenomenological point of view, have less probability in incepting an interturn PD. Nonetheless, it must be also pointed out that a shorter rise time has more probability of causing voltage overshooting and ringing, as already mentioned and will be demonstrated in Chapter 6. Thus, the aforementioned benefit in terms of PDIV increment is partially eclipsed. Additionally, in [86], the probe used for PD detection is a coaxial cable sensor coupled to a high pass filter and directly connected to an oscilloscope. A similar detection method is adopted in [91] where a Jack-SMA connector coupled to a coaxial cable is used as PD detection sensor. The same approach, based on PD detection through an antenna-like sensor, will be followed in this Thesis.

The influence of high dV/dt is analysed, among others, in [87]. In this work, it is surprisingly demonstrated that tooth-coil winding (i.e. concentrated winding) can be operated at high dV/dt and high switching frequency without having partial discharge problems. The authors claim that the reason for such behaviour is attributed to the high turn to turn capacitances of this winding topology. However, from the manuscript's

discussion it is not clear if the relative position among turns is known (i.e. form wound coil) or if the single coil is randomly wound. In addition, the tests are carried out on a single formette, thus, in case the winding is randomly wound, the repeatability of the presented results is questionable.

The effects of extra short rise times (down to 15 ns) on the PD phenomenology are also investigated in [88]. High voltage solid state switches, in push-pull configuration are used to generate variable frequency, short rise time waveforms. It is shown that the voltage level where PD occur influences the PD magnitude. In particular, the rise time reduction causes an increment in the PD magnitude. Furthermore, it is carried out an analysis on the partial discharge extinction voltage (PDEV), that is the applied voltage at which repetitive PDs cease to occur in the test object, when the voltage applied is gradually decreased from a higher value (at which PDs are observed) [92]. It is found that the PDEV decreases with decreasing rise times. Even in these examples, no details on how to feed these (important) information into the EM design and into the choice of insulation are provided.

More recently, a model for determining the PDIV of magnet wires has been published in [89]. Various insulation thicknesses (i.e. grades) and wire diameters are investigated. In this work, a different theory with respect to the Paschen model for PD inception is used and is based on the Schumann's streamer inception criterion. It is demonstrated that reducing the wire diameter, as well as the grade, causes a decrement in PDIV. However, how the winding choice can influence the torque-producing performance of an EM is not verified, neither by analytical/finite element analyses nor by experiments on real machines. A further PDIV reduction is identified when increasing the temperature, as already indicated in various other publications and technical standards [32].

Online and offline PD monitoring methods under impulsive voltage waveforms are presented in [93]. In this case, the tests are carried out on complete low voltage induction motors. The authors introduce a new testing procedure for such kind of specimen's arrangement. The latter allows to evaluate the repetitive PDIV in each

insulation sub-system (i.e. phase to phase, phase to ground and turn to turn), representing an extremely useful tool for EM designers and testing laboratories.

The influence of altitude (i.e. ambient pressure) on the PD inception in aerospace EMs is investigated in [94]. In this work the turn to turn PD inception behaviour is analysed by using twisted pairs specimens, whilst the phase to ground is assessed by a special arrangement in which, the magnet wire (i.e. phase) and a metallic grounded plan (i.e. ground) are separated by insulating paper. As expected, according to Paschen's law, it is found that low environmental pressure, with respect to standard sea-level pressure, leads to a PDIV reduction. Similar results were shown in [91], where tests down to 100 mbar pressure were carried out.

The effect of high humidity environment on the PD inception is investigated in [65], where the PDIV of rectangular, enamelled wires is measured under AC voltage and an optical sensor is used for PD detection. In this work, the PDIV measurements are performed after a pre-discharge cycle, which consists in applying a voltage above the PDIV to the specimen for 5 to 60 s, prior starting the PDIV assessment. It was shown that, for low ambient humidity (i.e. 20 %RH), the pre-discharge time duration only slightly influences the PDIV. On the contrary, with 90 %RH, pre-discharge times of 30 s or above, cause an abnormal PDIV increment. Through the electric field distribution calculation (in the gap between the specimens), coupled with the Paschen's curve, the authors demonstrate that the pre-discharge causes the moisture adhesion on the specimens surface. This in turn increases the surface conductivity and influences the electric field strength in the air gap between the wires. Such findings show the importance of the specimens pre-conditioning (aiming at reducing the specimens moisture) prior starting PD measurements. Therefore, according to these findings and prior experience, the specimens adopted in this Thesis, for the experimental investigations, are subjected to prior pre-conditioning.

2.4 Concluding remarks

This Chapter compiles the most relevant literature in the field of aging phenomenology of EMs insulation. It describes the current state of the art and today's main limitations in understanding and analysing these phenomena. Due to the chosen application, namely a PWM-driven, low voltage EM, the principal focus has been on the two main stressing factors, i.e. the thermal and the electrical with some considerations about environmental conditions (i.e. pressure and humidity).

For what concerns thermal stress, the models introduced almost one century ago are still valid and largely employed nowadays. Understanding of electrical stresses related to PD-activity has seen a considerable improvement in the past two decades, especially since an increase in works in this area has been registered from the late 90s onwards. This, of course, coincides with the advent of PWM-driven systems and the havoc they created for the insulation system of EMs.

While it is true that an increasing wealth of works is now available on the understanding of the physical phenomena related to these two stresses, however, it is also true that all these works usually stop at "describing" these phenomena. What is practically non-existent today are the processes of how to use this increasing understanding to actually improve the whole design process of an EM. That is, how and what should EM designers use to always improve their designs from an operational perspective, while at the same time improving or at least not compromising the reliability and lifetime. In other words, how does one develop a reliability-oriented design process using these methodologies?

This is actually what this Thesis aim to do, i.e. to challenge the concept that reliability of an EM is something which is simply checked after an EM has been designed. It is this gap in knowledge about reliability-oriented EM design that this Thesis seek to partially fill, and thus deliver a process that could potentially make a step-change in terms of how EMs are designed and developed.

Chapter 3 Thermal Modelling of Electrical Machines

Since a main part of this work is dedicated to the understanding of insulation thermal stresses, it is an essential pre-requisite to introduce some concepts about the thermal analysis and modelling of EMs. In fact, for insulation thermal lifetime modelling purposes, it is necessary to know the thermal behaviour (i.e. temperature distribution) of the machine according to its application and mission profile. This can be carried out by various thermal modelling approaches. The one preferred and presented in the following of this Chapter is based on the use of lumped parameter thermal networks. The reasons behind this choice are clearly outlined in the following.

After a general introduction on the EM thermal modelling and analysis, two different thermal networks will be presented, namely one suitable for naturally air-cooled EMs and the other one for liquid cooled ones. Such choice is purposely embraced, since in Chapter 4 and 5 these models are employed for predicting the winding hot-spot temperature profile, during the reliability assessment of the presented case-studies.

3.1 Lumped Parameter Thermal Network

EMs design is mainly constrained by three main factors, namely the electromagnetic, the mechanical and the thermal limits. The ever-increasing demand for higher power and torque densities, enabled by advances in materials and design tools, is resulting in the thermal limit nowadays becoming more and more the dominant constraint. For this reason, appropriate thermal management as well as accurate

temperature assessment in EMs are crucial requirements in high performance applications. Several methods can be adopted for the purpose of temperature prediction. These include computational fluid dynamics (CFD), finite element (FE) and lumped parameters thermal network (LPTN) [95]. CFD is generally used when accurate modelling of convection heat transfer is necessary. It requires high computational effort and time for both drawing and meshing the geometry as well as for performing the simulation. Thus, it is generally adopted when the precise prediction of flow in complex regions, such as in the airgap, is required. On the other hand, FE is highly accurate for modelling the heat exchange within solid regions, i.e. when the whole problem is related to thermal conductivity one [96]. FE is therefore very useful for precisely modelling the heat exchange in complex, multi-materials geometries, such as the thermal conductivity within a slot. This necessitates accurate meshing as well as the knowledge of the materials properties.

A faster tool for predicting the temperature distribution within an EM are LPTNs. They are highly affordable tools because of their reduced computational cost and the still relatively high accuracy in modelling heat exchange in both solid and solid/fluid interfaces [97]. Various works exist that highlight how a fine-tuned LPTN can achieve accuracies that are very similar to those obtained by FE models [98-100].

Considering all the above, then this work heavily relies on fine-tuned LPTNs to carry out the thermal analyses required. An LPTN can be seen as a counterpart of an electrical circuit. The analogy between electrical and thermal quantities is reported in Table 3.1.

Table 3.1 – Thermal and electrical counterparts

Electrical	Thermal
Voltage [V]	Temperature [K]
Current [A]	Heat [W]
Resistance [Ω]	Resistance [K/W]
Capacitance [F]	Capacitance [J/K]

The thermal resistances accounting for conduction and convection heat transfers are calculated by (3.1) and (3.2), respectively, where l and A are the thermal path length and cross-section area, while k and h are the thermal conductivity and the convection heat transfer coefficients respectively.

$$R_{cond} = \frac{l}{k \cdot A} \tag{3.1}$$

$$R_{conv} = \frac{l}{h \cdot A} \tag{3.2}$$

The contribution of heat exchange by radiation is generally incorporated in those given by convection [101].

Transient thermal behaviour is taken into account by including thermal capacitances in the LTPN. These capacitances model the material thermal inertia and they are determined by (3.3), where c_p is the specific heat capacity and m_b is the body mass.

$$c_{th} = c_p \cdot m_b \tag{3.3}$$

In an LPTN, heat sources, temperature sources, thermal resistances and capacitances are connected to thermal nodes (or thermal junctions). A node is defined "active" when heat and/or temperature sources are connected to it. Conversely, the junction is referred to as "passive", if only thermal resistances and/or capacitances form the thermal node.

The historical weakness of LPTNs is related to the accurate definition of parameters such as conduction and convection coefficients as well as interference gaps within various EM's components [101, 102]. In absence of experimental measurements, either on the full EM or on custom-built motorettes, these critical parameters are, typically, initially based on previous literature/datasheets, resulting in an imprecise thermal modelling process. However, this is typically overcome through calibration, based on the thermal experimental tests mentioned above. The LPTN critical parameters can be then fine-tuned allowing a precise and computationally-efficient thermal modelling. The experimental fine-tuning is the approach adopted in this Thesis.

3.2 Thermal Model of a Natural Air Cooled Motor

In this sub-section, the LPTN of a natural air-cooled EM for an aerospace electromechanical actuator (EMA) application is presented.

3.2.1 The case-study motor

For this first model, a dual three-phase PMSM for an aerospace application [103, 104] is considered. The machine was designed for driving a helicopter landing gear extension / retraction EMA. Thus, it is aimed at operating under a short duty cycle, as a single activation lasts less than 20 s. Further, given the particular application, between successive activations there is a relatively long cooling-down period, whose duration is inherently related with the helicopter mission profile. The machine geometry and winding layout are shown Figure 3.1, while the main geometrical dimensions and design parameters of the PMSM drive listed in Table 3.2. The PMSM features single layer, concentrated windings and each coil is randomly wound. A single sheet of Nomex® paper is used as slot liner, and the machine is not impregnated.

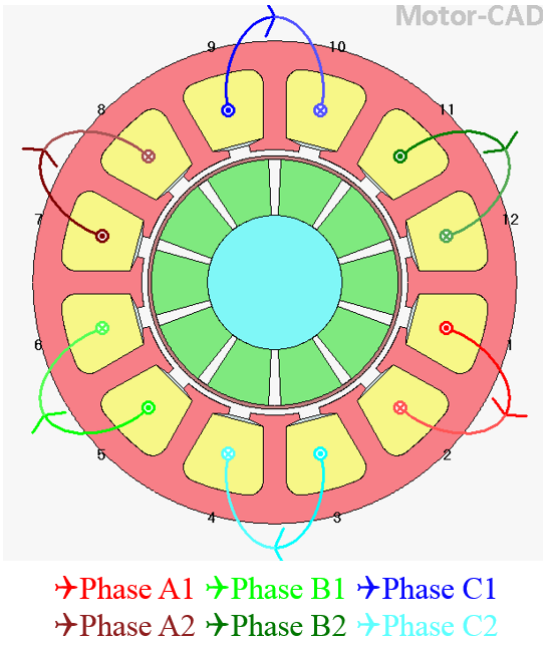

Figure 3.1 – Geometry and winding layout of a PMSM for EMA applications.

Table 3.2 – Main geometrical dimensions of the EMA PMSM.

Design Parameter	Quantity
Slot number	12
Poles number	10
Stator outer diameter	50 mm
Stator bore	27.5 mm
Stack length	60 mm
Copper fill factor	50 %
Cooling	Natural air
Thermal class	200 °C
Magnet wire diameter	0.4 mm
Magnet wire grade	2
Magnet wire insulation	Organic enamel
Secondary insulation	Non-impregnated
Slot liner	Nomex® paper
DC link voltage	270 V
Rated speed	2500 rpm
Rated torque	1 Nm

By exploiting the stator symmetry, the LPTN depicted in Figure 3.2, which models $1/12^{th}$ of the complete EM, is built. Despite the LPTN does not model axial heat transfer, the end winding losses have been added to the slot Joule loss node, so that the model can estimate the hot-spot winding temperature, rather than its average value. Accordingly, the LPTN calibration needs to be performed on the basis of the hot-spot temperature, as done in Section 3.2.3. Given the short-duty nature of the application (i.e. EMA actuator), it is reasonable to assume that the rotor is isothermal (at ambient temperature) throughout the short-time thermal loading, given its thermal inertia [105]. In other words, whilst the winding temperature sharply rises upon current application, the rotor is assumed to stay at its initial, constant temperature. Thus, it is modelled as a temperature source, connected to the stator through thermal resistances representing the air gap. This assumption clearly simplifies the modelling without compromising the temperature prediction accuracy. If the LPTN needs to be re-adapted for a continuous duty machine, then the rotor's thermal network needs to be introduced, alongside with a precise evaluation of the air gap heat transfer.

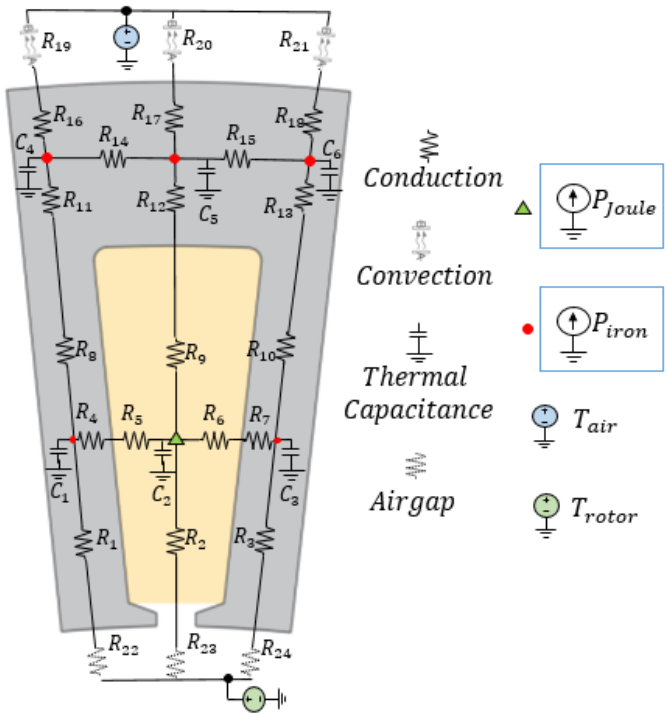

Figure 3.2 – LTPN representing 1/12th of the PMSM for EMA applications.

3.2.2 Modelling with natural air cooling

The heat transfer within the air gap of the machine is modelled through conduction only. This is a conservative assumption as, generally, part of the heat is transferred through the air gap by convection (i.e. lower thermal resistance) when the rotor is spinning. Given the short duty application, this simplification does not compromise by any means the model's accuracy. The circumferential heat flow is considered in the stator back iron. This choice allows to easily re-adapt the proposed LPTN for thermally modelling asymmetrically-loaded machines, where there could be a considerable heat exchange in the circumferential direction. This is the case for e.g. multi three-phase machines operating in active-open configuration, where adjacent coils can be characterised by a large temperature gradient. Figure 3.3 shows an example of a circumferential path with correlated nomenclature. The cross-section area subject to the heat flow can be calculated according to (3.4), while (3.5) is used to determine the equivalent heat path thickness.

$$A = (ro - ri)L \tag{3.4}$$

$$t = \frac{ri + ro}{2}\varphi \tag{3.5}$$

By replacing (3.4) and (3.5) in (3.1), the circumferential thermal resistances of the stator back iron are obtained, as expressed by (3.6).

$$R_{BackIron} = \frac{\varphi \cdot (ri + ro)}{2 \cdot k_{iron} \cdot L \cdot (ro - ri)} \tag{3.6}$$

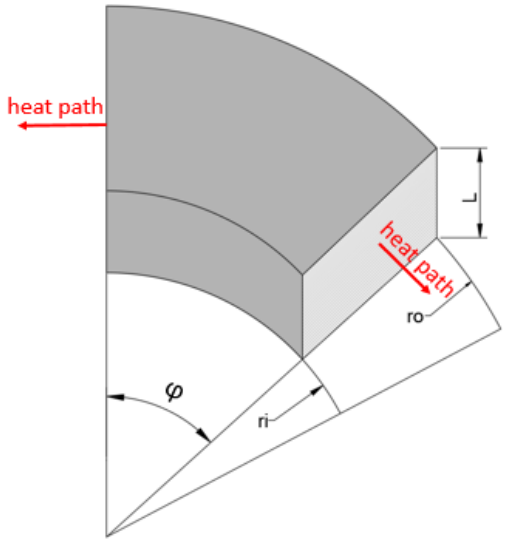

Figure 3.3 – Circumferential heat path in the stator back iron.

The thermal resistances modelling the slot in the radial direction are determined by simplifying the slot geometry to a hexahedron, as depicted in Figure 3.4. By introducing the auxiliary variable z (3.7) and defining the infinitesimal radial resistance (3.8), the equivalent slot resistances (3.9) in the radial direction are determined by integrating (3.8).

$$z = B1 + \frac{B2 - B1}{b}x \tag{3.7}$$

$$dR_{SlotRad} = \frac{dx}{k_{eq} \cdot L \cdot z} \tag{3.8}$$

$$R_{slotRad} = \int_0^b dR_{SlotRad} = \frac{b}{k_{eq} \cdot L \cdot (B2 - B1)} \cdot \ln\left(\frac{B2}{B1}\right) \tag{3.9}$$

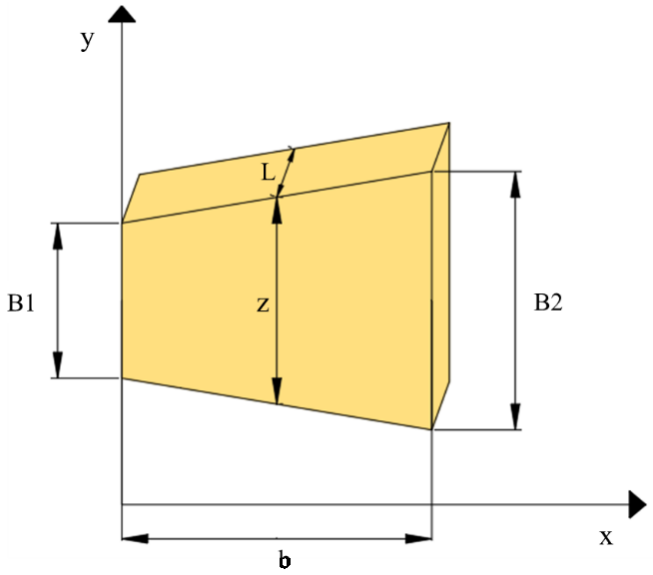

Figure 3.4 – Simplified slot shape.

In General, from a thermal perspective, a slot can be seen as a compound of two materials, namely copper (conductivity k_{cu}) and impregnating resin plus wire enamel insulation (conductivity k_{res}). Therefore, the value of the equivalent slot thermal conductivity is given by (3.10), where *ff* is the fill factor [106].

$$k_{eq} = k_{res} \frac{(1 + ff)k_{cu} + (1 - ff)k_{res}}{(1 - ff)k_{cu} + (1 + ff)k_{res}} \tag{3.10}$$

It is worth pointing out that the thermal conductivity of the wire enamel is similar to the one of the impregnating resin. For this reason, they are both accounted through k_{res}. Consequently, *ff* represents the actual copper fill factor (i.e. ratio between copper surface area and net slot surface area). Since the slot liner has a thermal conductivity approaching k_{eq}, its resistance is also embedded in the slot resistances. In case of non-impregnated winding, k_{res} can be conservatively replaced by the air thermal conductivity (in this case the slot is seen as a copper-air compound). Clearly, an estimation of k_{eq} based only on material datasheets and/or previous literature might lead to erroneous outcomes. Here is the need for experiment informed thermal modelling,

which is the philosophy adopted throughout this work. Namely, the mathematical modelling of thermal parameters is complemented and calibrated by experimental measurements. This should be also the norm when modelling impregnated machines, as, a-priori, is impossible to have a precise estimate of the impregnation goodness factor.

A similar method is used for determining the equivalent thermal capacitance of the slot. The values of the equivalent slot density and specific heat capacity are expressed by (3.11) and (3.12) respectively, where d_{cu} and d_{res} are the copper and resin mass densities, whereas c_{cu} and c_{res} are the corresponding specific heat capacities (the wire's enamel in this case provides a negligible contribution).

$$d_{slot} = d_{cu} \cdot ff + (1 - ff) \cdot d_{res} \tag{3.11}$$

$$c_{slot} = c_{cu} \cdot ff + (1 - ff) \cdot c_{res} \tag{3.12}$$

The copper losses are modelled as a heat source P_{Joule}, whose magnitude is calculated as in (3.13), where n_t is the number of turns per coil, L_{ew} is the (average) end winding length, S_{cond} is the equivalent conductor cross sectional area, $\rho(\theta)$ is the copper resistivity at temperature θ and I_{phase} is the rms value of the phase current.

$$P_{Joule} = \frac{n_t \cdot (L + L_{ew}) \cdot \rho(\theta)}{S_{cond}} \cdot {I_{phase}}^2 \tag{3.13}$$

The resistivity value is automatically updated at each simulation instant (based on the predicted coil's average temperature). Alternatively, various (generally 3 to 4) simulation iterations are necessary for $\rho(\theta)$ to converge to the final, steady-state value.

Iron losses are also modelled as heat sources, and they are obtained from electromagnetic FE simulations. Their magnitude in each stator's region (i.e. tooth or back iron) is proportional to the volumetric loss distribution, which can be easily extracted from commercial FE software. An example of (instantaneous) iron loss distribution (per unit mass) for the PMSM operating at rated condition, obtained through the software Motorcad®, is shown in Figure 3.5. For the machine at hand, iron

losses are more than one order of magnitude lower than Joule losses and thus they provide a minimum contribution to the EM's hot-spot temperature rise.

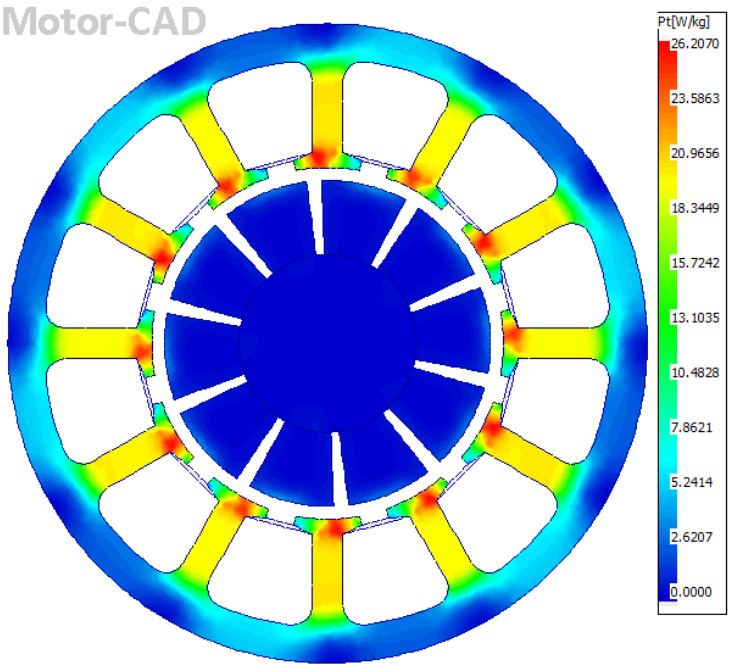

Figure 3.5. Volumetric iron loss distribution for the EMA PMSM operating at rated condition.

3.2.3 LPTN fine-tuning

As explained above, a main aspect of LPTNs is that to achieve accuracy, then some fine-tuning against characteristics obtained through experimental results is required. An accurate temperature estimation can be then obtained. Several parameters are critical in terms of this, and are difficult to be analytically determined. The most important among them are [101, 107]:

- Interference gaps between components
- Equivalent slot conductivity
- Convection heat transfer coefficients
- The uncertainty of material properties
- Heat sources.

For most of the critical parameters, their range of variation can be found in literature [108, 109]. These are empirical values based on previous experience and their range

might result significantly wide for some of them, as listed in Table 3.3. Therefore, selecting the appropriate value is not an easy task, also because it can compromise the LPTN precision. To choose a proper value, while still achieving accurate temperature prediction, the critical parameters are identified relying on experimental findings/data. Generally, for doing so, motorettes representing a portion of the complete machine to be modelled are employed. These should replicate as much as possible both geometry and materials of the complete EM, and needs to be instrumented with thermal sensors distributed in key locations.

In this particular case-study, the measurements were directly carried out on the actual PMSM described in Section 3.2.1, since it was already available and equipped with temperature sensors. The complete test setup is shown in Figure 3.6. The winding temperatures are measured using K-type thermocouples distributed in the coils, and the temperatures are acquired through a data logger. In particular, a total of 16 thermocouples are available and located at various axial positions within the active length of the coils and in the end winding region. Prior starting the tests, the thermocouples providing the hot-spot temperatures within each coil's location (i.e. active length and end winding portion) have been identified.

The tests are performed feeding the machine's coils through a DC power supply. This is the common practice when fine-tuning LPTNs as it enables for a single, well defined source of winding power loss [110]. Further, for the machine at hand it is fair neglecting any AC contribution to the winding loss given the relatively low operating frequency. This might not be the case when modelling very high speed machines, where AC tests can surely provide more precise evaluations. Although iron losses are neglected during the experimental tests, they have been computed via electromagnetic FE analysis and can be easily included in the LPTN. The FE simulation results prove also that the main share to the PMSM losses is given by the Joule losses, confirming the appropriateness of DC tests.

The experimental procedure can be summarised by the following workflow:

1. The PMSM phases are series connected, so that they are subject to the same current during the tests;

2. The DC power supply is connected to the PMSM terminals and the desired DC current value is selected;
3. The temperature profiles measured by the various thermocouples are recorded by the data-logger;
4. The DC current is set to zero once the machine has reached the steady state temperature.

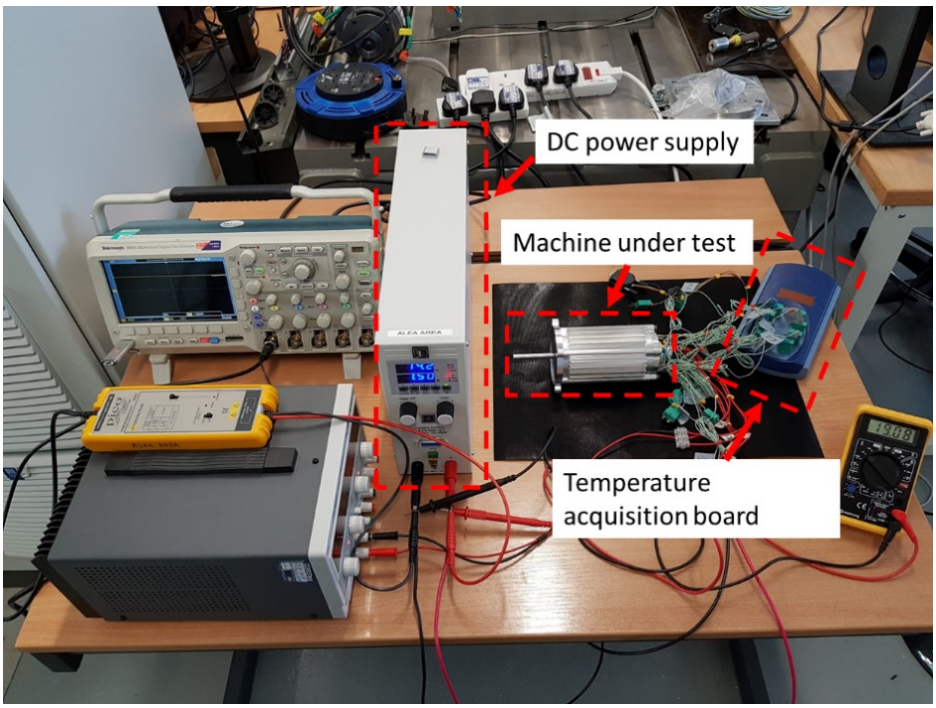

Figure 3.6 – Experimental setup for the LPTN fine tuning.

Table 3.3 – Critical thermal parameters for the analysed PMSM.

Parameter	Variation Range [108, 109]	Experimental
Equivalent slot conductivity [W/m/k]	0.5-2	0.45
Natural air convection coefficient [W/m^2/k]	5-30	5
Equivalent slot specific heat [J/kg/K]	400-1 k	400
Equivalent slot mass density [kg/m^2]	4-5 k	4160

The LPTN fine-tuning has been dealt with the Simulink Design Optimisation™ toolbox. This tool allows the user to import and pre-process the recorded temperature profiles. Then, it executes estimation of the critical thermal parameters by a sequential quadratic programming (SQP) algorithm. Such an algorithm aims to minimise the error between the measured temperatures and those predicted by the LPTN. In practice, the

critical parameters are varied within a user-defined range until the sum-squared error between measured and predicted temperatures are minimised. Thus the optimised values of the critical parameters are assumed to be those which best reflects the actual thermal parameters of the real machine. Experimental and predicted hot-spot temperatures are evaluated for several DC current values. In Table 3.3, the critical parameters (experimentally obtained) are compared with their range of variation proposed in literature, and a good fitting is revealed. It is possible to observe that the equivalent slot conductivity (i.e. radial and circumferential directions) is 0.45 W/m/K, which is below the range provided by literature. This because the tested PMSM is not impregnated leading to a low thermal conductivity according to (3.10). The term "equivalent" here refers to a single "virtual" material, which thermally behaves as the copper / enamel / air compound found in the actual machine. The calculated thermal coefficients can then properly tune the LPTN. The comparison between experimental and LPTN estimated winding temperature profiles (i.e. hot-spot temperature) is reported in Figure 3.7, where two current values are considered, namely rated and twice rated current. The obtained temperature profile(s) refers to an ambient temperature of 23 °C, which is also the initial temperature set in the LPTN's thermal capacities. It is worth recalling that the machine is naturally air-cooled. The tests refer to a DC (rated) current of 1.1 A, and a phase resistance of 3.24 Ω at 23 °C.

In the worst case, a maximum relative error below 5% is observed. Since the PMSM is intended for short-time duty cycle application (i.e. EMA actuator), the time window of Figure 3.7 is limited to 500 s, which, nonetheless, is well above the operation time of the analysed machine (i.e. <60 s for three full extensions/retractions in a row).

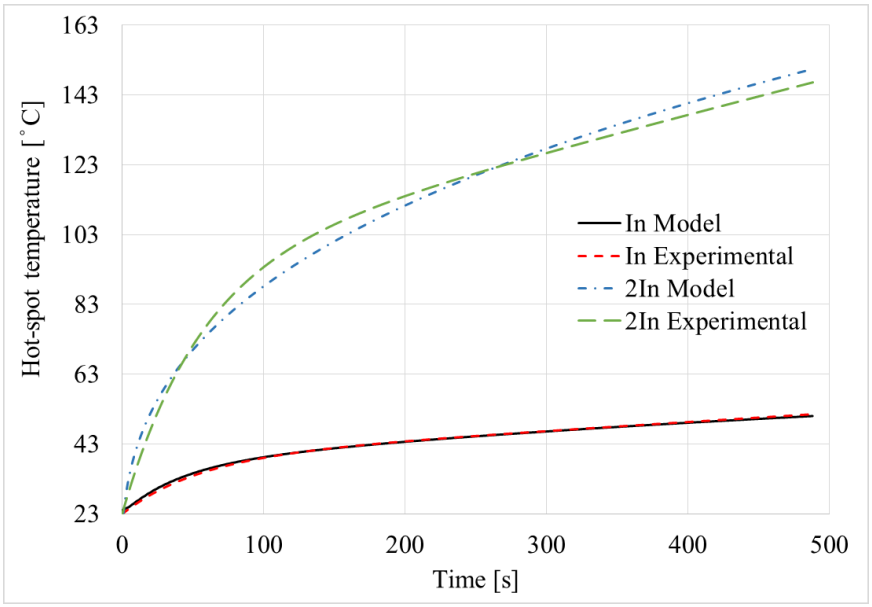

Figure 3.7 – Comparison between measured and estimated winding temperature profiles at different current levels.

3.2.4 Considerations an limits of the LPTN

It is important to note that actually a lower order LPTN (i.e. reduced number of nodes) could have been used for the analysed machine, due to the short-time duty cycle of the considered application. Indeed, the duty cycle duration is more than one order of magnitude lower than the PMSM thermal time constant. The thermal time constant for the analysed machine is about 900 s, while its duty cycle is equal to 20 s (i.e. time for a single EMA activation). However, the proposed LPTN structure has a more general validity and can be employed for studying the thermal behaviour of machines operating under longer duty cycles, up to the time interval within the LPTN fine-tuning was performed (i.e. 500 s). Furthermore, isothermal (and geometrically-symmetrical) nodes can be merged and equivalent parallel/series resistances and capacitances can be easily computed. However, the proposed LPTN, with some basic modifications, can be used for the thermal analysis of asymmetrically-loaded EMs i.e. machines where adjacent slots can experience a different thermal loading (such as dual three-phase EMs operating in active-open mode). This can be easily done by circumferentially connecting two identical duplicates of the proposed LPTN (i.e., these will share a

common tooth). Thus, during asymmetrical operations heat can be transferred from the most thermally loaded slot to the less thermally loaded one.

The implemented LPTN is built assuming a) the PMSM rotor isothermal and b) only conductive heat transfer is taken into account within the air gap. However, it is noteworthy that such assumptions may affect the accuracy of the steady-state temperature prediction. Indeed, for naturally air-cooled machines, a non-negligible portion of heat (produced within the stator) is transferred to the rotor across the air gap and the rotor itself is a source of heat because of the losses, particularly within the PMs region. This heat flow is axially extracted from the machine via a low thermal resistance path represented by the rotor shaft. For this reason, the rotor structure needs to be modelled in the LPTN, along with the convective heat transfer in the air gap, when the steady-state temperature evaluation is critical (i.e. continuous running duty).

For simplification purposes, the axial heat exchange has been neglected, both in the copper coils and in the stator core (the latter is anyway uninfluential). This reduces the number of convection heat transfer coefficients to be experimentally fine-tuned, as the internal end-cap area is not modelled at all. However, the Joule losses generated in the end-winding region have been included in the single winding node, localised in the slot centre. In principle, it would have been possible to assume that all the heat generated within the end-winding was to be dissipated through natural convection to the internal end-cap area, and therefore avoid the inclusion of an additional loss contribution in the slot node. However, as the objective was to estimate the winding hot-spot temperature, rather than its average value, concentrating the Joule loss in a single node allowed to slightly increase the LPTN-predicted winding temperature. This without modifying excessively the fine-tuned critical parameters, and thus maintaining their magnitude within an acceptable, physically meaningful range.

In the presented modelling procedure, the thermal resistances accounting for interference gaps between the stator back iron and the frame (i.e. housing), plus the frame thermal resistances have been added in the thermal resistances R_{16}, R_{17} and R_{18}. Similarly, the frame thermal inertia is determined through the iron thermal capacitances C_4, C_5 and C_6. Due to these choices, the temperature distribution in the PMSM frame

is not as accurate as the one resulting from an LPTN which separately models both frame and interference gaps' thermal resistances. Despite the poor estimation of the frame temperature, the proposed LPTN allows to precisely predict the PMSM hot-spot temperature (i.e. winding temperature), as proven by the results shown in Figure 3.7. Considering that the most critical data for thermal insulation lifetime prediction and modelling purposes is the winding temperature, then the LPTN proposed above is deemed to be highly appropriate for the task at hand.

3.3 Thermal Model of a Liquid Cooled Traction Motor

In this sub-section the LPTN of a forced-liquid cooled EM for an automotive application will be presented discussed. The aim is to estimate the winding hot-spot temperature necessary for the insulation lifetime prediction purposes.

Liquid cooling is generally preferred to both natural and forced air cooling for machines characterised by higher current density levels. In this case, cooling methods are classified in direct and indirect, according to whether or not the coolant is in direct contact with the heat source (i.e. winding). Common direct liquid cooling methods are spray evaporative cooling [111, 112], flooded or semi-flooded stators [113] and embedded liquid-carrying pipes within electrical conductors [114]. On the other hand, the most widely adopted indirect liquid cooling method, largely employed in the automotive sector, is represented by a water jacket embedded within the EM's housing [115, 116].

3.3.1 The machine at hand

The machine is a 30 kW, 12 slot / 10 pole PMSM and it was originally designed for a hybrid-electric car [117, 118]. Its cross sectional view is shown in Figure 3.8, while the main geometrical dimensions and parameters are reported in Table 3.4. Contrarily to the landing gear EMA presented in the previous Sections, the automotive PMSM is designed for continuous duty operations, with frequent overloads.

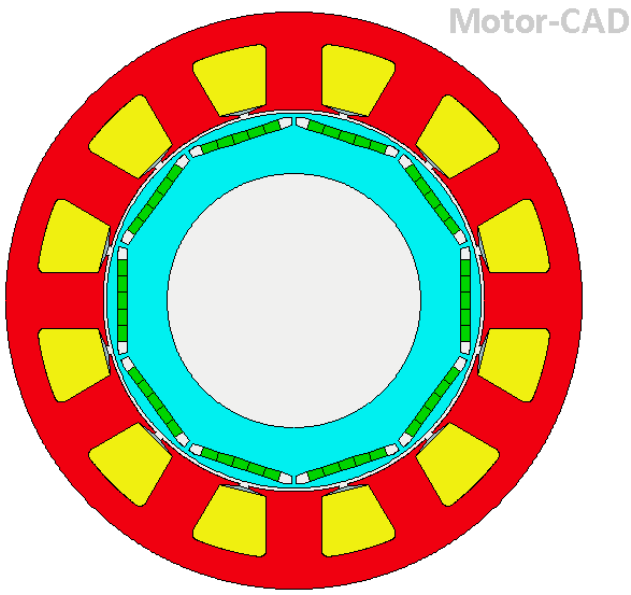

Figure 3.8 – Geometry of the traction PMSM.

Table 3.4 – Main geometrical dimensions of the traction PMSM.

Design Parameter	Quantity
Slot number	12
Poles number	10
Stator outer diameter	250 mm
Stator bore	165.5 mm
Stack length	200 mm
Copper fill factor	45 %
Cooling	Liquid water jacket
Thermal class	200 °C
Magnet wire diameter	1 mm
Magnet wire grade	2
Magnet wire insulation	Organic enamel
Slot liner	Nomex® paper
DC link voltage	540 V
Rated speed	2800 rpm

The PMSM is cooled through a housing water jacket plus two additional silicone cooling pipes embedded in the EM end-winding [117]. Figure 3.9 depicts how maximisation of the contact area between pipe and end-winding is achieved with the latter being split into upper and lower sections. The hydraulic circuit for the complete cooling system is schematised in Figure 3.10. Since the PMSM shares the same cooling system of the internal combustion engine, a water flow rate of 10 L/min is available from the radiator unit (i.e. heat exchanger). The overall water flow rate is split between

the housing water jacket (i.e. 6 L/min) and the two end-windings sides (i.e. 2 L/min each) by using a flow regulator.

The application of the end-windings cooling pipes was proposed, explained and validated for the first time in [117]. This novel cooling methodology allows a noticeable hot-spot temperature reduction in the EM's winding, bringing considerable performance improvements in terms of peak torque and power densities. Another advantage resulting from lowering the winding temperature is the insulation's lifetime extension. This aspect will be detailed in Chapter 5.

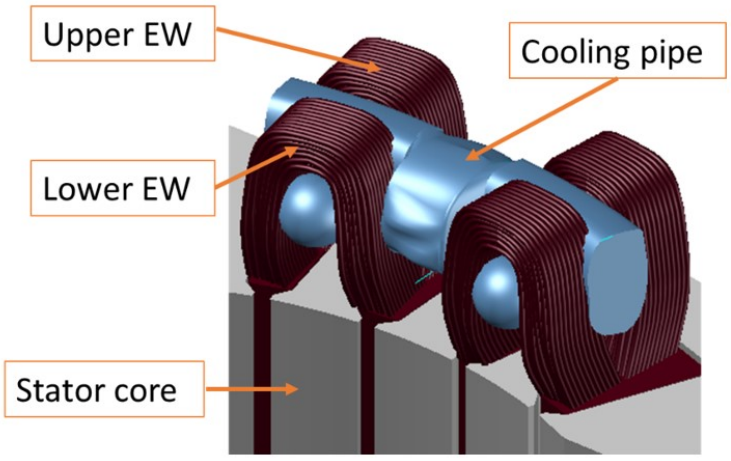

Figure 3.9 – End-winding cooling through liquid-carrying pipe.

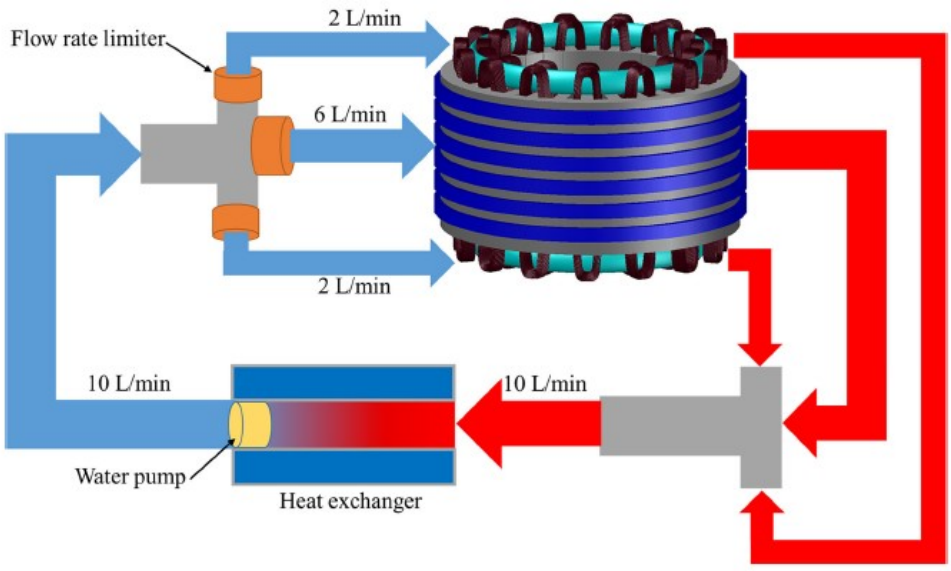

Figure 3.10 – Complete hydraulic circuit of the traction PMSM.

A 7-nodes LPTN is built for thermally modelling the PMSM as shown in Figure 3.11. The list of each thermal element as well as their description are reported in Table 3.5. The number of nodes that results in an optimum between accuracy and use of computational resources is selected according to a sensitivity analysis exercise. This analysis was performed by following the steps listed below:

1. Initially the PMSM's temperature is estimated using a more complex 78-nodes LPTN, built adopting the standard procedure reported in Sections 3.1 and 3.2.
2. The isothermal nodes (i.e., nodes at the same temperature whose mismatch is in the range ± 3 °C) within the same machine volume (e.g. slot, tooth etc…) are merged.
3. Only the nodes representative of hot-spot temperatures, according to the simulation's outcome of the highly discretised 78-nodes LPTN, are kept for each machine's portion.
4. Equivalent resistances/capacitances are determined by series/parallel computation.

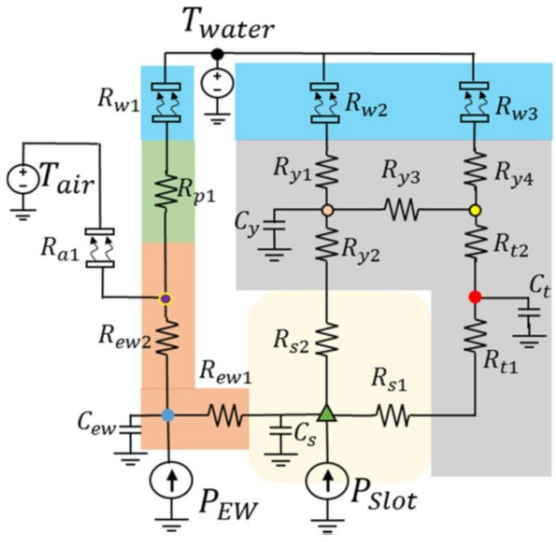

Figure 3.11 – 7-Nodes LPTN of the traction PMSM.

Table 3.5 – Thermal resistances (R) and capacitances (C) used in the 7-nodes LPTN

Component	Description
R_{s1}	Tangential slot
R_{s2}	Radial slot
R_{y3}	Tangential yoke
R_{y1}, R_{y2}, R_{y4}	Radial yoke
R_{t1}, R_{t2}	Radial tooth
R_{p1}	Pipe + Contact pipe / end-windings
R_{ew1}, R_{ew2}	End-windings
R_{w1}	Pipe / Cooling fluid convection
R_{w2}, R_{w3}	Water jacket / stator convection
R_{a1}	Convection end-windings / air
C_s	Slot
C_y	Yoke
C_t	Tooth
C_{ew}	End-windings

The obtained LPTN computes both radial and axial heat transfer. Indeed, given the particular end-winding cooling arrangement, part of the heat produced within the slot is transferred and extracted by the end-winding cooling pipe. With the purpose of validating and tuning the LPTN the instrumented motorette shown in Figure 3.12, which is equipped with the housing water jacket and the silicone pipe, was manufactured. In addition a total number of 7 thermocouples are uniformly distributed within the active region of the winding as well as the in the end winding area. An additional thermocouple is used for measuring the coolant temperature. Among these thermocouples, those providing the highest temperature (i.e. hot-spot) for both slot and end winding are selected for calibrating the LPTN. For this particular case-study it has been purposely decided to carry out the tests on an instrumented motorette rather than on the full machine. This represents the less time-consuming and more economically convenient option when evaluating a newly designed prototype, and does not compromise by any means the validity of the study. Further, the same motorette has been exploited for quantifying the cooling benefits of different end winding pipe materials. Such an evaluation would have been extremely complex on a fully assembled machine.

The experimental calibration is again carried out by feeding the winding through a DC power supply, for the same reasons detailed in Section 3.2. The Simulink Design

Optimisation™ toolbox is employed for calibration purposes, similarly to the aerospace EMA machine's LPTN tuning. The comparison between measured and LPTN-predicted hot-spot temperatures is reported in Figure 3.13. These have been obtained with ambient and coolant temperatures both at 30°C, and by feeding the winding through a 40 A DC current (i.e., 315 W total Joule losses). The LPTN's results match within a 5% error the experimentally-recorded temperature profiles, during both transient and steady-state operations.

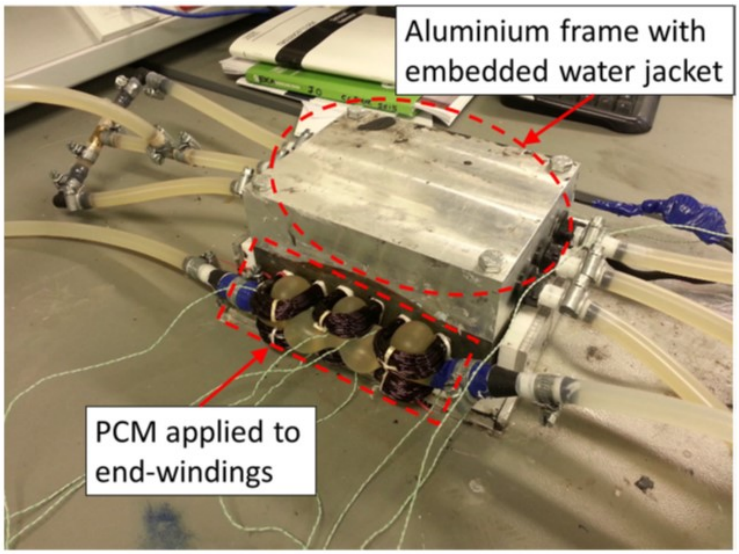

Figure 3.12 – Instrumented motorette used for the traction motor's LPTN tuning/validation.

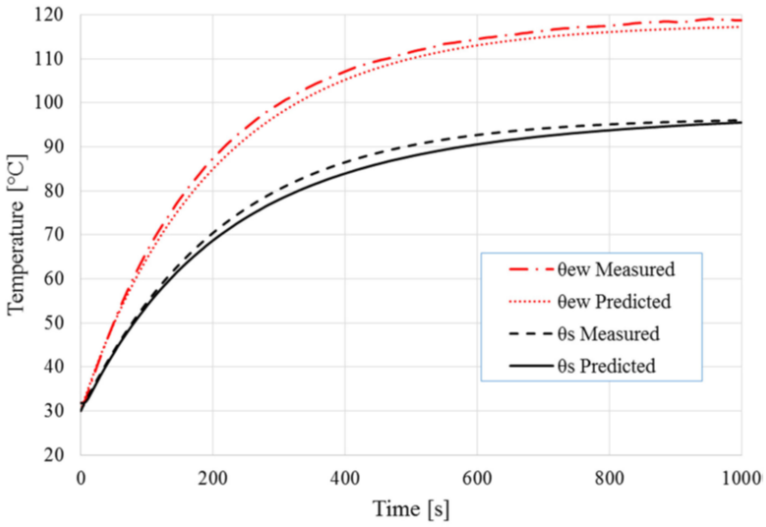

Figure 3.13 – Measured vs. LPTN-predicted hot-spot temperature profiles for slot (s) and end-winding (ew).

A more detailed description of the LPTN tuning procedure and a trade-off study among pipe's materials is reported in [117], and it is purposely omitted here, as it is slightly out of the main topic of this Thesis.

3.4 Concluding remarks

In this Chapter, basic concepts behind the thermal modelling of EMs via LPTNs are introduced. The advantages of LPTN methods over more "computationally expensive" thermal modelling techniques have been briefly discussed. Two different examples of LPTNs, for air- and liquid-cooled EMs have been built and fine-tuned which will be employed in the remainder of this Thesis.

The importance of this Chapter for the whole "flow" of the work in this thesis cannot be underestimated. The analyses in this Chapter, basically, "sets the scene" for the rest of the work of this PhD. The modelling methodologies and the basic methods introduced in this Chapter, for precise temperature estimation of EMs windings are an essential pre-requisite for the insulation lifetime assessment/prediction methodologies that are proposed and validated later in this Thesis. It is the hot-spot temperature profile defined by the work in this Chapter 3 that is the main input to the insulation's thermal lifetime prediction models of Chapter 4 and Chapter 5. All this can be visually appreciated in Figure 1.4, which clearly shows the mentioned links.

On the other hand, this Chapter has also been the source for "stand-alone" contribution to research. It has resulted in 3 journal papers [103, 117, 119] and 4 conference papers [104, 120-122]. One of the conference papers [122] was honoured with the Brian J. Chalmers Best Paper Award in 2018.

Chapter 4 Thermal Aging in Continuous Duty Electrical Machines

From this Chapter onwards, the Thesis will be mainly focusing on experimentally investigating the physics of failure of electrical insulating systems. The final aim, based on these investigations, is proposing a novel reliability-oriented design procedure for electrical machines. This Chapter, in particular, explores the influence of thermal aging in low voltage random wound electrical machines operating under a continuous duty (i.e. constant temperature). These are commonly found in industrial applications, but some excellent examples are also encountered in transport applications. Continuous duty machines in transportation include (but are not limited to) fuel pumps, compressors and fans for environmental control, and to some extent traction motors (although the latter can also experience periodic overloads).

Starting from the life modelling and reliability assessment for continuous duty machines represents the most logical choice. Both because this analysis is relatively simpler - as opposed to variable duty ones - and because part of the experimental data and analyses presented throughout this Chapter will be re-called in Chapter 5. At the same time, this Chapter makes use of the temperature prediction method, through lumped parameter networks, discussed in Chapter 3. The presented analysis is strongly linked to experimental tests, carried out on custom designed specimens, with the purpose of obtaining life data as representative as possible to a complete “real” machine. The experimental results are post-processed via statistical analysis and the obtained data are used for proposing and tuning an insulation lifetime prediction model. This model is then exploited to assess the reliability of a continuous duty, aerospace machine, which is chosen as a case-study.

4.1 Problem Definition

Thermal constraints represent one of the main performance-limiting factors in modern EMs. In fact, the torque-producing capability of an EM is limited by the maximum temperature at which some of its components can operate. PM demagnetisation is dependent on temperature, however modern commercially available PMs, today can reach temperature ratings of more than 300 °C. Therefore, the maximum operating temperature of an EM is usually defined by the thermal class of its weakest insulating sub-system. In low voltage, random wound EMs the latter is generally the magnet wire [20, 21, 43, 123], since it is insulated by a thin organic enamel layer (i.e. Type I insulation).

Operating an EM at temperatures as close as possible to the insulation thermal class limit, can maximise its torque/power density. This implies the importance of:

a) precise estimation/measurement of the winding hot-spot temperature;
b) knowledge of the EM's thermal limit;
c) knowledge of the insulation lifetime consumption/degradation process associated with high temperature operations.

While point a) has been discussed in Chapter 3, the following sections focus on b) and c) and do this through an experimental investigation. The main objective of this Chapter is then to combine the knowledge of all three points above and thus develop a lifetime model able to predict the insulation's time to failure for low voltage EMs operating under continuous duty (i.e. constant temperature).

4.2 Thermal Accelerated Aging Tests at Constant Temperature

A common strategy for evaluating the thermal lifetime of insulating systems is based on accelerated aging tests. This procedure consists in testing the product (in this case the insulation system) at high stress conditions with respect to "normal" service

operations to yield failures quickly [124]. When temperature is the aging/stress factor, (at least) three sets of specimens need to be tested [125, 126]. Each set should be aged at a different temperature, higher than the expected thermal class. This allows to extrapolate through regression or other fitting procedures the Arrhenius plot or thermal endurance curve of the insulation. An end of life criterion, necessary for determining the specimen's failure, needs to be defined before starting the testing campaign.

For the whole procedure to be valid, it is necessary that the chosen aging temperatures do not cause secondary degradation effects / reactions within the material. Indeed, the Arrhenius model stays valid as long as the specimens' temperature does not exceed a critical value, after which secondary chemical reactions could be incepted (i.e. multiple activation energies). Technical standards dealing with the thermal qualification of insulating systems and materials [38, 125] generally provide a range of temperatures suitable for these evaluations.

4.2.1 Specimens Description

Common specimens employed for the evaluation of the turn to turn insulation in low voltage EMs are twisted pairs, coils and motorettes. The terms "motorette" and "formette" are conventionally used by technical standards for describing a portion of the complete EM. A specimen should replicate as closely as possible the actual insulation sub-system to be analysed. This means that tests performed on the actual EM should provide the most accurate estimate. However, for guaranteeing an appropriate statistical significance on the tests results, it is necessary to age a relatively large number of test objects (i.e. large sample size). Thus, it would be economically unsustainable and time consuming to carry out accelerated aging tests on complete EMs. Here is the need for identifying which specimen typology can guarantee a fair trade off between life estimation accuracy and economic/time burden, as shown in the following paragraphs.

In this work, three different specimen topologies are analysed, namely, twisted pairs, random wound coils and motorettes as shown in Figure 4.1, and their suitability for interturn thermal lifetime evaluation purposes is apprised. Details regarding the

adopted magnet wire for the three specimen topologies are reported in Table 4.1, while the Arrhenius plot provided by the wire's manufacturer is shown in Figure 4.2. The latter is obtained according to the TS IEC 60172 [127], where twisted pairs are adopted for the curve extrapolation. Accordingly, the twisted pairs specimens feature 16 twists covering a distance of 120 mm [127].

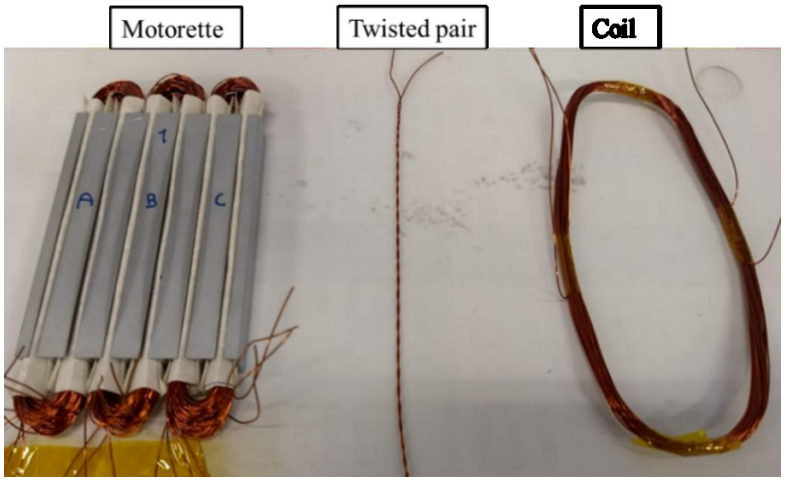

Figure 4.1 – Specimens used for the thermal accelerated lifetime tests.

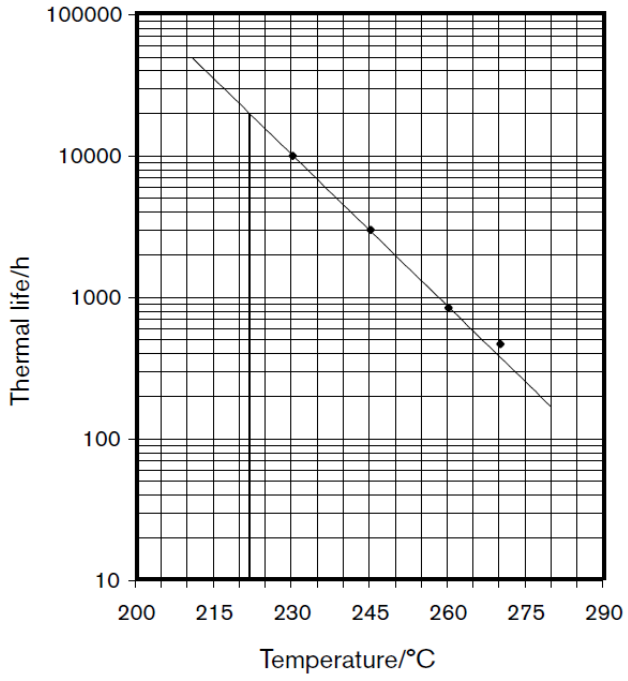

Figure 4.2 – Thermal endurance plot of the used magnet wire (manufacturer).

Table 4.1 – Properties of the adopted magnet wire.

Parameter	Property
Copper diameter	0.400 mm
Grade	2
Thermal class	220
Base coat insulation	Polyester-imide
Over coat insulation	Polyamide-imide

Each of the manufactured motorettes has three wound teeth with a total of 6 subcoils counting 20 turns each as illustrated in Figure 4.3. Since each subcoil has two strands, the turn to turn insulation condition can be assessed by performing the dielectric measurements on the interstrand insulation. The strand to strand insulation corresponds to the turn to turn one (i.e. layer of organic enamel), in low voltage random wound EMs. Therefore, measuring the dielectric properties of the strands insulation is equivalent to evaluate the turn to turn insulation condition. Thus, a single motorette embeds 6 specimens (i.e. 6 subcoils) and the average coil length is 240 mm. The motorette represents one half of the aerospace EMA motor presented in Chapter 3 (cfr. Figure 3.1 and Table 3.2). The winding layout is chosen for increasing the number of specimens (i.e. subcoils) in a single motorette, and thus maximising the sample size.

As for the motorettes, also the coils adopt the same winding configuration based on two parallel strands. These are kept together by Kapton® tape, which is only used for mechanical purposes. In this case, the average coil length is 300 mm and the number of turns is 20.

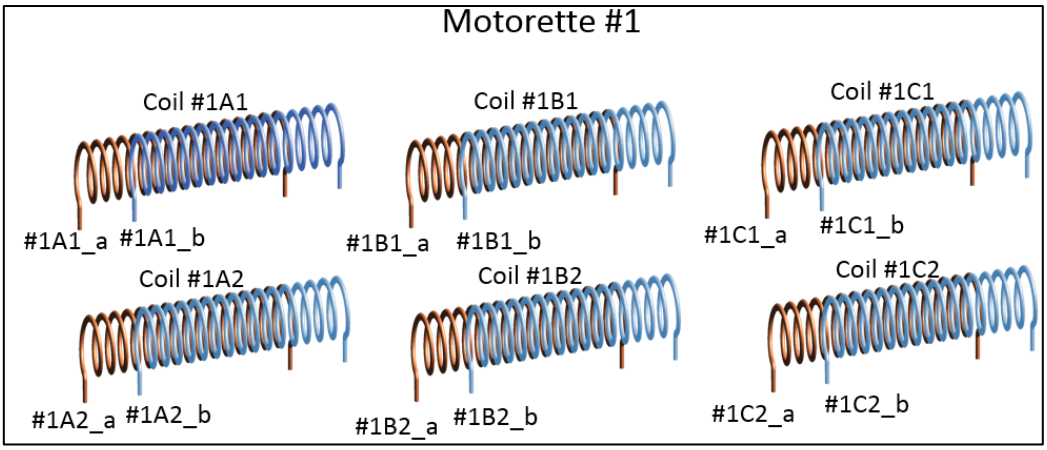

Figure 4.3 – Motorette's winding layout.

4.2.2 Test Campaign Description

Since the results from accelerated aging tests can have relatively large statistical variations, the number of tested specimens, for each aging temperature, can influence the results accuracy. In principle, from a statistical point of view, larger sample sizes are almost always preferred to smaller ones, as this reduces uncertainties and narrows confidence bands. However, from the engineering side, there are various reasons for minimizing the number of tested specimens. Firstly, the time and cost for manufacturing the specimens can be significant - also considering that each specimen is discarded after the evaluation campaign is completed. In addition, a larger sample size implies also longer diagnostic sessions, leading to extra time needed for the whole evaluation procedure. In general, both IEEE [125] and IEC [38] technical standards consider appropriate a minimum sample size of 5 to 10 for each stress level (i.e. temperature for thermal aging and voltage for electrical aging) [40].

In this work, a total of 15 motorettes, 36 twisted pairs and 36 coils identical to the ones shown in Figure 4.1 have been manufactured and wound. As the main aim of this particular study is investigating the thermal life performance of the turn to turn insulation, the specimens are not impregnated. This might not exactly replicate the layout of a real EM, where the winding impregnation through resins or varnishes is the common practice. However, particularly for random wound EMs it is very likely that two adjacent turns within a coil are in direct contact, even after the impregnation process. Further, as the in-service EM thermally ages, volatile substances are released from the resin / varnish as the substance depolymerises, leading to a progressively decreasing impregnation goodness, and thus enhancing the probability of different turns being in direct contact. Clearly, if the purpose is investigating the chemical interaction and compatibility between resin and wire enamel materials at high temperature, the specimens need to be impregnated, however, this goes beyond the main objectives of this work.

Performing the tests on three different specimen typologies aims in investigating if the specimen's layout has an impact on the obtained lifetime data, as

well as showing which layout provides the most conservative life estimate. These have been divided in three sets, each comprising 5 motorettes (i.e. 30 sub-coils), 12 twisted pairs and 12 coils. In order to determine the Arrhenius plot, for every specimen topology, each set should be aged at a different temperature above the magnet wire thermal class, that is 220 °C. The three chosen aging temperatures are 250, 270 and 290 °C. For each of the three selected temperatures, a number of thermal exposure cycles, whose time-durations are reported in Table 4.2, have been carried out. The flow-chart of the test campaign is reported in Figure 4.4.

Table 4.2 – Duration of the thermal exposure cycles.

Temperature [°C]	Exposure cycle duration [h]
250	120
270	24
290	8

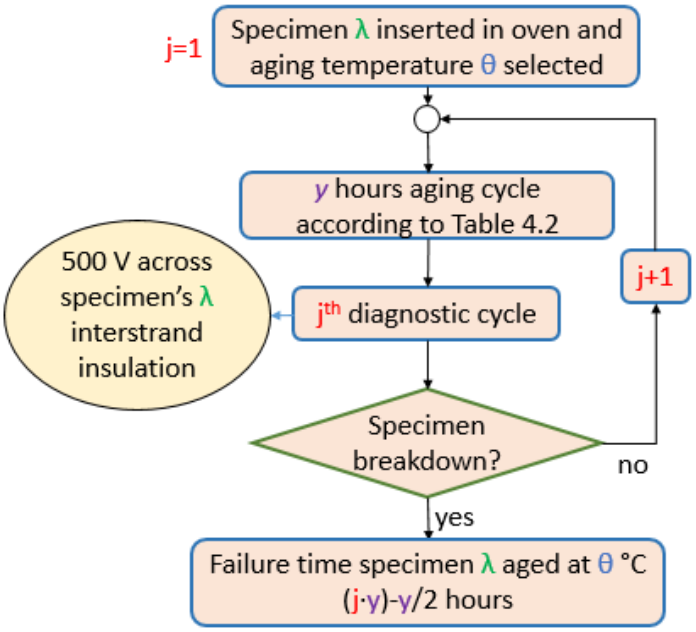

Figure 4.4 – Flow-chart of the testing campaign.

The accelerated aging campaign is preceded by a pre-conditioning cycle, which aims at removing both volatile substances as well as impurities that might be present on the wire's enamel surface. The pre-conditioning cycle consists in a thermal exposure session of 12 h at 220 °C (i.e. wire thermal class). This has minimum or no influence

on the outcome of the accelerated thermal aging tests, but it is necessary if particular dielectric measurements and insulation diagnostic markers need to be recorded throughout the various diagnostic sessions [128].

The thermal exposure cycle durations (i.e. y in Figure 4.4) have been selected according to the Montsinger's law [cfr. Equation (2.3)] [44]. To enhance the statistical significance of the predicted time to failure, the number of diagnostic sessions (i.e. j of Figure 4.4) should be comprised between 10 and 20 [125]. Thus, the thermal exposure time (in hours) can be calculated by the relationship given in (4.1), where θ_i is the temperature considered during the ith accelerated aging test (i.e. θ^i>*class*), j is the number of desired diagnostic sessions (between 10 and 20) and *class* is the thermal class (i.e. temperature that guarantees at least 20,000 working hours).

$$ExpTime_{\mathrm{i}} = 20{,}000 \cdot 2^{\frac{class-\theta_i}{10}}/j \tag{4.1}$$

Relying on (4.1), the exposure times of 8, 24 and 120 hours have been obtained for the aging temperatures 290, 270 and 250 °C respectively.

Throughout the diagnostic cycles, the specimen's failure is detected through the AC Hipot test. Namely, a 500 V rms voltage is applied to the strand to strand insulation (e.g. between the terminals "#1A1_a" and "1A1_b" of the winding layout shown in Figure 4.3). Thus, the end of life criterion is the electric breakdown. Therefore, the presented analysis is valid for EMs operating in a PD-free regime throughout their whole lifetime (e.g. the PMSM EMA presented in Section 3). Nonetheless, the introduced testing procedure can be re-adapted by choosing various end of life criteria suitable for different electric drives topologies. The voltage level used for the AC Hipot test (i.e. 500 V rms) allows to directly compare the obtained experimental lifetime data with the Arrhenius curve provided by the magnet wire manufacturer. Indeed, this voltage level is suggested by the TS IEC 60270 [92] for the magnet wire at hand.

4.2.3 Test Campaign Results

The two-parameter Weibull distribution has been used for post-processing the experimentally-recorded failure times. The Weibull cumulative distribution function (CDF) can be described as in (4.2), where t is the time to failure, α is the scale parameter and β is the shape parameter.

$$F(t) = 1 - \exp\left[-\left(\frac{t}{\alpha}\right)^{\beta}\right] \tag{4.2}$$

In particular, α is the 63.2% percentile of time to failure, while β represents the inverse of the data scatter, which is proportional to the variance of the failure times. For estimating α and β, the recorded failure times data are rearranged in ascendant way, whereas (4.2) is linearized by taking the natural logarithm twice, as expressed in (4.3), where t_i is the i_{th} time to failure.

$$\ln\left[ln\left(\frac{1}{1 - F(t_i)}\right)\right] = \beta \ln(t_i) - \beta \ln(\alpha) \tag{4.3}$$

As a consequence of the linearization, (4.3) represents the general equation of a straight line having β as gradient (i.e. slope) and $\beta ln(\alpha)$ as intercept on the y-axis. For the sake of clarity, (4.3) is rewritten as in (4.4).

$$Y(t_i) = \beta \ln(t_i) - \beta \ln(\alpha) \tag{4.4}$$

The Weibull CDF - $F(t_i)$ - at the time to failure t_i is evaluated using the median rank estimator, which is given by Bernard's approximation (4.5), where n is the sample size (i.e. the number of specimens) [129].

$$\hat{F}(t_i) = \frac{i - 0.3}{n + 0.4} \tag{4.5}$$

By plotting $Y(t_i)$ versus $ln(t_i)$, it is possible to obtain α and β through a linear regression.

The Weibull probability plots of failure times, with 95% confidence intervals, for the three analysed specimens, and for each of the three aging temperatures are

reported in Figure 4.5, Figure 4.6 and Figure 4.7 for twisted pairs, coils and motorettes respectively. Table 4.3 summarizes the obtained results.

Table 4.3 – Results summary of the accelerated thermal aging tests.

Parameter	**Twisted Pairs**			**Coils**			**Motorettes**		
	250 °C	*270 °C*	*290 °C*	*250 °C*	*270 °C*	*290 °C*	*250 °C*	*270 °C*	*290 °C*
α [h]	1943	415	111	640	251	64	1307	319	78
β	2.73	3.67	5.93	2.97	4.33	2.60	3.08	4.56	1.61
Median [h]	1699	375	104	571	230	56	1161	295	70

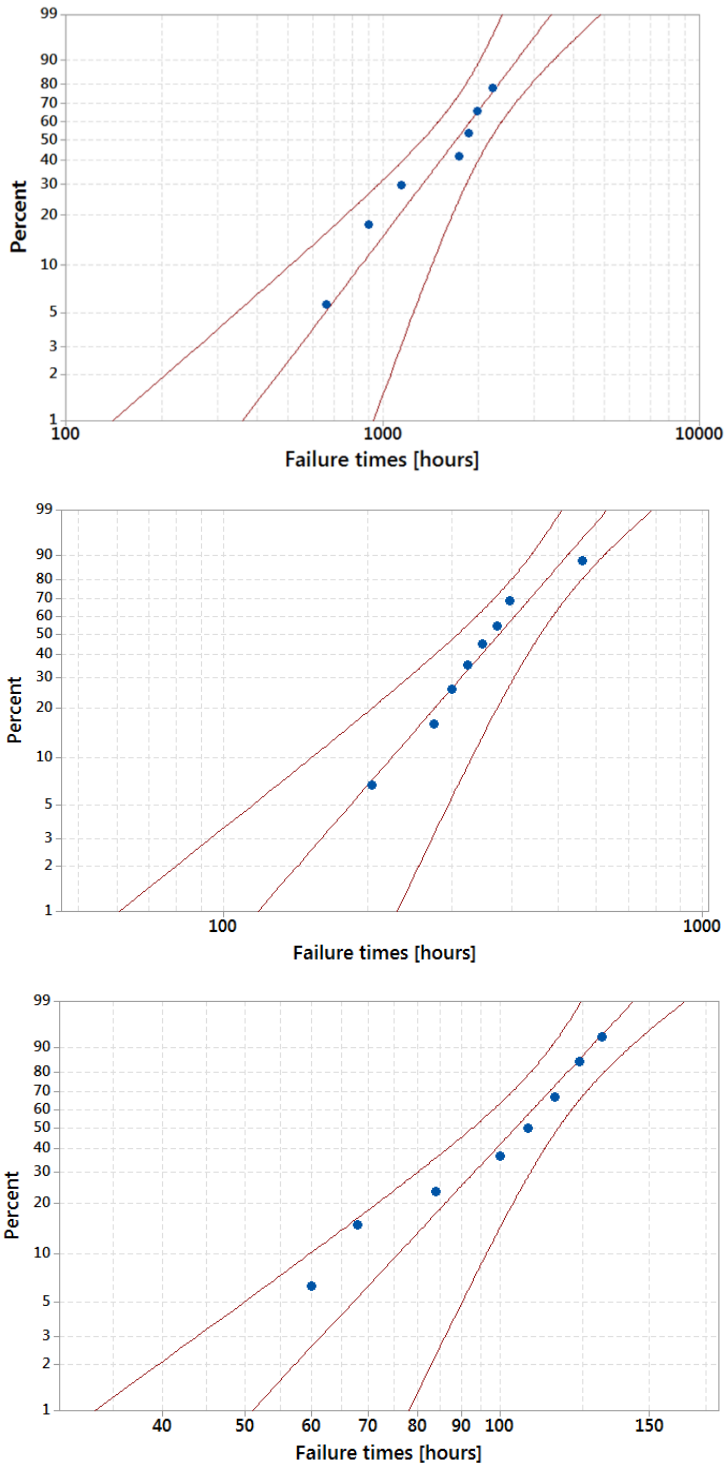

Figure 4.5 – Weibull probability plot of failure times for twisted pairs aged at 250 °C (top sub-plot), 270 °C (middle sub-plot) and 290 °C (bottom sub-plot).

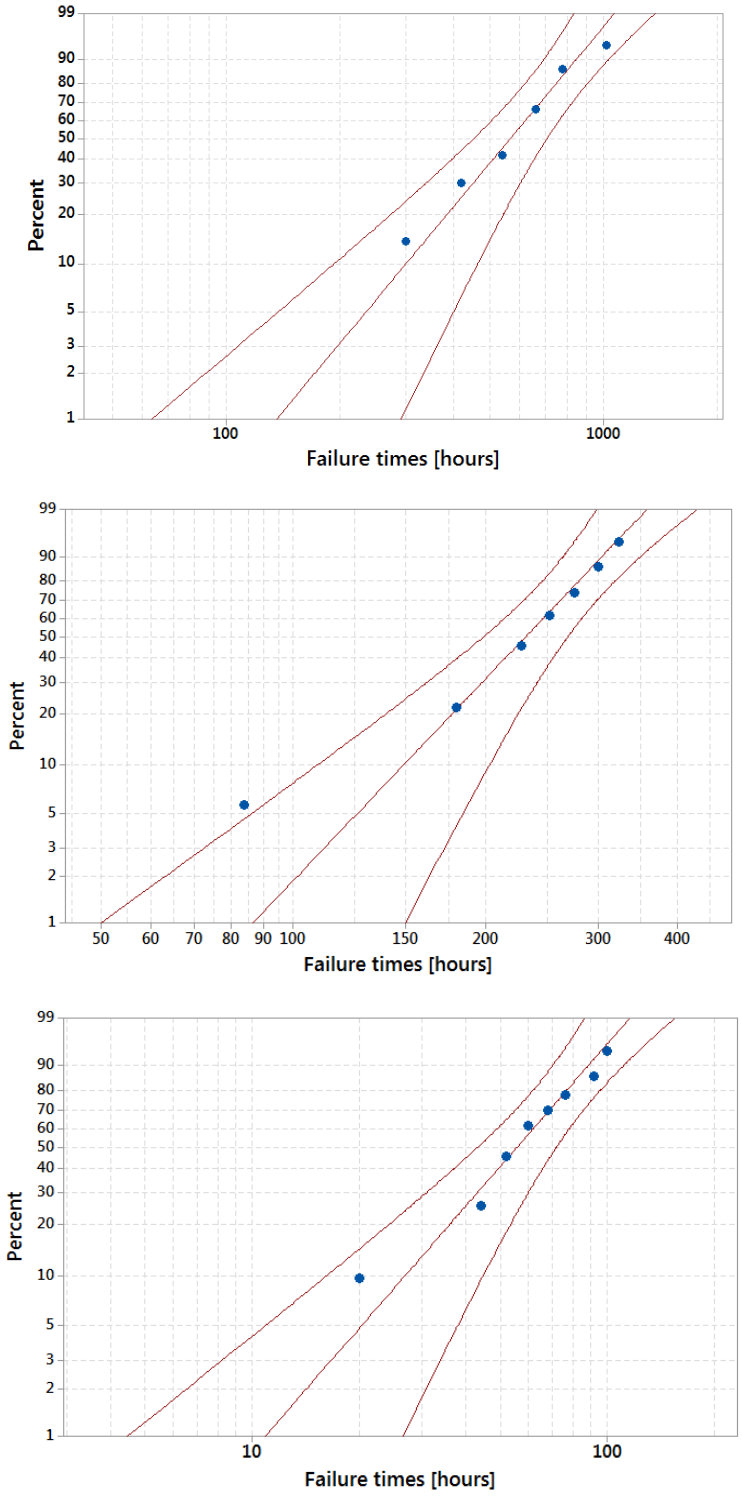

Figure 4.6 – Weibull probability plot of failure times for coils aged at 250 °C (top sub-plot), 270 °C (middle sub-plot) and 290 °C (bottom sub-plot).

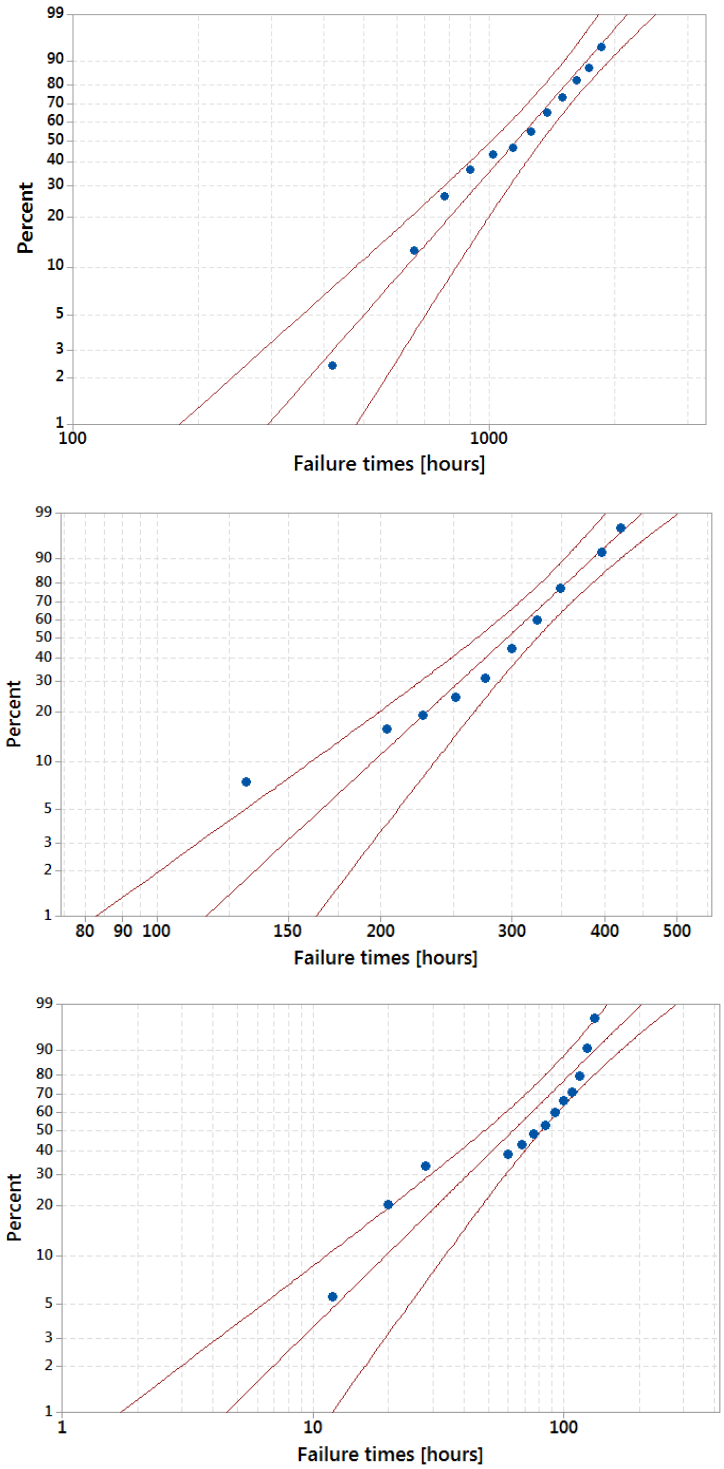

Figure 4.7 – Weibull probability plot of failure times for motorettes at 250 °C (top sub-plot), 270 °C (middle sub-plot) and 290 °C (bottom sub-plot).

4.2.4 Discussion

By analysing the data reported in Table 4.3 the first interesting result is the difference in the Weibull scale parameter among the three specimens. For a fixed aging temperature it can be noted that α, as well as other percentiles of failure times, are considerably lower for the coil specimens compared to the other two tested specimen layouts. Similar comparisons and results, to date, are not addressed in the literature concerning insulation systems for electrical machines. Thus, the adopted approach consisting in evaluating various specimens typologies, represents one of the novelties and strengths of this work.

The difference in failure times among specimens might be correlated with the so-called "size effect" [124]. That is, the failure rates can be proportional to the specimens' size. The Weibull distribution is a powerful and convenient tool for accounting for such effect. Let us suppose a generic specimen *SP1* whose dimension (i.e. volume, length, number of turns etc…) is ρ_{SP1} and its Weibull distribution has shape parameter β and scale parameter α_{SP1}. Then, a specimen *SP2*, with dimension ρ_{SP2} has a Weibull distribution with shape parameter β and scale parameter calculated as in (4.6) [124].

$$\alpha_{SP2} = \frac{\alpha_{SP1}}{\left(\frac{\rho_{SP2}}{\rho_{SP1}}\right)^{1/\beta}} \tag{4.6}$$

Note: when referring to thermal aging, the specimen's size does not generally influence the failure mode, as this is only related to the materials activation energy. This is why β does not depend on the specimen's size.

A sensitivity analysis has been carried out for evaluating if the α discrepancies among the specimens topologies are correlated with their size. In this case the selected geometrical dimension, ρ_{SP}, is the average length of one turn. Thus, the sensitivity analysis is performed by varying the number of touching turns (i.e. strands in this case), recalling that the coils and motorettes are randomly wound, and the results are reported in Figure 4.8, Figure 4.9 and Figure 4.10 for the temperatures of 250, 270 and 290 °C

respectively. From the gathered results, it can be observed that the scale factor, obtained experimentally, falls within the range provided by the size-effect formula, for both coils and motorettes. However, given the random nature of low voltage EMs windings, this range is quite wide. The Author believes that more precise predictions can be obtained when assessing the lifetime of form-wound EMs.

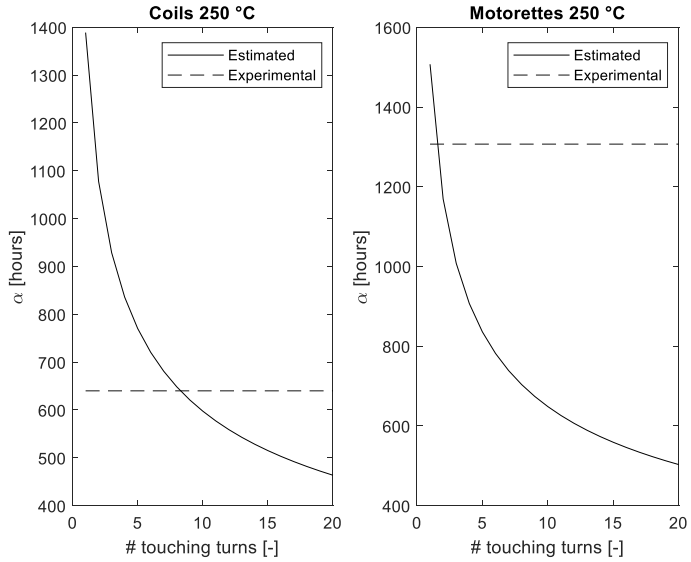

Figure 4.8 – Size effect sensitivity analysis for scale factor computation at 250 °C.

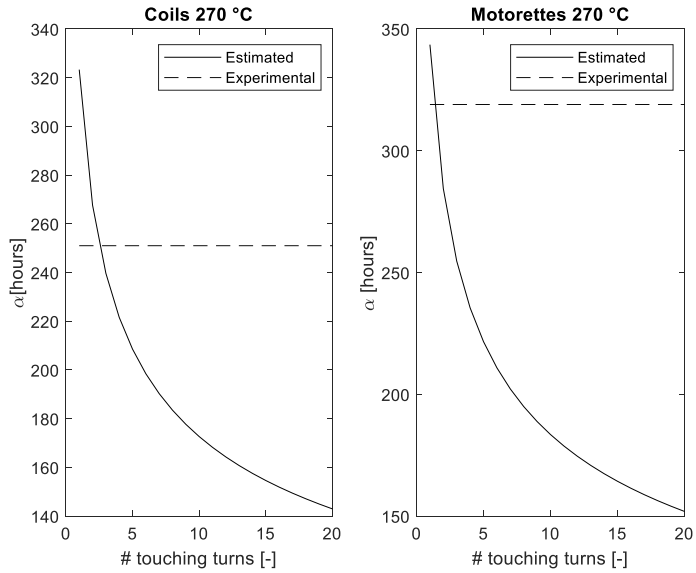

Figure 4.9 – Size effect sensitivity analysis for scale factor computation at 270 °C.

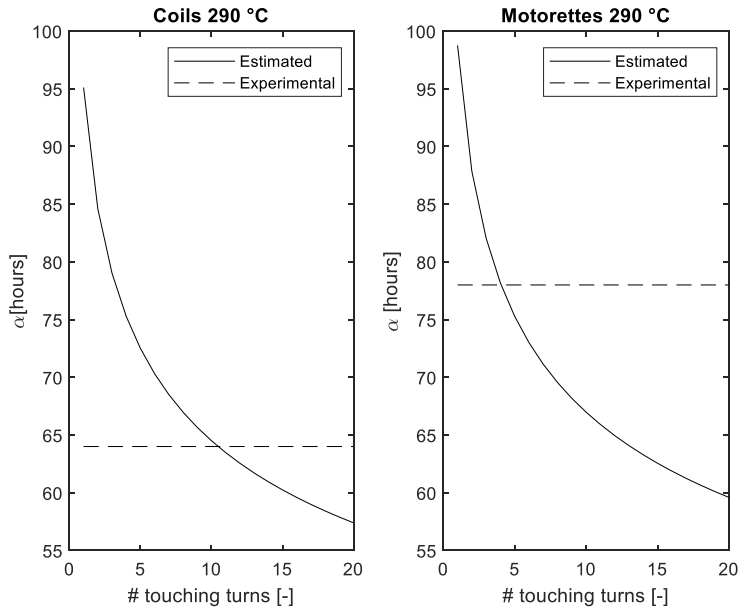

Figure 4.10 - Size effect sensitivity analysis for scale factor computation at 290 °C.

Nevertheless, the proposed sensitivity analysis/procedure might be a convenient tool for a preliminary "lifetime prediction" of a low voltage EM insulation, when only the magnet wire's Arrhenius curve is available (which in most cases is true, as the latter is generally provided by the wire's manufacturer).

Based on the presented results, it might be argued that for accelerated thermal aging tests, in low voltage EMs, the use of coils as specimen provides more conservative lifetime estimations. Another important consideration is that the manufacturing of coils is less time-consuming and more cost-effective than motorettes. Further, using the magnet wire's thermal class alone, for the thermal design of an EM is an improper procedure. In fact, the class provided by manufacturers is obtained by accelerated tests on twisted pairs, and thus it over-estimates the lifetime. All these information find their usefulness when planning accelerated thermal aging tests, particularly during the initial prototyping stage of a newly designed EM.

By observing the Weibull probability plot for the motorettes tested at 290 °C (see Figure 4.7) another important observation can be drawn: the data show two different failure modes (i.e. a variation in slope). This might indicate that a) the adopted

temperature (i.e. 290 °C) is too high for the tested organic insulation, triggering multiple chemical reactions and/or b) the specimens' have been mishandled during the diagnostic sessions. This second option is strengthened by the fact that the other two specimens (i.e. twisted pairs and coils) do not show such a behaviour.

4.2.5 Arrhenius Plot: Conventional Approach

The post-processed data attained from the accelerated thermal aging tests can be used for determining the Arrhenius plot (i.e. thermal endurance curve) of the tested specimens. For the reasons discussed in Section 4.2.4, the procedure will be reported only for the coils specimens. In fact, they 1) provide conservative results, 2) are cost effective and easy to manufacture and 3) the motorettes show two failure modes (for the highest tested temperature).

The approach conventionally reported by technical standards [125, 127], based on a first order regression, will be initially adopted for extrapolating the thermal endurance graph. Assuming a dominant chemical reaction involved in the thermal deterioration process, the lifetime of the insulation can be calculated as in (2.1), which is reported here again for the readers' convenience.

$$L = A \cdot \exp(B/\theta) \tag{2.1}$$

Equation (2.1) can be linearized by applying the logarithm to both sides as shown in (4.7).

$$\log_{10}(L) = \log_{10}(A) + \log_{10}(e) \cdot B/\theta \tag{4.7}$$

Equation (4.7) is the standard mathematical expression of a straight line in a $\log_{10}(L_{ins})$ vs. 1/θ graph scale. The method of least squares can be used for obtaining the slope and intercept of (4.7) on the basis of the experimentally-recorded failure times. In particular, the slope can be calculated as in (4.8), where N_{SP} is the number of tested specimens for each temperature, θ_i is the i_{th} temperature (in Celsius degrees) used during the aging tests and ttf_i is the corresponding median of failure times.

$$\log_{10}(e) \cdot B = \frac{N_{SP} \sum_{i=1}^{3} \left(\frac{1}{273 + \theta_i} \cdot \log_{10} ttf_i \right) - \sum_{i=1}^{3} \frac{1}{273 + \theta_i} \cdot \sum_{i=1}^{3} \log_{10} ttf_i}{N_{SP} \sum_{i=1}^{3} \left(\frac{1}{273 + \theta_i} \right)^2 - \left(\sum_{i=1}^{3} \frac{1}{273 + \theta_i} \right)^2} \tag{4.8}$$

The intercept can be calculated as shown in (4.9).

$$\log_{10}(A) = \frac{\sum_{i=1}^{3} \log_{10} ttf_i - \log_{10}(e) \cdot B \sum_{i=1}^{3} \frac{1}{273 + \theta_i}}{N_{SP}} \tag{4.9}$$

The resulting Arrhenius plot of the coils, relative to the median of failure times is shown in Figure 4.11, where the experimentally-recorded failure times are also reported.

Through the Arrhenius plot it is then possible to predict the coils' lifetime for temperatures others than 250, 270 and 290 °C. Of course, this methodology allows the user to extract information about the predicted median of failure times, without however providing any information regarding other percentiles. However, it is also important to note that this methodology is the most widely-accepted process for these kind of analyses and is in fact adopted by the major technical standards, such as [125, 127, 130].

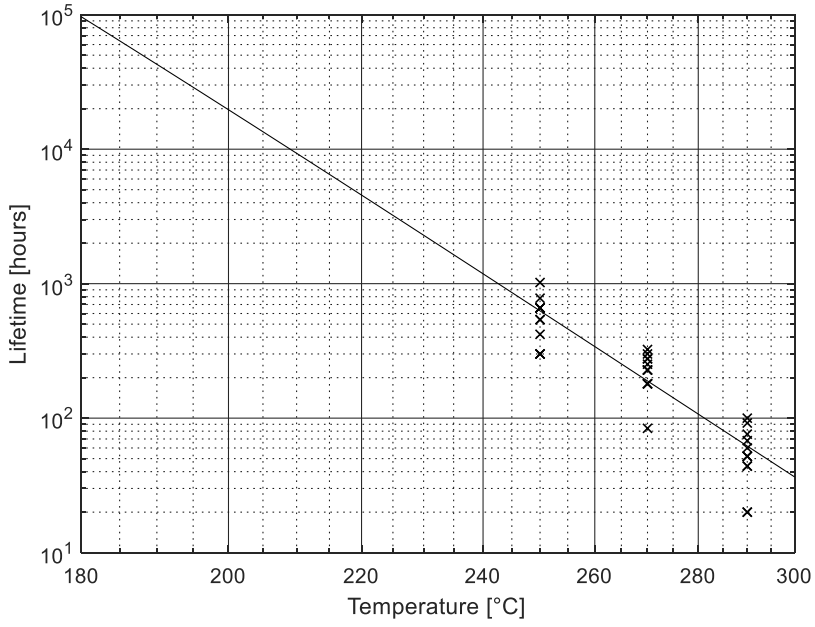

Figure 4.11 – Arrhenius plot (thermal endurance curve) for the coils specimens.

4.2.6 Arrhenius Plot: Weibull Distribution Evaluation at the Design Temperature

A more elegant and precise method for assessing the failure probability of an insulation exposed to thermal stress is presented in this sub-section. Statistical textbooks define this method as "Graphical Data Analysis" [124] since, in the past, the computation was mainly performed graphically. With the availability of modern computational software, this analysis can be carried out in a more accurate fashion.

As a first step, it is necessary to plot the experimentally-recorded failure times (relative to each aging temperature) on a single probability graph as shown in Figure 4.12. The second step consists in fitting three (i.e. one for each temperature) straight distribution lines. The slope of the three lines should be identical, and equal to the one that better fits the experimental data (i.e. the vertical deviations between the regression line and the plotted points should be as small as possible [124]). As mentioned, this procedure can be carried out either graphically or through the minimum least square method, e.g. (4.8) and (4.9). The second option is favoured in this work, given the availability of a powerful statistical software (i.e. Minitab® 17), and the result is reported in Figure 4.13. Since the three probability lines are parallel with each other, the corresponding Weibull probability distributions will have a common shape factor (i.e. β) which in this case is equal to 2.987. The scale factors (i.e. 63.2% percentile of failure times) are different among the three temperatures, and they are reported in Table 4.4 together with the 10% percentile and the median (i.e. 50% percentile).

Table 4.4 – Weibull percentiles of failure time for a fixed shape factor β (coils specimens).

[β=2.987]	**Temperature**		
Failure times percentiles	*290 °C*	*270 °C*	*250 °C*
10 %	33.7 h	100 h	328 h
50 % (median)	63.3 h	189 h	616 h
63.2 % (α)	71.6 h	214 h	696 h

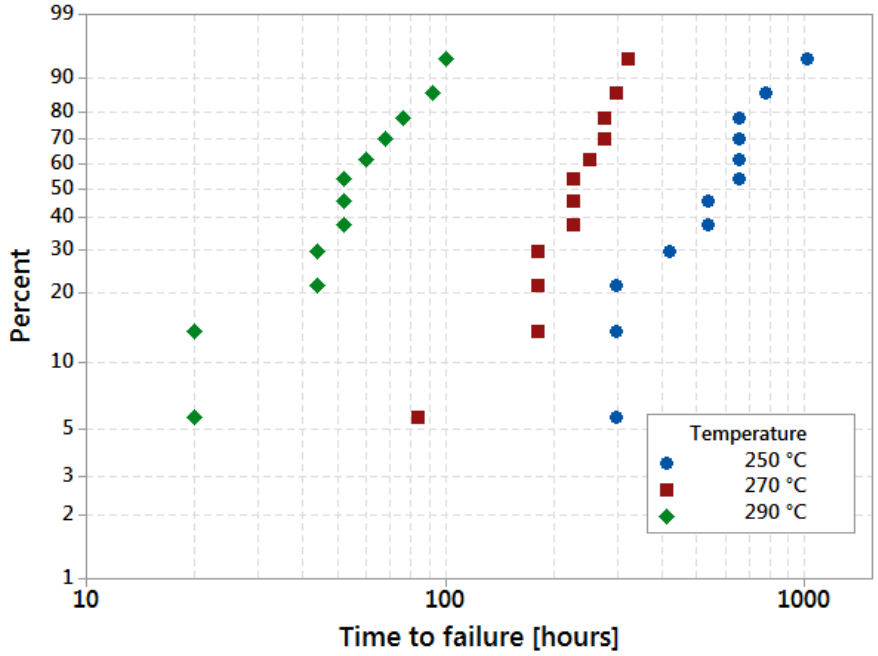

Figure 4.12 – Weibull plot of the accelerated thermal aging data (coils specimens).

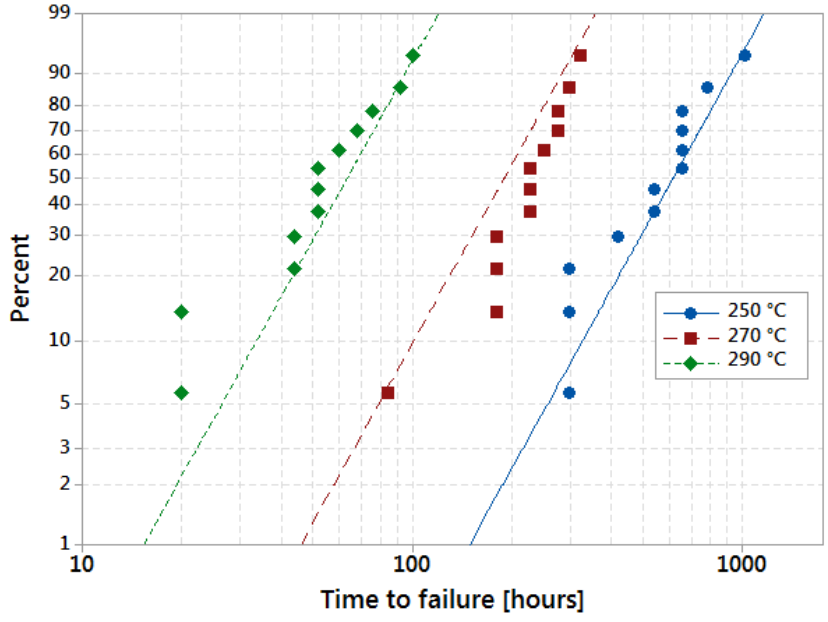

Figure 4.13 – Parallel Weibull fit of the accelerated thermal aging data (coils specimens).

At this point, three different thermal endurance curves (one for each percentile) can be plotted on the same Arrhenius plot, adopting the procedure reported in Section 4.2.5, as shown in Figure 4.14. As can be observed, the three endurance curves have the same slope, which means that the activation energy of the main chemical reaction

[i.e. B of (2.1)] is equivalent among them. This makes complete sense from a chemistry / physics point of view, as the insulation's activation energy is an intrinsic parameter of the material. Nonetheless, in an investigation presented in [131] the provided endurance curves, at various percentiles, show different slopes amongst them. However, the Authors did not expand the discussion on this particular point. An explanation to such discrepancy could be the adoption of too high temperatures during the thermal aging tests. This, in turn, can trigger secondary reactions involved in the insulation's degradation process, leading to the aging model (which considers only a single dominant chemical reaction) being unsuitable for the analysis.

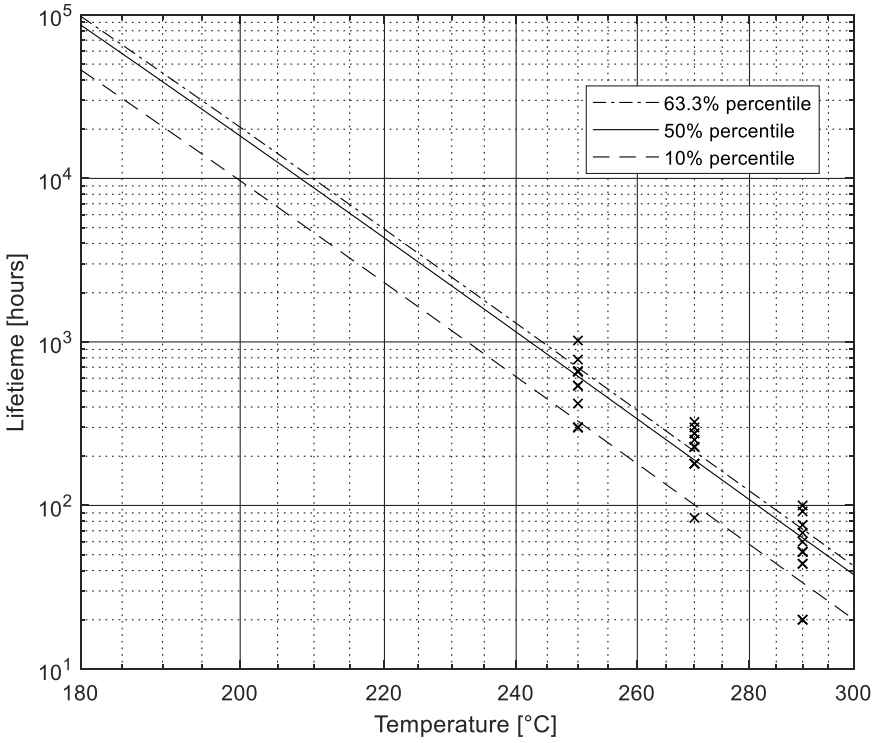

Figure 4.14 –Arrhenius plot for coils specimens reporting three percentiles of failure time.

The availability of the Arrhenius plot with various percentiles of failure time, is extremely important at the design stage of an EM. Indeed, if a specific reliability level is required for a given EM, then, assuming a single-stress model, a designer can fix the maximum hot-spot temperature which guarantees such level. Furthermore, the thermal endurance curve relative to α (dot-dash line in Figure 4.14) allows to extrapolate the

Weibull CDF (i.e. unreliability function) for any desired (design) temperature, as the scale factor (i.e. α) is the only necessary information, being β fixed. An example of application is reported in Section 4.3.

4.3 Case-Study: Aerospace Environmental Control System

A PMSM used for powering/driving an environmental control system (ECS) compressor in a more-electric business jet is used as a case-study. One of the main concepts of the MEA initiative, is the adoption of the so-called "bleed-less" engine architecture. Thus, the ECS, which in traditional aircraft is driven by high-pressure air extracted from the engines (i.e. pneumatic power), is, in modern EMA platforms, operated electrically through the use of VSDs. The compressor units, used for pressurisation purposes, are active for most of the flight duration. Thus, the EMs used for driving such systems can be (conservatively) considered to be operated under (full-load) continuous duty.

The main design parameters of the designed PMSM are listed in Table 4.5. The EM has been sized analytically and via electromagnetic FE using the commercial software Ansys® Maxwell 2D. The full-load flux density and magnetic field lines of the PMSM are depicted in Figure 4.15. Further details regarding the electromagnetic design are purposely omitted here, as this goes beyond the scope of the Thesis, but they are detailed in [132].

Table 4.5 – Main design parameters of the case-study, aerospace PMSM.

Parameter	Quantity
DC link voltage	270 V
Rated power	30 kW
Maximum speed	25000 rpm
Cooling method	Forced liquid (water jacket)
Available flow rate	6 L/min
Pole pairs, p	1
Slot number, Q	12
Turns per coil	5
Phase current	111 A (rms)
Stator outer diameter	150 mm
Axial length	85 mm

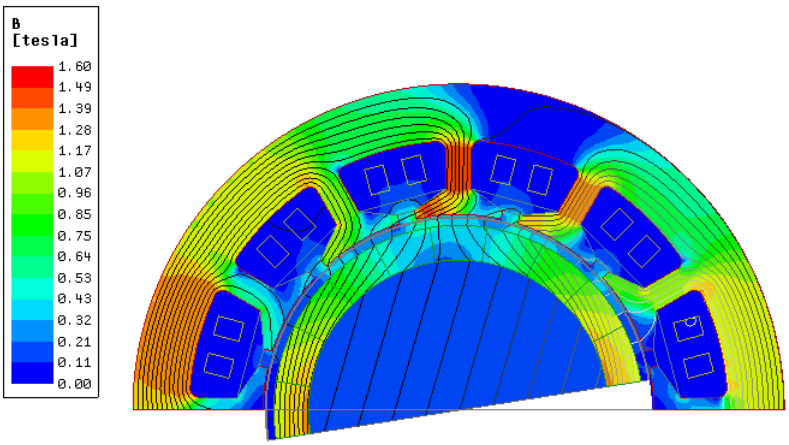

Figure 4.15 –30 kW PMSM for ECS compressor: magnetic flux density map and field lines at rated operating condition.

The PMSM thermal analysis has been carried out using the LPTN approach (cfr. Section 3). In particular, the LPTN reported in Figure 3.11, purposely modified according to the EM dimensions, has been adopted. The steady-state winding temperature, obtained from the thermal simulation, is equal to 150 °C, and the hot-spot is localised in the end-winding region. These findings are confirmed via a simulation through the commercial software Motorcad® (which also adopts an LPTN approach for the thermal modelling). The reliability assessment of the PMSM will be carried out in the following sub-section, by assuming the turn to turn insulation breakdown, caused by thermal aging, as the dominant failure mode. It is worth outlining that the DC link voltage level (i.e. 270 V) justifies the consideration that this EM is PD-free. This important point will be clearer after going through Chapter 6.

In order to employ the data obtained from the accelerated thermal aging tests at constant temperature, it is assumed that the ECS EM employs the same magnet wire used for the experimental campaign. Nonetheless, the presented study has general validity and can be applied to any magnet wire, provided that experimental thermal lifetime data are available.

The thermal endurance curve with multiple percentiles, reported in Figure 4.14, can be extended for temperatures as low as the EM design temperature, as shown in Figure 4.16. By intercepting the 63.2% percentile line with the 150 °C abscissa (i.e. EM hot-spot temperature), it is possible to obtain the scale factor [i.e. $\alpha(150°C)$] for the

design temperature of 150 °C, which is equal to $1.3499 \cdot 10^6$ hours. At this point, by recalling that β is equal to 2.987, the Weibull CDF plot can be obtained using (4.2) and it is reported in Figure 4.17.

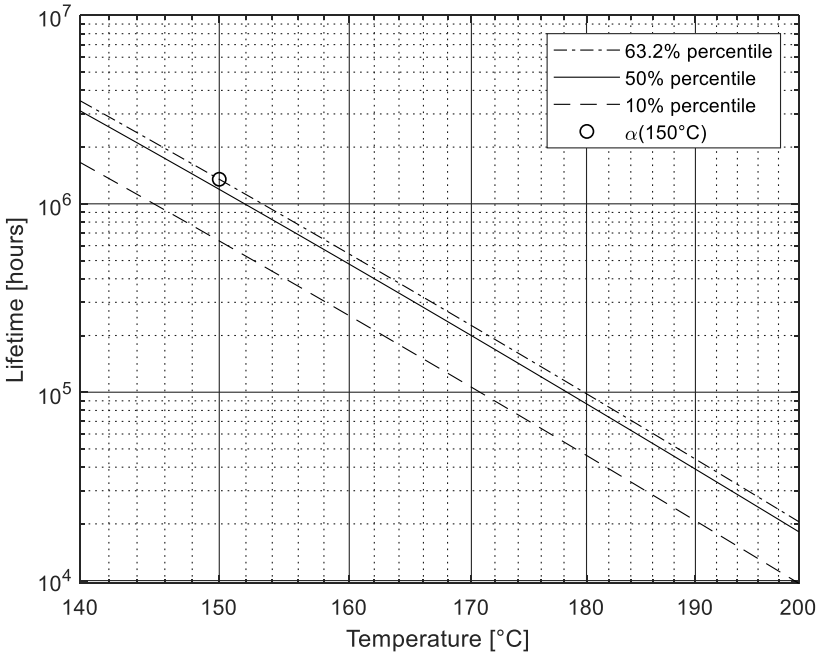

Figure 4.16 –Thermal endurance curve and percentiles for design temperature.

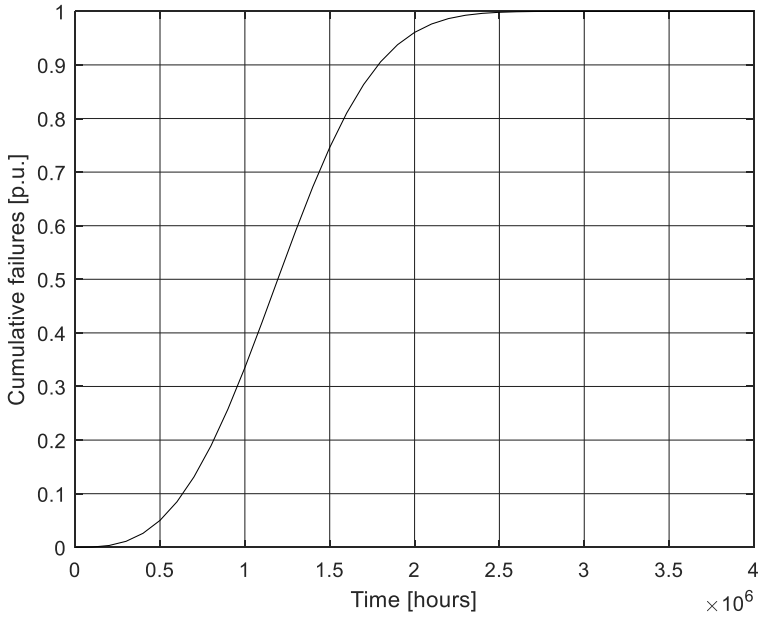

Figure 4.17 –Weibull CDF (i.e. unreliability) of the case-study PMSM insulation.

Assuming that the EM must operate for 10,000 flight-hours before being replaced/serviced, its probability of failure (at the end of its useful life) can be calculated as in (4.10) (i.e. Weibull CDF), and it is equal to $4.33 \cdot 10^{-7}$.

$$F(10000) = 1 - \exp\left[-\left(\frac{10000}{1.3499 \cdot 10^6}\right)^{2.987}\right] \tag{4.10}$$

The failure rate after 10,000 flight hours, calculated as the ratio between the Weibull PDF and the Weibull reliability function (i.e. 1-CDF), is equal to $1.3 \cdot 10^{-10}$ failures per hour. According to the EASA (European Union Aviation Safety Agency) Standard for Large Aircraft Certification (CS-25) [133], the obtained probability of failure corresponds to an "extremely improbable failure condition". If a lower failure probability is required, various strategies can be implemented. These include:

1. Reducing the thermal loading of the PMSM by adopting larger conductors (and thus increasing the EM size) – or alternatively enhancing the cooling effectiveness by e.g. adopting a higher flow-rate for the housing water jacket coolant;
2. Scheduling a more frequent EM replacement;
3. Applying redundancy measures.

The strategy #1 is mainly an EM design exercise. It can be easily carried out by experienced EM designers by using common scaling laws or sensitivity FE analyses. For this purpose, the thermal analysis via LPTNs presented in Section 3 is extremely useful, as it allows to apprise the thermal performances of various designs without requiring excessive computational effort. For the implementation of the strategy #2, the Weibull CDF helps to easily evaluate the probability of failure at any operating time (i.e. for any number of flight-hours in this particular case-study). The strategy #3 can be fulfilled by adopting a) more than one EM for driving the same load [29] and/or b) a fault-tolerant drive topology [103]. In fact, for safety-critical systems, more than one independent means might be required for satisfying the same purpose (i.e. driving/powering the same load). In all of this, it must be pointed out that an interturn failure does not cause the instantaneous EM outage. Actually, it was demonstrated by

this Author that if an electric drive is properly designed, it can safely operate (for a limited amount of time) under severe fault conditions such as phase to ground short-circuits [103].

In the presented case-study, the "size-effect" discussed in Section 4.2.4 has not been taken into account. The adopted thermal endurance curve is the one relative to the coils specimens. For a more precise analysis, the Weibull scale factor should be re-adapted according to the PMSM winding layout/size. Nonetheless, it must be also underlined that in the presented study, it was (conservatively) assumed that the whole PMSM's winding operates at a uniform temperature of 150 °C. As shown in Chapter 3, this is not the case, as the hot-spot is generally localised in a small portion of the winding (usually the end-winding volume, particularly for indirect liquid cooled EMs). Another "pessimistic" assumption has been made by considering the EM operating at full-load for the whole flight duration. This is not completely true, since ECS compressors do not always operate at full load (e.g. during the climbing phase, the cabin pressurisation requirements are less demanding than in cruise condition). Because of these conservative considerations, in the Author's opinion, the presented reliability assessment procedure represents a fair compromise between accuracy and computational complexity. In other words, the listed assumptions, which considerably simplify the overall reliability assessment, are carefully chosen for providing a conservative life estimation rather than an optimistic one. Thanks to the proposed methodology, a quantitative estimation on the winding's probability of failure is obtained. This surely represents a step ahead of traditional reliability assessment methodologies, based on outdated handbooks which refer to technologies and manufacturing techniques belonging to the last century.

4.4 Concluding Remarks

In this Chapter it has been demonstrated how temperature can significantly affect the lifetime of insulation systems (and the EM in which they are installed). This critical aspect has been "well known" in the EM designers' community for almost one

century. However, there has never been a real integration of insulation thermal degradation models in the design procedure of an EM. This Chapter aimed in providing such kind of "integration tool" by adopting both experimental results as well as theoretical formulas/concepts. Some basic statistical post-processing analysis was carried out, as it allows to better exploit the collected experimental data. This part can be surely further expanded and made even more rigorous by statisticians / mathematicians. For the purpose of this work, it represents a reasonable compromise between accuracy and computational simplicity. The considered aerospace case-study was purposely introduced for providing the readers with an application example for the proposed methodologies.

According to Figure 1.4, where the "PhD story" is summarised, this Chapter represents a technical focal point. The thermal aging at constant temperature has been, in the past, extensively addressed by literature on dielectric science. However, what presented here aims at being a fairly comprehensive analysis on this topic, but from a machine designer side. Thus, considerations on dielectrics thermal aging and physics of failure are linked with statistical computations, with the aim of predicting the time to failure of thermally aged electrical motors.

This Chapter resulted in the publication of 2 journal papers [128, 132] and 2 conference papers [134, 135], and it is still source of ongoing research activity.

Chapter 5 Insulation Thermal Aging in Variable Duty Electrical Machines

This Chapter focuses on the insulation lifetime modelling for short- and variable-duty EMs. In this case, the winding (insulation) temperature is subject to "heavy" thermal cycling (i.e. non-constant temperature) as, in most cases, designers tend to take advantage of the short duty cycle and improve the machine design (e.g. power density) by "pushing" the thermal limit boundaries. Consequently, the standard Arrhenius-Dakin law, suitable for constant temperature operations, needs to be properly modified. A variant of this model is therefore proposed in this Chapter, and its effectiveness is experimentally investigated. The Chapter concludes with 3 different case-studies. The first two, namely an aerospace and an automotive machine, are used for showing the implementation of the proposed model. The third case-study, which is a motor for aerospace propulsion purposes, is used for proposing an innovative, physics of failure-oriented design methodology for EMs.

5.1 Problem Statement

A large number of EMs operate under short time or variable duties, i.e. the motor does not run at a continuous load for sufficient time to enable thermal equilibrium (i.e. steady-state temperature) [84]. Examples of short time duty EMs are aerospace EMAs for secondary flight control (e.g. high lift devices), where the mission profile usually requires a high torque level for a relatively short amount of time.

Even if an automotive traction motor can reach the thermal equilibrium at some point in time during operations, however, in practice, can experience large thermal

transients. A standard automotive drive cycle will comprise various stages that require the delivery of high torque in a short time-span (e.g. during start/stop or overtaking), causing wide variations in the winding temperature. In general, the winding temperature of on-road vehicles EMs can range from tens of Celsius degrees below zero (i.e. during winter time in some northern hemisphere regions) up-to ≈180 – 200 °C (hot-spot) in peak operating conditions.

At this point, the question is: how can the (thermal) insulation lifetime of such variable duty EMs be predicted? Contrarily to insulation thermal aging at constant temperatures, which has extensively been addressed in past literature (and in Chapter 3), thermal cycling, particularly for low voltage EMs, is a very sparsely investigated topic. This is partially in contrast with the ever-increasing push for electrification, where high power, low mass EMs are demanded, and (most of) these machines are not continuously running (as in the case of e.g. large generators in power plants). In fact, most of the times, the EM designer adopts an "overpessimistic" approach when thermally sizing a variable-duty machine, by accounting for large safety-margins, and thus over-engineering the insulation. This procedure will most likely extend the insulation lifetime, but, at the same time, defeats the whole concept of higher power-dense EMs.

Before the widespread of PWM-operated variable speed drives, the insulation system design for mains-fed, low voltage EM was mainly based on mechanical considerations. Namely, insulating materials were chosen with the purpose of withstanding in-service mechanical forces as well as resisting abrasion during the manufacturing process [40]. Electrical and thermal constraints were satisfied by a) selecting an appropriate thickness for the interphase and phase to ground insulation systems, for avoiding PDs inception and b) operating the winding at temperatures well below the thermal limit of insulating materials, by relying on safety factors during the design stage. With the progressive trend towards high performance VSDs, these conventional design methodologies need to be updated for satisfying ever-increasing power density requirements. The interturn insulation sub-system, which for mains-fed EMs was not a source of concern, is nowadays one of the most reliability-critical, and

performance-limiting subcomponents in VSDs. Indeed, the winding insulation choice for a low voltage, variable-speed EM needs to be coordinated with the features of the power electronics converter, as will be discussed in Chapter 6. On the thermal side, advancements in dielectrics and material sciences have strongly contributed to the commercial availability of winding's organic enamels able to operate at temperatures higher than 250 °C. However, it is the Author belief that having tools and methodologies for their reliability assessment and life prediction can actually change the game in terms of how EMs are designed and operated.

The following Sections will thus describe methodologies for the insulation lifetime prediction/assessment of variable duty EMs, aiming at minimizing the reliance on over-engineering approaches. The reported considerations can be integrated at an early stage in the EM design procedure, with the aim of guaranteeing optimal electromagnetic performance while satisfying reliability requirements.

5.2 Proposed Lifetime Prediction Model

The Arrhenius-Dakin model, in its standard form as described by (2.1) does not allow to predict the insulation lifetime under variable temperature operations. Therefore, it has been purposely modified, and combined to the cumulative damage law (i.e. Miner's rule) [53], introduced in Chapter 2 and repeated here for the readers' convenience.

$$C_d = \sum_{i=1}^{k} \frac{n_i}{N_i} \tag{2.4}$$

In order to re-adapt the insulation's thermal life data, experimentally derived in Chapter 4, again it is assumed that the interturn insulation system consists of the sole wire's organic enamel. Accordingly, because of this assumption (i.e., non-impregnated winding) the chemical interaction / compatibility between organic enamel and impregnating material is not modelled. This does not compromise by any means the validity of the discussion that follows. Indeed, what presented in the following

paragraphs can be mirrored for impregnated windings, provided that data from accelerated thermal aging tests on impregnated specimens are firstly acquired.

To obtain the desired lifetime model, a generic temperature profile (i.e. temperature vs. time) as shown in Figure 5.1 is assumed. The first step consists in dividing the entire time pattern into infinitesimal intervals, ranging from a generic time instant t to a subsequent time $t+dt$, so that within every dt, the temperature can be taken as constant and equal to the corresponding instant-value of transient temperature, $\theta_i(t)$. Hence, the fraction of life "lost" (i.e. consumed) by the insulation, during a given dt within Δt_i, can be written as shown in (5.1), where $L[\theta_i(t)]$ is the insulation life at constant temperature $\theta_i(t)$ [cfr. (2.1) and (2.2)].

$$dLF = \frac{dt}{L[\theta_i(t)]} \tag{5.1}$$

Hereafter, the quantity dLF will refer to an infinitesimal "loss of life fraction". Therefore, the loss of life fraction at each cycle, LF_{cycle}, is given by (5.2).

$$LF_{cycle} = \int_0^{\Delta t_{cycle}} dLF = \int_0^{\Delta t_{cycle}} \frac{dt}{L[\theta_i(t)]} \tag{5.2}$$

For the sake of clarity, a graphical explanation regarding the computation of the loss of life fraction is shown in Figure 5.2.

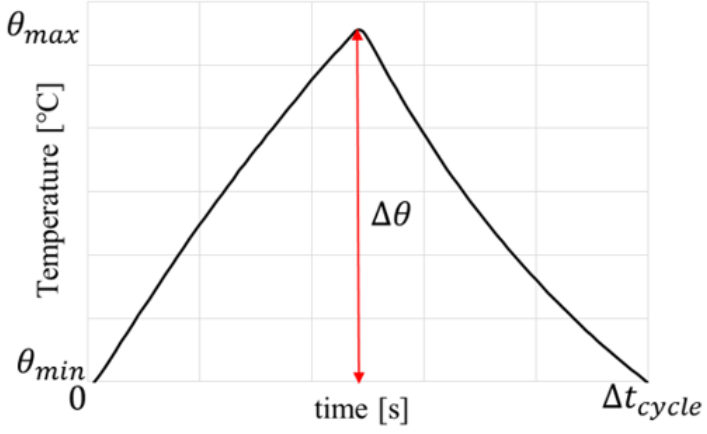

Figure 5.1 – Generic temperature profile.

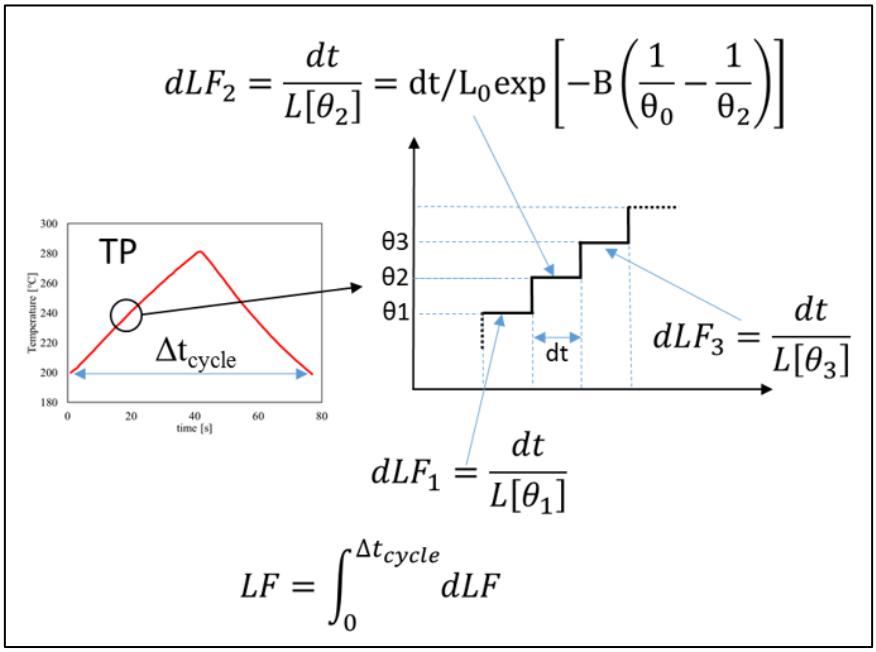

Figure 5.2 – Loss of life fraction computation.

At this point, the only two inputs, necessary for the loss of life computation, are the temperature profile, which is available from the considered application, and the parameters of the Arrhenius model defined by (2.1) and (2.2). The Arrhenius equation, in the form proposed by Montanari and Simoni [37], (2.2) is preferred at this stage. Equation (2.2) is repeated here for convenience.

$$L_{ins} = L_0 \cdot \exp\left[-B\left(\frac{1}{\theta_0} - \frac{1}{\theta}\right)\right] \tag{2.2}$$

It is important to recall that L_0 is the lifetime (for a given percentile) corresponding to the (absolute) temperature θ_0, while B is the slope of the thermal endurance curve shown in Figure 4.14, related to the (main reaction's) activation energy. It is then clear why (2.2) is preferred over the general Arrhenius equation (2.1). In fact, the parameters L_0, θ_0 and B can be easily obtained from the thermal endurance curve. For this purpose, the Arrhenius plot, relative to the coils specimens shown in Figure 4.14 is adopted. The 63.2% percentile failure times is considered (i.e. α of the Weibull distribution). Nonetheless, the proposed approach for the Arrhenius curve extrapolation allows to use

any percentiles of the Weibull distribution (the B parameter is equal for every percentile).

The lifetime value $L_{\theta 0\text{-}\alpha}$ of 20,000 hours is selected for the computation. This value corresponds to a temperature $\theta_{0\text{-}\alpha}$=(273+200) K. After selecting a second generic temperature $\theta_{k\text{-}\alpha}$, whose corresponding lifetime on the Arrhenius curve is $L_{\theta k\text{-}\alpha}$, the B parameter can be computed as in (5.3).

$$B = \frac{\ln\left(L_{\theta_{k-\alpha}}/L_{\theta_{0-\alpha}}\right)}{\frac{1}{\theta_{k-\alpha}} - \frac{1}{\theta_{0-\alpha}}} \tag{5.3}$$

It is worth remarking that B can be also easily calculated by rearranging (4.8) as shown in (5.4).

$$B = \frac{N_{SP}\sum_{i=1}^{3}\left(\frac{1}{273+\theta_i}\cdot\log_{10} ttf_i\right) - \sum_{i=1}^{3}\frac{1}{273+\theta_i}\cdot\sum_{i=1}^{3}\log_{10} ttf_i}{N_{SP}\sum_{i=1}^{3}\left(\frac{1}{273+\theta_i}\right)^2 - \left(\sum_{i=1}^{3}\frac{1}{273+\theta_i}\right)^2} / \log_{10}(e) \tag{5.4}$$

The loss of life fraction in a generic cycle LF_{cycle} can be now computed by numerically integrating the right hand side of (5.5).

$$LF_{cycle} = \int_0^{\Delta t_{cycle}} \frac{dt}{L_0 \cdot \exp\left[-B\left(\frac{1}{\theta_0} - \frac{1}{\theta_i(t)}\right)\right]} \tag{5.5}$$

The theoretical number of cycles to failure, relative to the ψth percentile of failure times, $K_{\psi}^{'}$ can be calculated as in (5.6), according to the Miner's rule [i.e. (2.4)], which states that the end of life is reached when the cumulative damage equals one.

$$K'_{\psi} = 1/LF_{cycle} \tag{5.6}$$

Alternatively, the total life, $L_{tot\text{-}\psi}$, of the cyclically stressed insulation can be calculated in unit measure of time as in (5.7).

$$L_{tot-\psi} = K'_{\psi} \cdot \Delta t_{cycle} \tag{5.7}$$

To summarize the proposed insulation lifetime prediction methodology, a visually descriptive tool is reported in Figure 5.3. This methodology is considered to be one of the main outcomes of this Thesis.

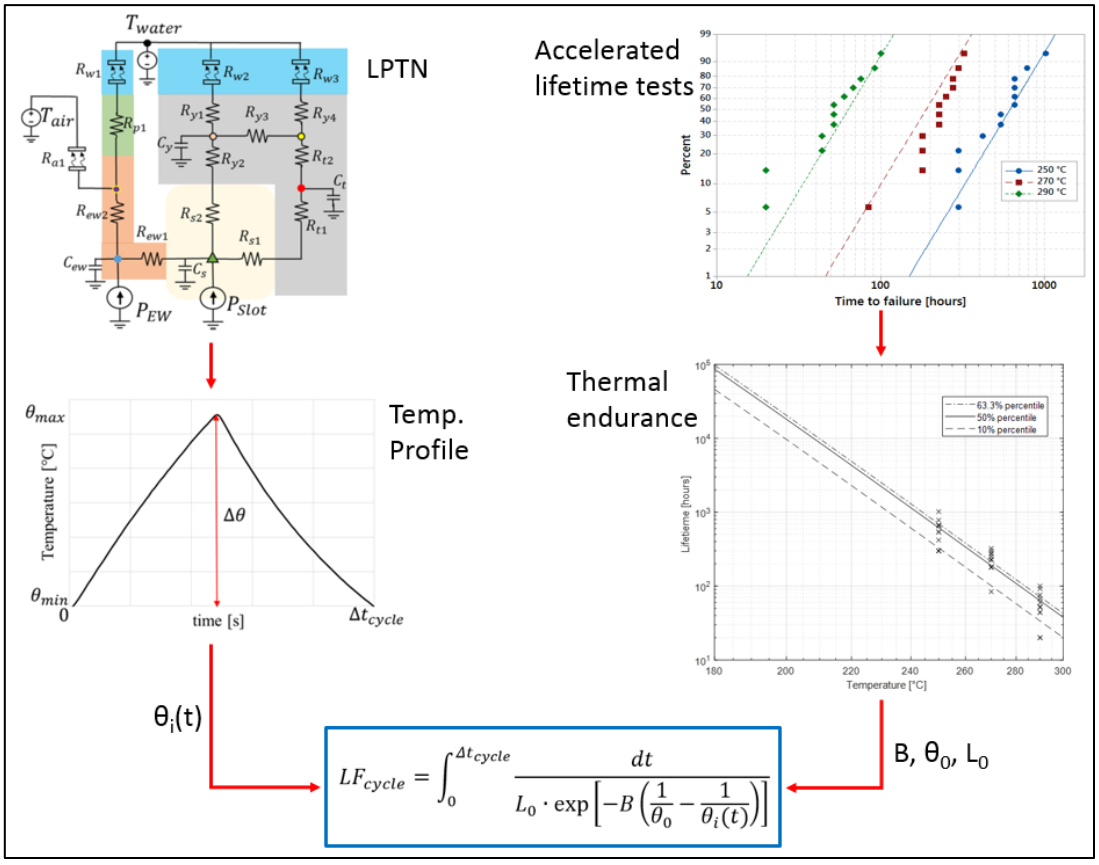

Figure 5.3 – A scheme of the proposed methodology for the thermal insulation lifetime estimation under dynamic temperatures.

For its correct application, two main "ingredients" are required, namely a representative temperature profile, and the parameters of the Arrhenius model. The temperature profile can be obtained through a transient thermal simulation of the EM under analysis via LPTN, as described in Chapter 3. The parameters for the Arrhenius model are experimentally derived by accelerated lifetime tests on custom made specimens, as reported in Chapter 4. How the proposed method is applied for the reliability assessment of an electric motor is explained in the final part of this Chapter. The next section aims instead in experimentally validating the proposed Arrhenius-Miner model

5.3 Experimental Validation

5.3.1 Test Setup Description

Two sets of twelve coils each, identical to those shown in Figure 4.1, are manufactured using the same magnet wire thermally-evaluated in Chapter 4 (cfr. Table 4.1). Again, the sample size (i.e. number of specimens) is selected according to guidelines from both IEEE and IEC standards. The choice of using coils instead of motorettes arises by the fact that the former have a considerably lower thermal inertia than the latter do. This implies that: a) thermal cycles with wider temperature gradients can be adopted throughout the validation procedure, and b) for a fixed time-span, the coils can be exposed to a larger number of thermal cycles with respect to motorettes, as they can be cooled down more rapidly.

The specimens are hung to a PTFE rod and inserted inside a fume hood with variable air flow-rate, as shown in Figure 5.4. By regulating the flow-rate, it is possible to adjust the convection heat exchange between coils and ambient. The schematic of the experimental setup is depicted in Figure 5.5. The specimens are heated by exploiting the Joule effect, hence they are fed using an Elektro Automatik® DC power supply. The coils' temperatures are measured by means of K-type thermocouples uniformly distributed within the specimens. The acquired temperatures are elaborated by a digital signal processor (DSP) (i.e., Raspberry PI®), which also controls the DC power supply via the analogue interface. For aging purpose, the applied temperature profile is shaped by selecting the suitable DC current value and the proper air flow-rate of the fume hood. A PID controller, implemented in an Arduino® board is used for modulating the applied current, and thus following the desired temperature profile.

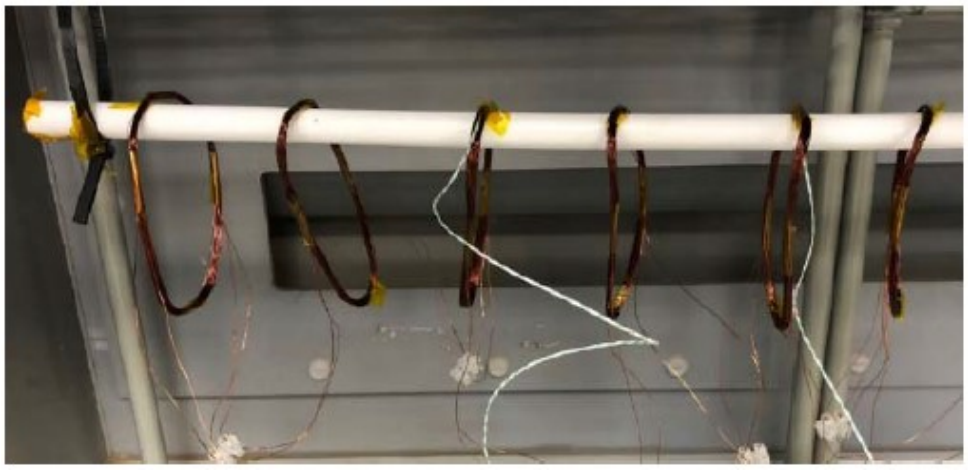

Figure 5.4 – Coils hung to a PTFE rod inside the fume hood.

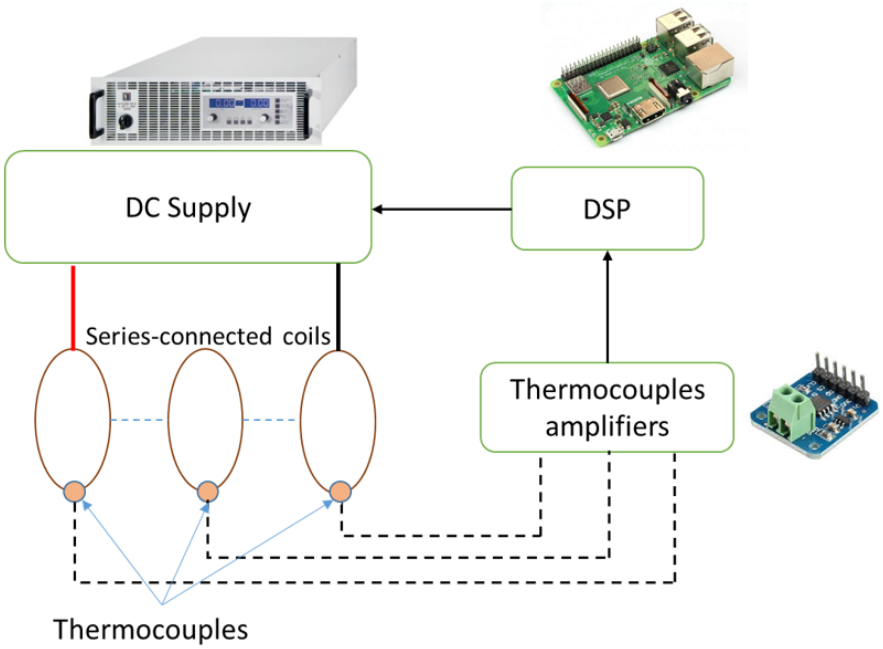

Figure 5.5 – Diagram of the experimental test setup.

5.3.2 Aging temperature profiles definition and end of life

Before starting the thermal cycling tests, the aging temperature profiles are defined, according to the following constraints: 1) the duty cycles should have the same order of magnitude of short-duty EMs, and 2) the temperature(s) should be higher than the magnet wire thermal class in order to enhance the thermal stress and reduce the

duration of the test campaign. Two different temperature profiles are selected according to these constraints, these are named TP#1 and TP#2 and they are reported in Figure 5.6 and Figure 5.7 respectively. These temperature profiles have a time duration which is compatible with typical EMs for aerospace actuators (which is one of analysed case-studies).

The two sets of coils are aged with the temperature profiles TP#1 and TP#2 according to the flow-diagram reported in Figure 5.8. For consistency's sake, the end of life criterion for the aged specimens is maintained unchanged with respect to the analysis presented in Chapter 4 (i.e. dielectric strength assessed through the AC hipot test). Thus, when a specimen fails the AC hipot test, it is removed from the experiment and its time to failure is recorded.

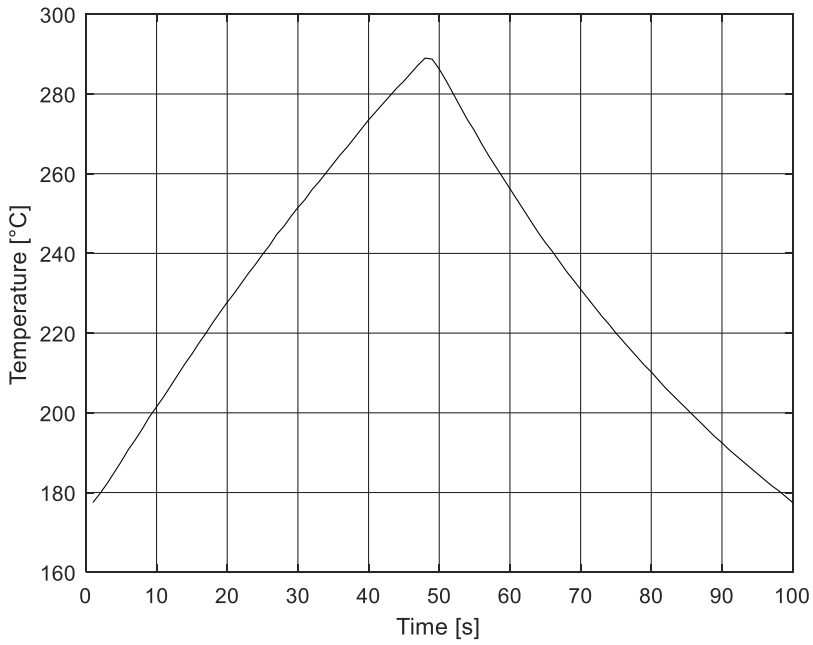

Figure 5.6 – Experimental temperature profile TP#1.

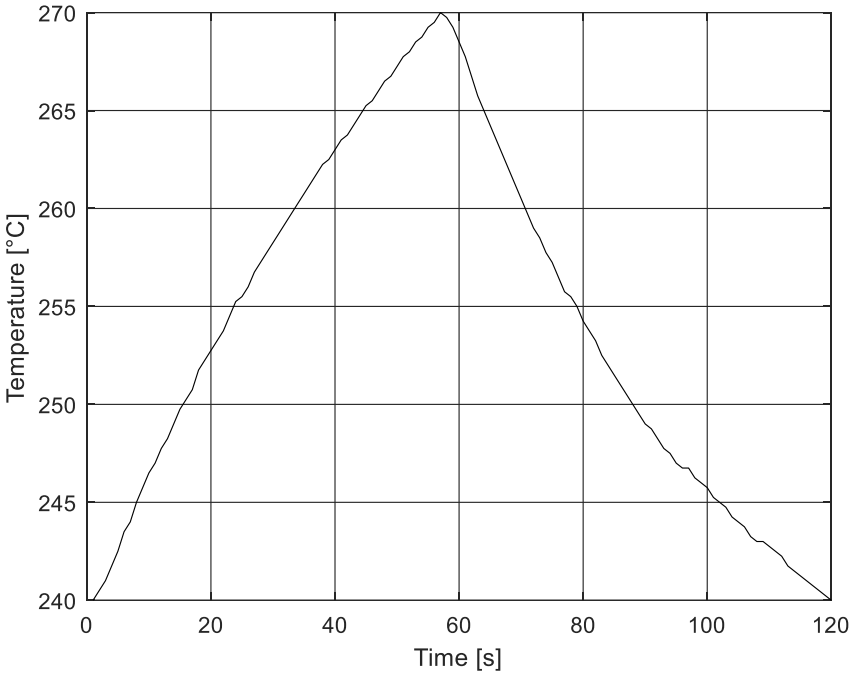

Figure 5.7 – Experimental temperature profile TP#2.

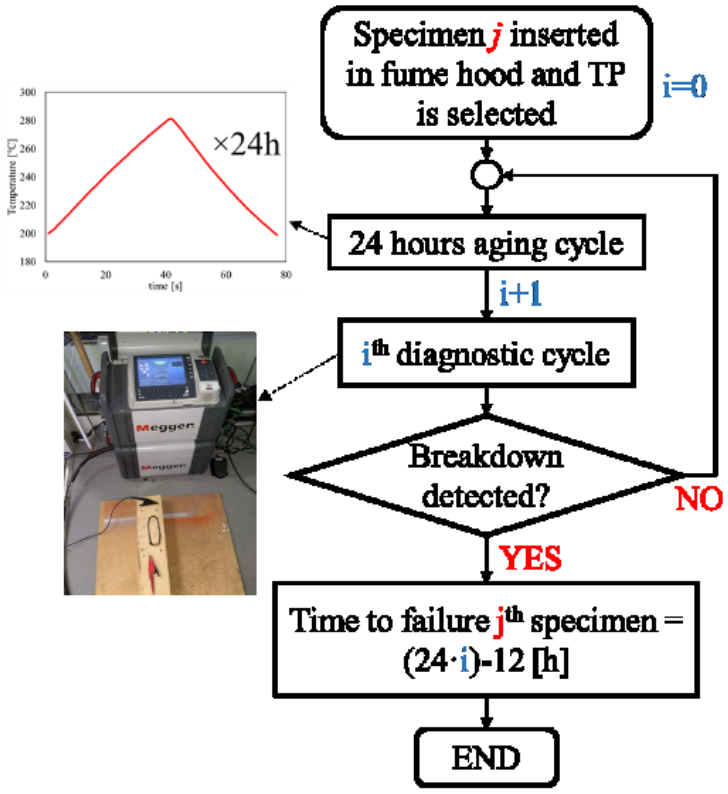

Figure 5.8 – Flow diagram of the testing procedure.

5.3.3 Results and Discussion

The failure times (i.e. number of cycles to failure) are post-processed through the Weibull distribution and the corresponding probability plots with 95% confidence intervals are shown in Figure 5.9. For representation clarity, the probability plots, report only the average of tied points (i.e. if more than one specimen fail during the same diagnostic session, only a single point is reported on the Weibull graph, representing their average cumulative failure probability).

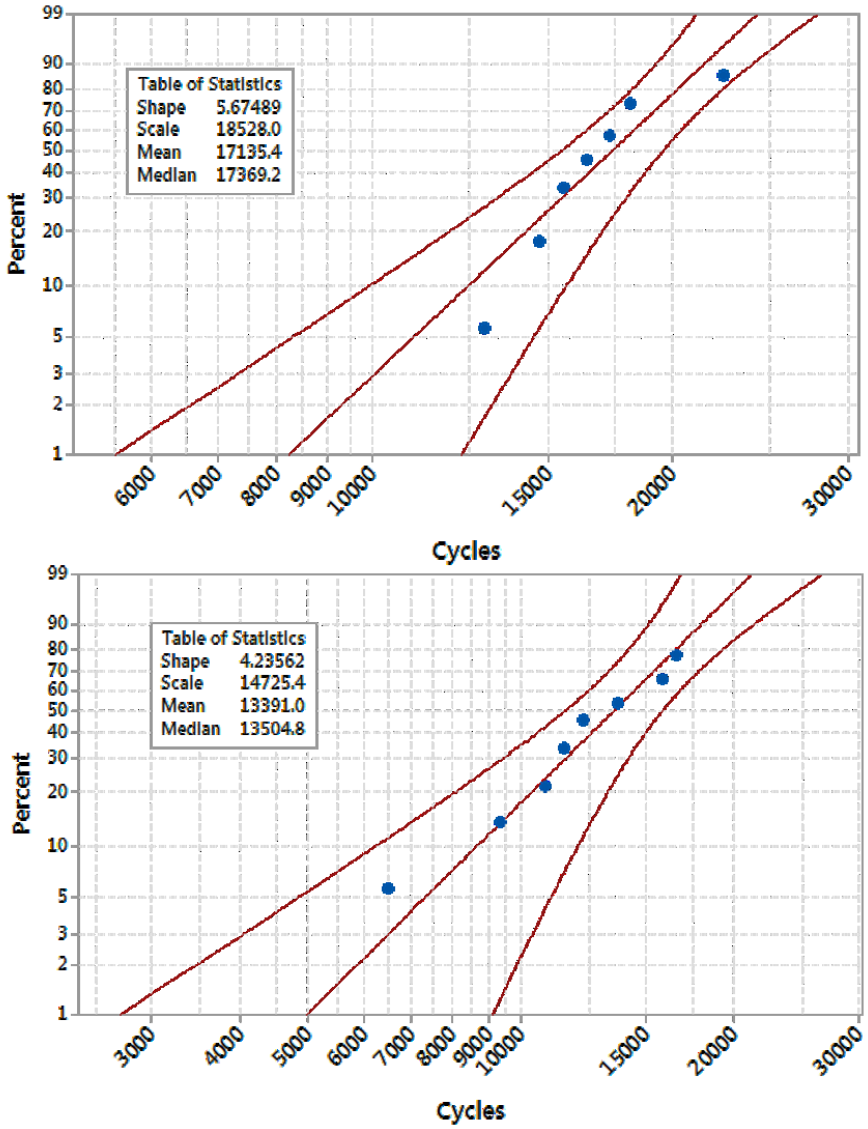

Figure 5.9 – Weibull probability plot of cycles to failure for TP#1 (top sub-plot) and TP#2 (bottom sub-plot).

The following (and most crucial) step consists in verifying if the proposed lifetime prediction model is able to match the experimentally-recorded cycles to failure. For this purpose, the Arrhenius-Miner model of (5.5) is implemented in Matlab® Simulink environment as shown in Figure 5.10, so that the numerical integration can be performed. The instantaneous loss of life fractions relative to TP#1 and TP#2 are reported in Figure 5.11 and Figure 5.12 respectively. Therefore, the predicted cycles to failure are calculated according to (5.6) and they are collected in Table 5.1 where they are apprised with the experimentally measured ones. It is important to recall that the cycles to failure are calculated adopting the 63.2% percentile (i.e. α) of the Weibull distribution.

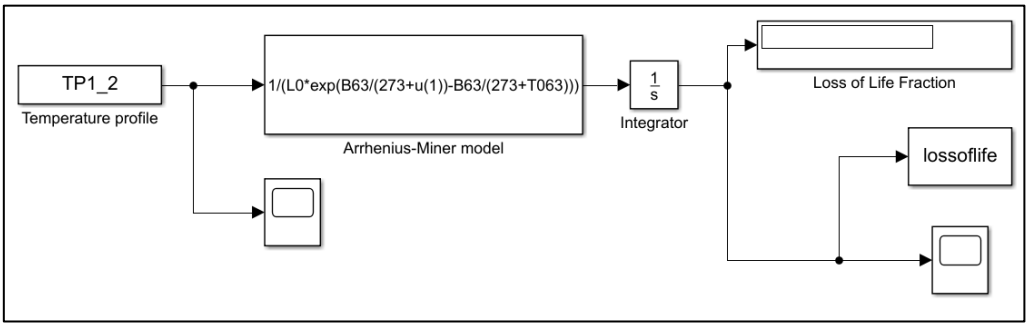

Figure 5.10 – Arrhenius-Miner model implemented in Simulink.

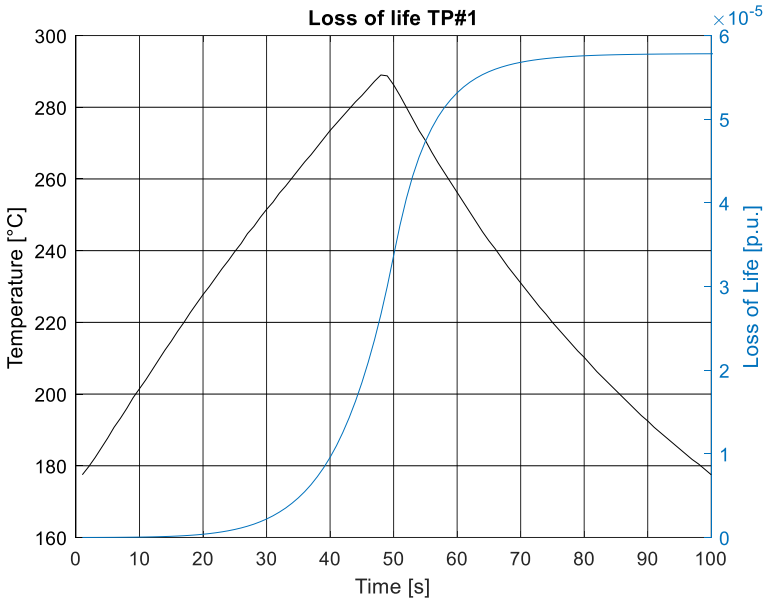

Figure 5.11 – Loss of life fraction for the temperature profile TP#1.

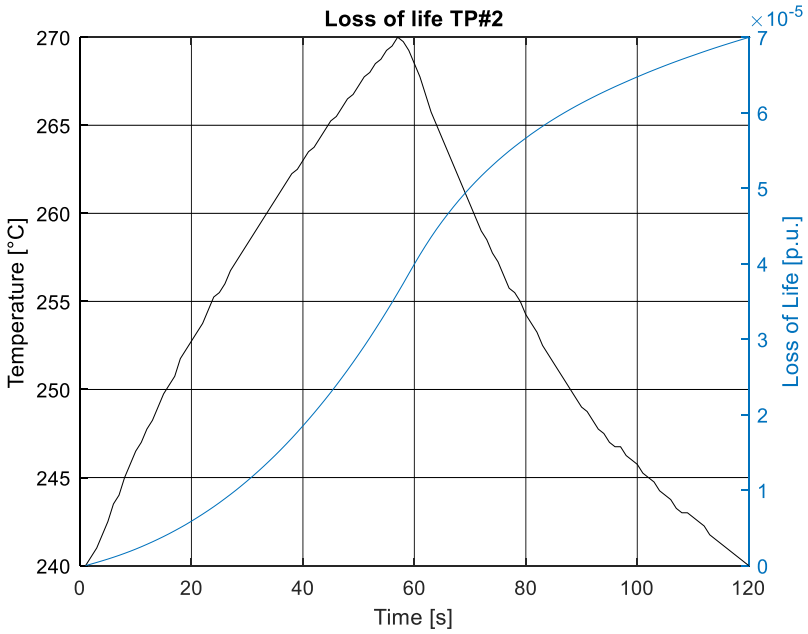

Figure 5.12 – Loss of life fraction for the temperature profile TP#2.

Table 5.1 – Comparison between experimental and estimated failure times (cycles).

Temperature profile	K_α (measured)	K'_α (estimated)	%|error|
TP#1	18528	17288	6.7 %
TP#2	14725	14247	3.1 %

From the obtained results, it can be observed that the proposed model guarantees a fair estimation of the failure time in both cases. The larger mismatch is observed for the profile TP#1, which features a temperature gradient of ≈2.3 °C/s, contrarily to TP#2 where the gradient is ≈0.62 °C/s. This result might indicate that a steeper temperature gradient can introduce additional insulation stresses which the Arrhenius model alone is not able to account for. This result is also partially confirmed by the optical microscope enlargement shown in Figure 5.13, where specimens aged with the profile TP#1 are analysed at the end of their life. Indeed, Figure 5.13 shows some cracks on the coils enamel surface, which might derive from thermally-induced mechanical stresses. This kind of stress is extremely common in large machines, whilst it has never been fully investigated for low voltage, random wound EMs.

It is important to note, however, that a complete machine has a larger thermal inertia than the tested specimen topology (i.e. coils), due to the presence of the stator

core (i.e. large thermal capacitance). As a result, the temperature profile to which the winding is subject can have a more "gentle" gradient than the one of TP#1, guaranteeing the appropriate applicability of the proposed model.

Another important consideration can be made by observing the stress-strain curves of polyamide-imide (i.e. the over-coating material of the tested magnet wire) at various temperature reported in Figure 5.14, provided by a specialised polymers manufacturer [136]. From this figure it is possible to state that the elasticity of polyamide-imide progressively deteriorates when the temperature is increased. This might explain the cracks on the aged specimens' enamel. Based on these considerations an important conclusion can be drawn. That is, if the winding temperature of variable duty EMs does not exceed "too much" [1] the thermal class temperature, then, the Arrhenius model provides accurate lifetime prediction results, independently on the thermal gradient value. Obviously, experimentally-validating such hypothesis might require several years of testing.

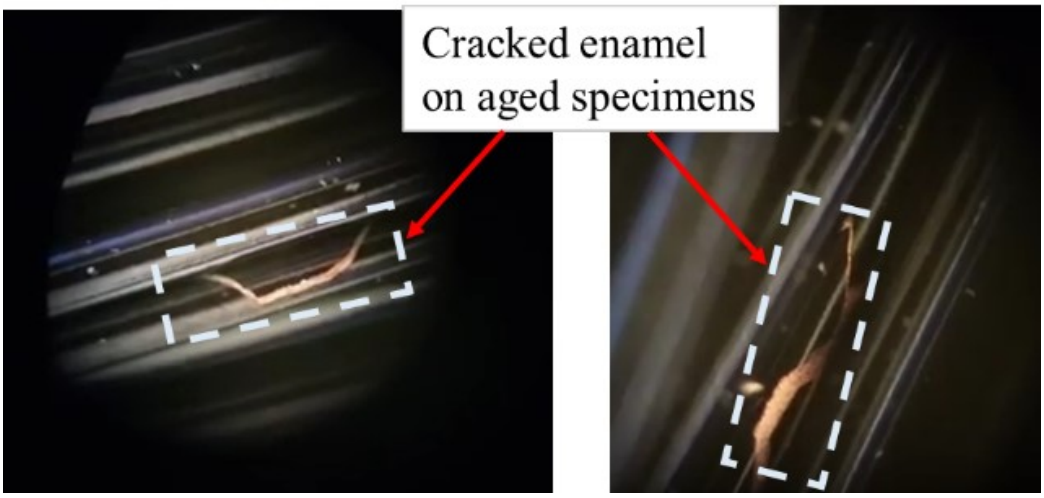

Figure 5.13 – Optical microscope enlargement for specimens aged with TP#1 at the end of their life.

[1] The precise numerical value can only be evaluated if the wire's manufacturer would provide the stress-strain curve, for various temperatures, of the polymeric enamel; based on this Author's experience, unfortunately, these data are not often provided.

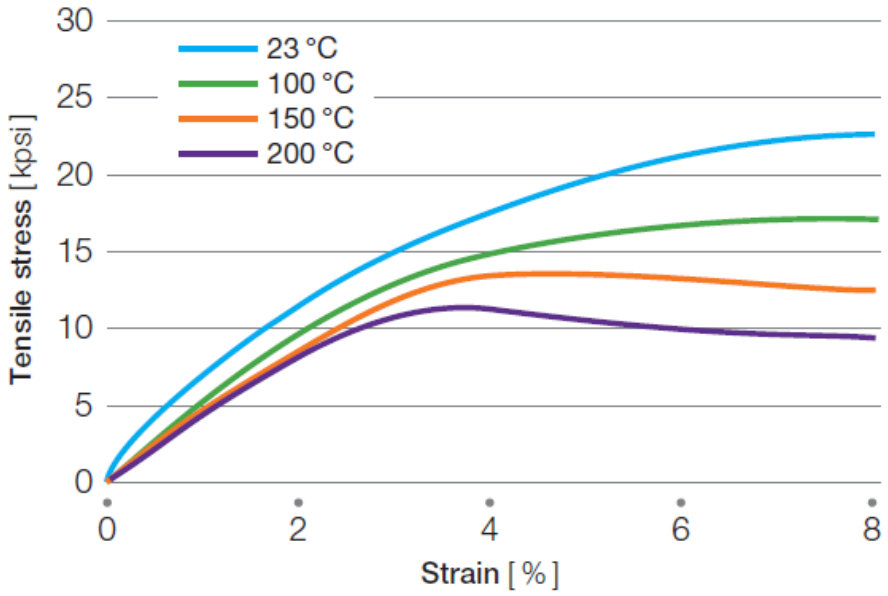

Figure 5.14 – Stress-strain curves of Torlon® polyamide-imide resin at various temperatures [136].

All the above shows how the proposed model for evaluating the winding insulation degradation in short duty cycle EMs has been validated. To prove the quality of this novel proposed method, and for demonstrating how what presented would fit in the design process of real electric motors, various case-studies are reported below.

5.4 Case-Study: Helicopter Actuator

The 12 slot / 10 pole EM introduced in Chapter 3, i.e. in Figure 3.1 and Table 3.2, is considered as a first short-duty application case-study. The selected machine, drives a helicopter nose landing gear extension / retraction mechanism as schematically illustrated in Figure 5.15. This particular EMA (i.e. landing gear) is only powered after taking off and just before landing. Therefore, it is activated for a short time-period compared to the total flight duration. In addition, as the landing gear is only operated at low altitudes, it can be safely assumed that the EM operates at sea level pressure. Hence, the enhancement on the PD activity, due to low pressure, does not apply to the considered case-study, which therefore operates under a PD-free regime. This implies that the prevailing aging factor is that of the sole effect of thermal stress. The time necessary for a single extension / retraction is equal to 20 s. However, for safety reasons,

the EMA should be able to perform three extension / retraction cycles in a row without any cooling-down time, according to the mission profile reported in Figure 5.16.

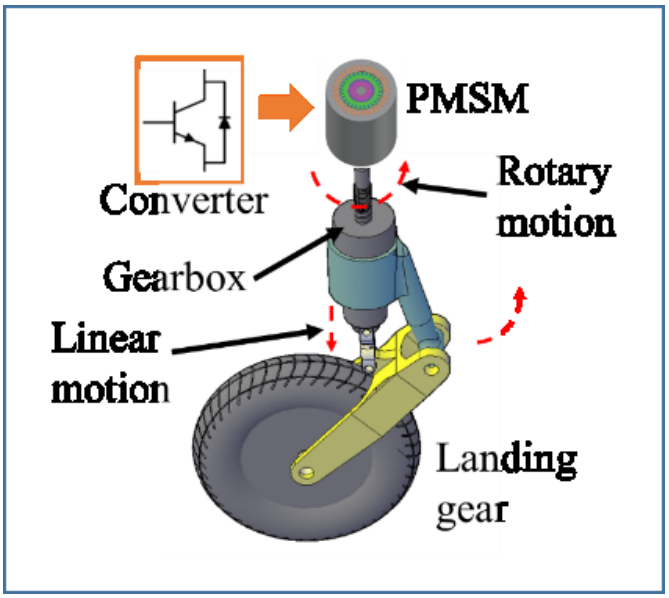

Figure 5.15 – Diagram of the helicopter landing gear EMA.

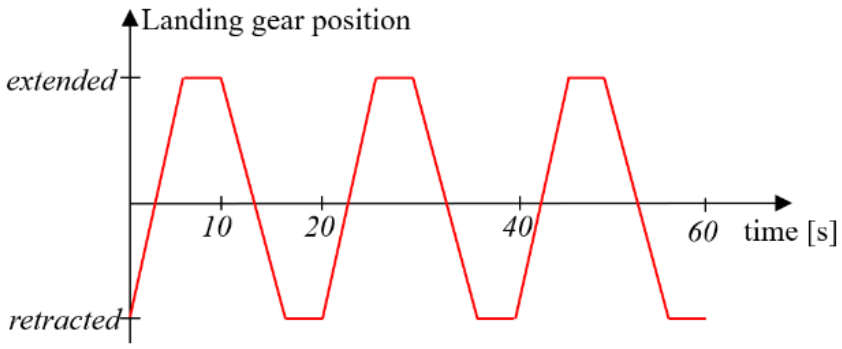

Figure 5.16 – Landing gear EMA mission profile.

The LPTN described and experimentally-tuned in Chapter 3, which is shown in Figure 4.2, is used for predicting the winding hot-spot temperature during an EMA mission. For this purpose, the starting ambient temperature is set to 70 °C, in order to have a scenario which is even "worse" than what one would expect in practice. The resulting temperature profile, *TP#EMA*, for a 120 s time-window simulation is shown in Figure 5.17. From Figure 5.17, it can be observed that the temperature gradient is ≈0.9 °C/s which is within the applicability limits of the proposed lifetime model, as explained in the previous section. In order to predict the number of cycles to failure,

the simulated hot-spot temperature profile is used as input for the Arrhenius-Miner model. The ensuing instantaneous loss of life functions relative to the 63.2th percentile of the Weibull distribution is shown in Figure 5.18. The predicted number of cycles to failure for various percentiles of the Weibull distribution are calculated according to (5.6) and they are reported in Table 5.2.

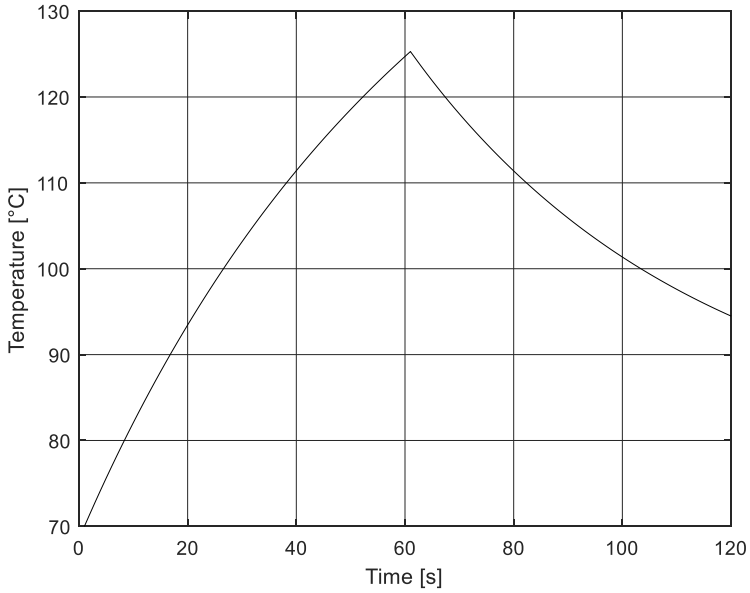

Figure 5.17 – Temperature profile TP#EMA.

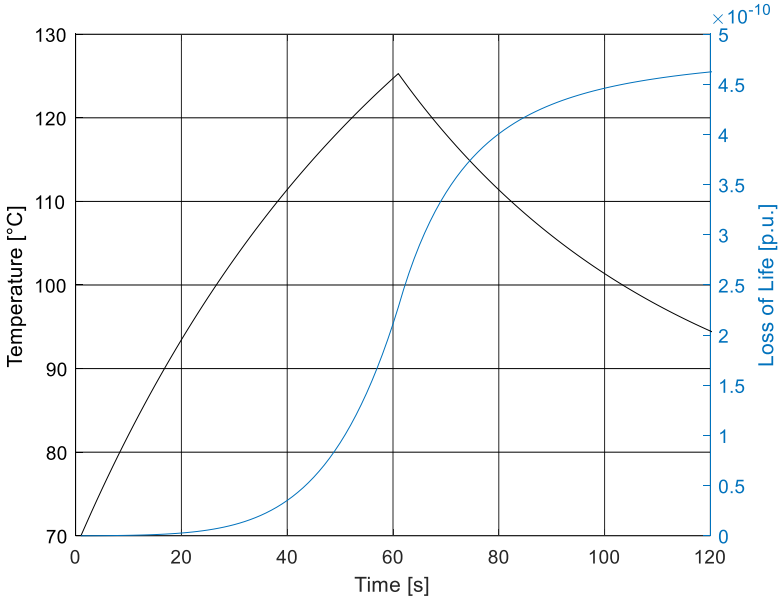

Figure 5.18 – Loss of life relative to the 63.2% percentile of the Weibull distribution for TP#EMA.

Table 5.2 – Predicted number of cycles to failure using the Arrhenius-Miner model.

Percentile	*K'*
10%	$1.01621 \cdot 10^9$
50%	$1.90866 \cdot 10^9$
63.2% (α_{EMA})	$2.16006 \cdot 10^9$

The Weibull CDF of the cycles to failure, for the turn to turn insulation stressed with the profile TP#EMA, can be now obtained. The CDF will have scale factor α_{EMA} (see Table 5.2) and shape factor 2.987. The latter has been experimentally determined through accelerated aging tests at constant temperature performed on the coils, as reported in Section 4.2.6. The Weibull CDF relative to the temperature profile TP#EMA is shown in Figure 5.19.

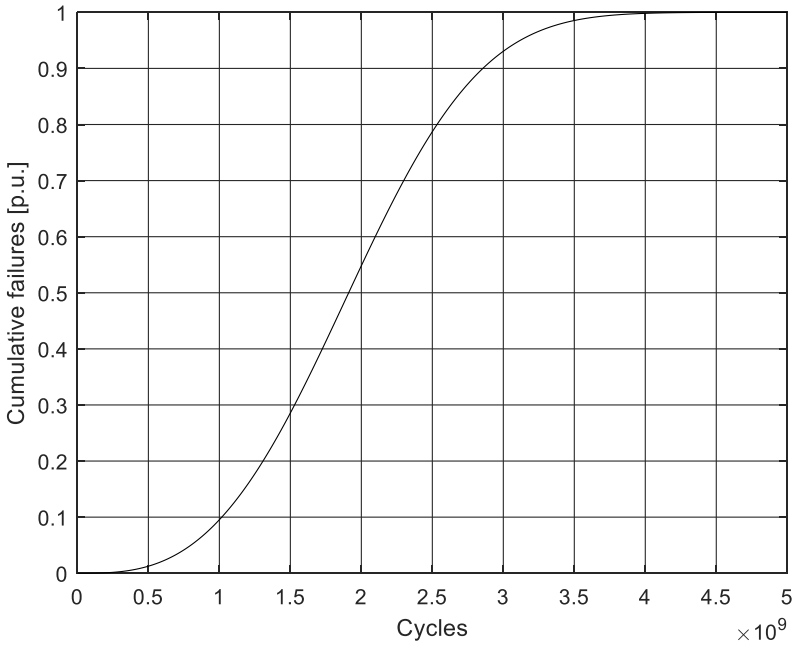

Figure 5.19 – Weibull CDF of cycles to failure for TP#EMA.

The CDF allows to easily assess the probability of failure (for thermal cycling aging) of the PMSM EMA at any point in time (i.e. after any number of activations). Assuming that the PMSM has to safely operate for 10,000 cycles before being replaced, its probability of failure (at the end of its life), calculated as in (5.8), is equal to $1.16 \cdot 10^{-16}$. For this calculation the size-effect has been neglected for the same reasons reported in Section 4.3.

$$F(10000) = 1 - \exp\left[-\left(\frac{10000}{2.16006 \cdot 10^{10}}\right)^{2.987}\right] \tag{5.8}$$

From the obtained result it is clear that the PMSM is over-engineered from the thermal point of view, due to the adoption of safety factors at the design stage. Hence, its expected lifetime largely exceeds the reliability requirements for safety-critical systems (generally, the probability of failure limit for safety-critical systems is 10^{-9}).

5.5 Case-Study: Traction Motor

A traction PMSM is used as second case-study for demonstrating the power and convenience of the proposed lifetime assessment methodology. The aim of this case-study is to verify how applying the enhanced end-winding cooling method presented in Section 3.3 and shown in Figure 3.9, can strongly extend the insulation lifetime. For doing so, it is supposed that the PMSM is installed on a full-electric mini-van. The main design parameters of the PMSM are listed in Table 5.3.

Table 5.3 – Main design parameters of the case-study traction PMSM.

Parameter	Quantity
Rated power	78.5 kW
DC link voltage	540 V
Rated speed	4500 rpm
Rated torque	166 Nm
Rated current	275 A
Winding type	Concentrated
Parallel paths	2
Current density	12.5 A/mm^2
Cooling method	Forced liquid
Core material	Vacoflux 17
PM material	SmCo

For verifying the thermal performance of the PMSM, a standardized European driving cycle is assumed, that is the EUDC [137]. This is an extra-urban cycle and it is reported in Figure 5.20. The EM torque necessary for satisfying the EUDC cycle is computed by implementing in Simulink® environment the full model of the drivetrain. The model is omitted here, as it is out of the main scope/topic of this work. The winding current profile is easily computed by dividing the instantaneous torque by the EM

torque constant (the machine operates in linear region and without field weakening). The PMSM hot-spot temperature is predicted using the LPTN presented in Section 3.3 (see Figure 3.11) in two different conditions, namely with and without the application of the end-winding cooling pipe. The LPTN simulation results are reported in Figure 5.21 and they correspond to the EUDC cycle, continuously applied for one hour. Assuming for the EM winding the same magnet wire presented in Chapter 4 whose details are tabulated in Table 4.1, it is clear that the configuration without end-winding cooling clearly exceeds the wire's insulation thermal class (i.e. declared class 220).

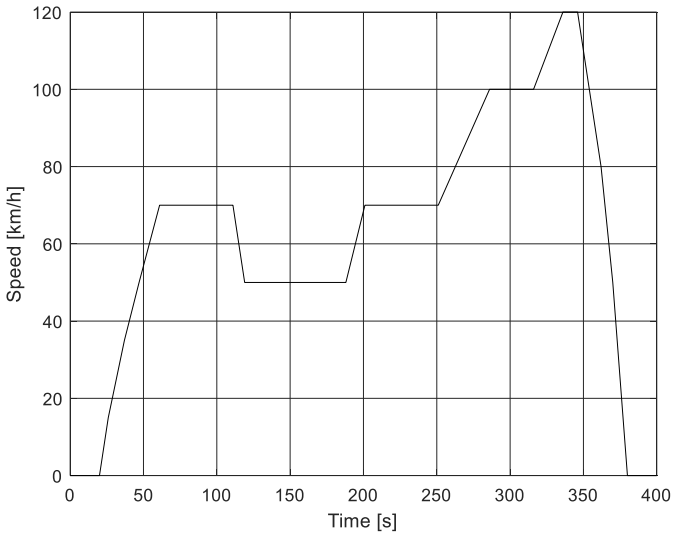

Figure 5.20 – Extra-urban European driving cycle EUDC.

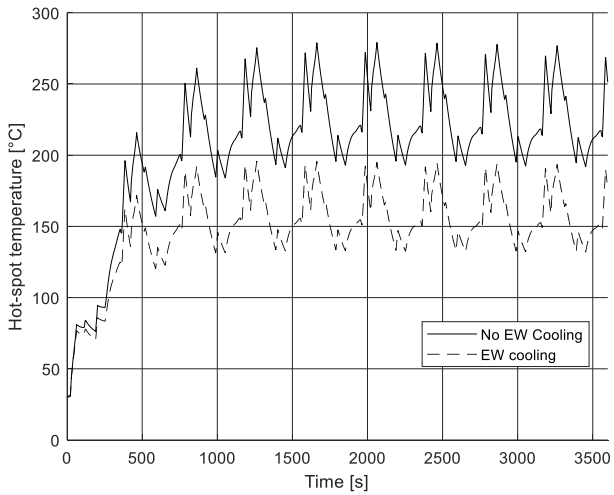

Figure 5.21 – Hot-spot temperature profile for the case-study traction PMSM operating with the EUDC driving cycle.

The Arrhenius-Miner model for insulation lifetime prediction is adopted for evaluating the EM insulation reliability in two different cases, namely with, *TP#AU-C,* and without, *TP#AU-NC,* end-winding cooling. The assessment is performed under the following assumptions:

1. The reliability computation is carried out by assuming that the EM operates for its whole life under the EUDC profile. This hypothesis is on the conservative side, as road vehicles do generally experience various driving-cycles/conditions (less demanding than the EUDC one) throughout their lifespan.
2. The PMSM insulation is expected to be exempt from partial discharges (i.e. PD-free). This might not be true, as the DC link voltage is 540 V, and thus further verifications are necessary as will be explained in Chapter 6.
3. It is assumed that the insulation aging is mainly caused by thermal effects by neglecting any mechanical stresses. However, it is acknowledged that automotive systems are subject to excessive vibration levels, which can compromise/shorten the PMSM's insulation lifetime.
4. Further, the (worst-case) temperature profile gradient (see Figure 5.21) is ≈2.5 °C/s. This gradient value is slightly above than 2.3 °C/s, which was experimentally verified to provide accurate lifetime prediction results with the Arrhenius-Miner model.

The two temperature profiles are used as input for the insulation lifetime prediction model, and the resulting loss of life functions, over one hour simulation, are reported in Figure 5.22 and Figure 5.23 for TP#AU-NC and TP#AU-C respectively. The predicted failure times, for various percentiles of the Weibull distribution are summarised in Table 5.4. From these results, it is evident the enormous amount of lifetime extension caused by the enhanced end-winding cooling. It is also possible to conclude that without additional cooling, the original PMSM configuration is not suitable for such kind of automotive application, as its predicted lifetime is way below

10,000 h (the standard life of an automotive traction motor, i.e. 500,000 km driven at an average speed of 50 km/h).

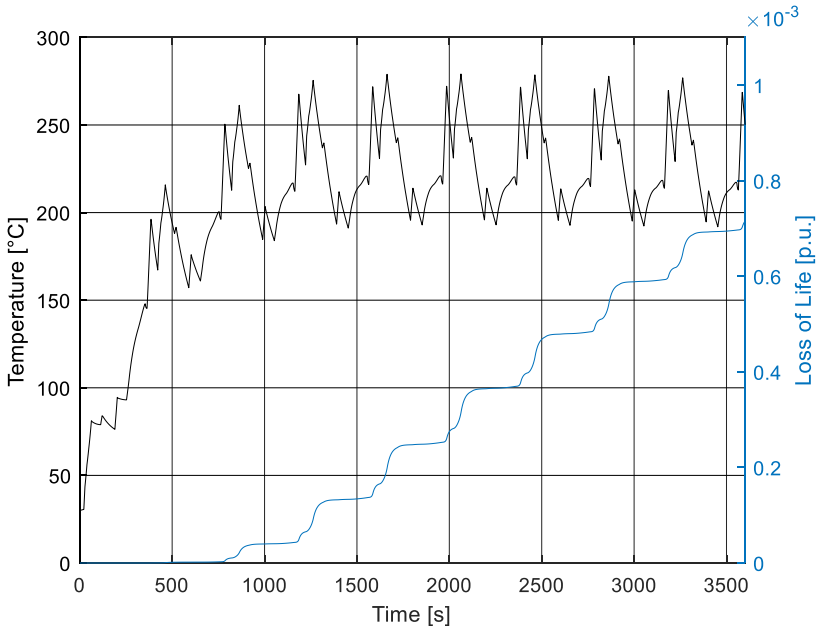

Figure 5.22 – Loss of life relative to the 63.2% percentile of the Weibull distribution for TP#AU-NC applied for 1 h.

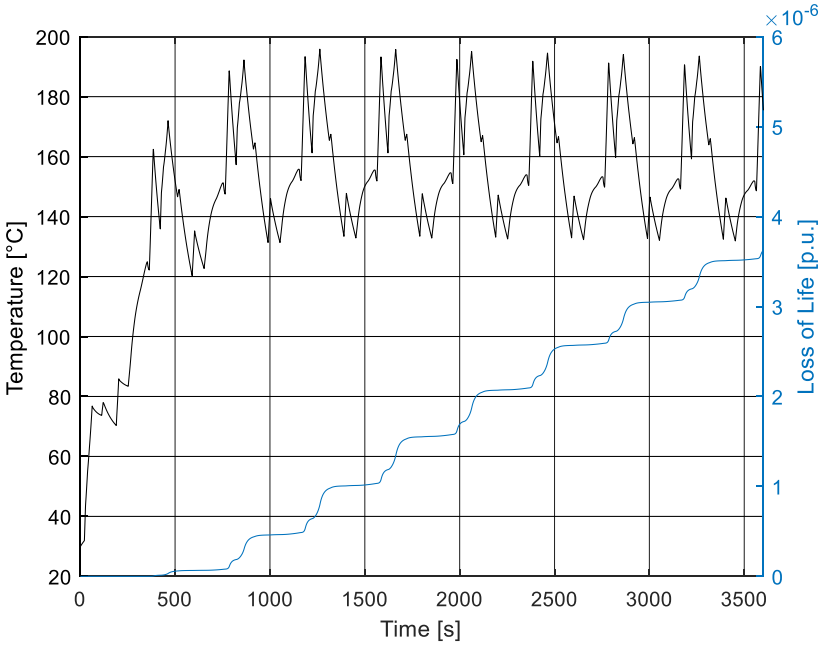

Figure 5.23 – Loss of life relative to the 63.2% percentile of the Weibull distribution for TP#AU-C applied for 1 h.

Table 5.4 – Predicted time to failure for various percentiles of the Weibull distribution using the Arrhenius-Miner model.

Percentile	$K'_{TPAU\text{-}NC}$	$K'_{TPAU\text{-}C}$
10%	657 h	$129.7 \cdot 10^3$ h
50%	1234 h	$243.6 \cdot 10^3$ h
63.2% (α)	1397 h	$275.7 \cdot 10^3$ h

After implementing the enhanced end-winding cooling, the PMSM reliability, at any time-instant *t,* can be computed as in (5.9) where α is the scale factor of the Weibull distribution (i.e. $275.7 \cdot 10^3$ h – as reported in Table 5.4) and β is the shape factor, which for the considered insulation is equal to 2.987, as demonstrated in Section 4.2.6.

$$R(t) = 1 - F(t) = \exp\left[-\left(\frac{t}{\alpha}\right)^{\beta}\right] \tag{5.9}$$

After 10,000 h of operation, under the EUDC driving cycle, the PMSM adopting the proposed end-winding cooling method features a reliability of 99.99502 %. This value is fairly elevated, however, it must be pointed out that it only considers failures of electrical nature on the turn to turn insulation caused by thermal aging. Nonetheless, the application of the proposed lifetime assessment methodology allows to confidently state that the EM is correctly sized from the thermal loading point of view. Such achievement clearly derives by the cooling improvement provided by enhanced the end-winding thermal management. This case-study shows how the lifetime prediction model can be used at an early design stage for validating/verifying the appropriateness of thermal management choices.

5.6 Case-Study: Propulsion Motor for UAV

The third case-study is related to an outer rotor brushless DC (BLDC) machine, used of propelling a lightweight radio-controlled unmanned aerial vehicle (UAV) i.e. drone. The BLDC topology features an excellent power density compared with conventional brushed DC motors, while maintaining a relatively simple control strategy [138].

Differently from the case-studies in Section 5.5 and Section 5.6 above, this case-study is not developed on an already-existing machine, but it is actually a completely newly designed motor by the Author. It is very important to note that here the objective goes beyond a simple evaluation of "degradation and/or prediction of lifetime for EMs". In fact, the objective here is to propose an innovative PoF-oriented design methodology for EMs. To the Author's knowledge, this design philosophy is completely inexistent in literature for EMs and it is considered a main novelty of this Thesis.

5.6.1 Mission profile and reliability constraint

For this case-study machine, a reliability constraint is imposed at the design stage. Namely, the BLDC should be able to perform the mission profile reported in Figure 5.24 for 5000+ times, with an insulation failure probability lower than 1.5 %.

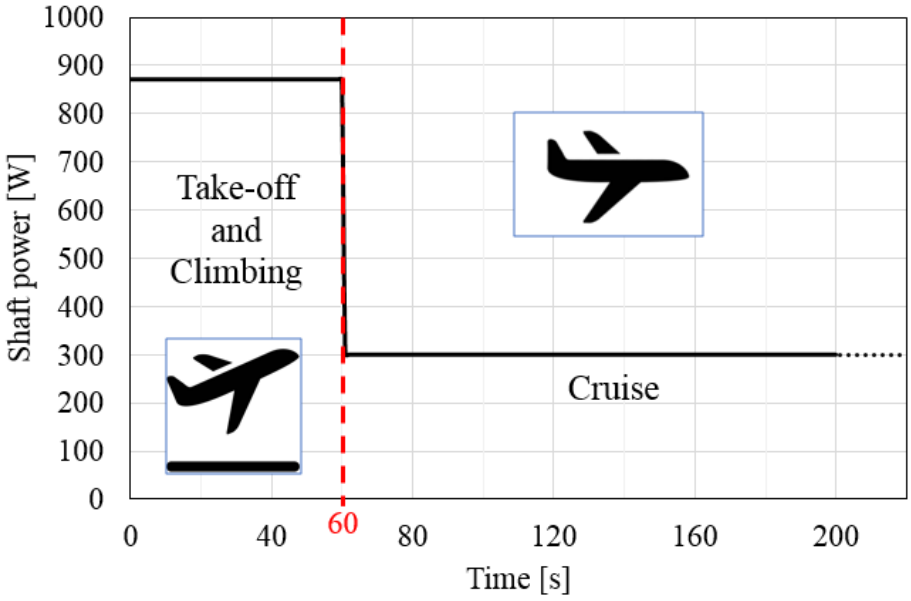

Figure 5.24 – UAV mission profile and required power at the EM shaft – the speed is 10,000 rpm.

A major constraining factor in light UAVs (and mobile applications in general) is the energy storage system. In fact, capacity (i.e. energy storage rating in Ah), voltage level (i.e. number of series-connected cells) and overload capability of the battery pack play a key role. For the application at hand, the available energy storage system is a

5000 mAh (rated capacity) lithium-polymer battery, with 6 series cells (i.e. DC link ≈22.2 V) and an overload capability of 30C, resulting in 150 A peak current.

5.6.2 Conventional Design Approach

A BLDC, defined hereafter as "*Prototype A*", is initially designed adopting a conventional approach. Because of the limited DC link voltage, it is obvious that the insulation reliability of the EM is strictly related to its operating temperature. Prototype A is designed in such a way that its hot-spot temperature stays always below the magnet wire thermal class, which in this case is 200 °C. This design procedure will lead to an over-engineered machine that will be immune to excessive thermal aging, and will naturally comply with the reliability specification.

The BLDC geometrical dimensions are chosen by re-scaling those of a commercially available motor, which is shown in Figure 5.25. The machine features a 12 slot / 14 pole configuration with concentrated winding. For complying with the limited DC link voltage, the winding is delta-connected with two parallel branches [139]. The main design quantities of Prototype A are listed in Table 5.5.

From Figure 5.25, it can be observed that the BLDC has open end caps on both drive- and non-drive ends. This provides excellent air flow through the EM stator (comparable with forced air cooling), enhanced by the propeller's induced turbulence.

Table 5.5 – Prototype A – design parameters.

Design Parameter	Quantity	Unit
Base speed, n	10,000	rpm
Pole pairs, p	7	-
Slot number, Q	12	-
Windings layout	Conc.	-
Phases	3	-
Turns per coil, n_t	10	-
Parallel paths	2	-
Copper slot fill factor, ff_W	42	%
Axial length, L	30	mm
Armature diameter	40	mm

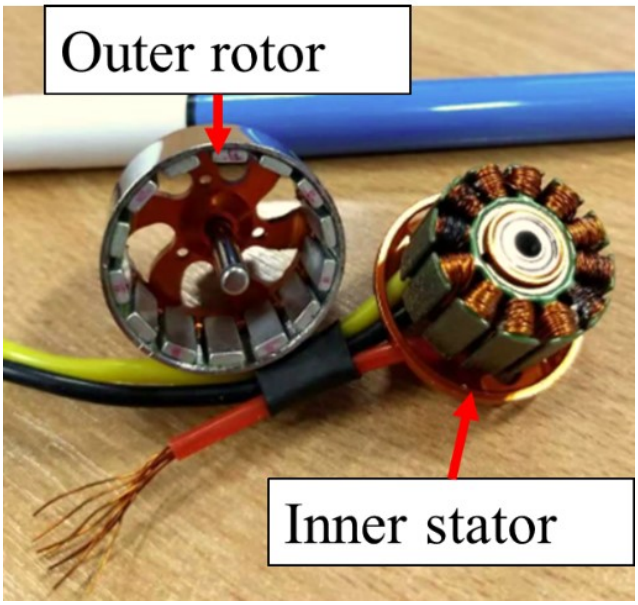

Figure 5.25 – Outer rotor BLDC motor.

Electromagnetic FE simulations have been run for determining the EM's performance and the ensuing instantaneous torque plots are reported in Figure 5.26 for both rated (i.e. continuous) and overload (i.e. peak) conditions. A considerable torque ripple, caused by the delta-connected winding (i.e. presence of 3rd order field harmonics), is observable in Figure 5.26. By multiplying the (average) torque with the rotational speed (i.e. 10,000 rpm · 2π/60), it can be easily verified that the power constraints in Figure 5.24 are met.

The rated torque is generated by feeding the winding with a current density J of 4.2 A/mm^2, while 12 A/mm^2 are needed for producing the peak torque. These values are highly conservative for a "forced air-cooled" EM, especially considering the short time-period overload of the application under study (i.e. 60 s). Thus, it is easy to verify that the hot-spot temperature is lower than the insulation's thermal class in every operating condition. This design approach clearly results in an over-engineered EM, as the materials within the machine (in particular the insulation) are not totally exploited, resulting in poor power density performances.

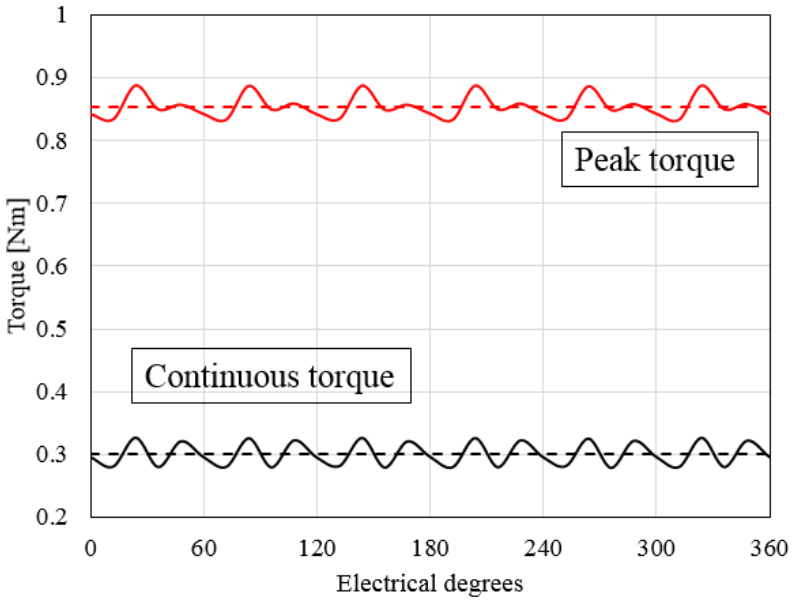

Figure 5.26 – Peak and continuous torque for Prototype A at base speed.

5.6.3 Physics of Failure – Based Design Approach

The second prototype, defined hereafter as "*Prototype B*", is designed by imposing the reliability constraint as a main design objective in order to optimise the insulation system design to its full potential. The new EM, known as Prototype B, is therefore conceived for working above the thermal class of 200 °C, while meeting the required 5000+ missions objective. The radial geometry of Prototype B is kept identical to the one of Prototype A, whereas its axial length is shortened from 30 to 20 mm, allowing for a more compact design. Since a shorter machine reveals a lower per-turn back EMF, the turns number of Prototype B is modified according to the available DC link voltage. After a sensitivity analysis, based on electromagnetic FE simulations, the selected number of turns per coil results equal to 13. This means modifying the magnet wire diameter for keeping unchanged the slot fill factor. Apart from L and n_t, all the remaining design parameters have been kept equal to those reported in Table 5.5.

Due to the afore-mentioned modifications (i.e. axial length and turns number), the power requirements are fulfilled by increasing the phase current (compared to Prototype A), hence, enhanced thermal loadings are achieved. In particular, 6.3 A/mm^2 and 18.9 A/mm^2 (for up-to 60 s) are the current density values during rated and overload

operations respectively. The latter value is extremely demanding in terms of thermal management. Therefore, further verifications are necessary for assessing if the reliability constraint is met. From the electromagnetic point of view, Prototype B can satisfactorily provide the required torque as shown in Figure 5.27.

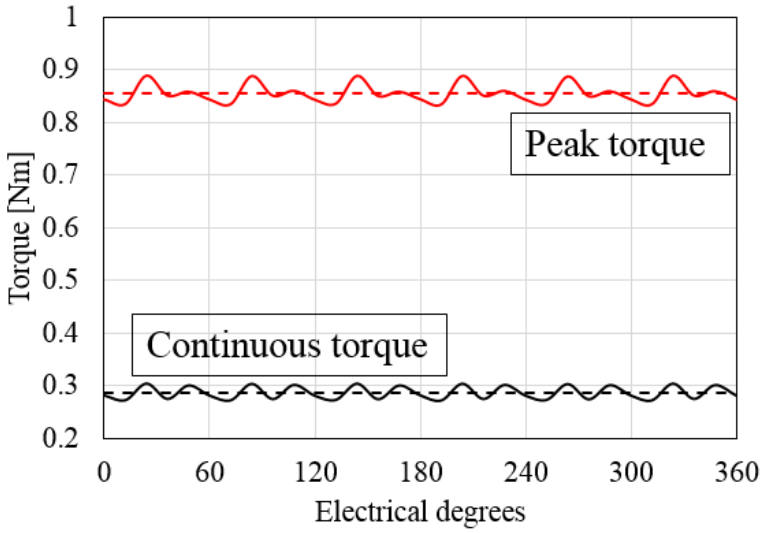

Figure 5.27 – Peak and continuous torque for Prototype B at base speed.

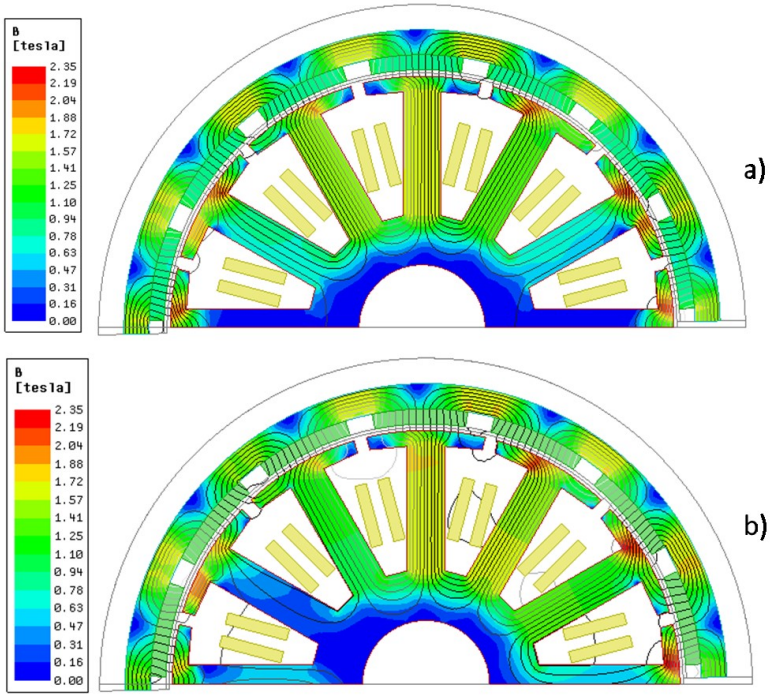

Figure 5.28 – Magnetic flux density and field lines in overload condition (i.e. take-off). a) Prototype A, b) Prototype B.

For completeness, Figure 5.28 shows the magnetic flux density and field lines for the two designed prototypes operating in overload condition (i.e. take-off), which is the most demanding situation electromagnetically. It is possible to note that the magnetic flux density in the teeth region of Prototype B is slightly higher in magnitude than in Prototype A. Nonetheless, the magnetic flux path for both EMs does not a show deep magnetic saturation level, proving that the magnetic core is properly sized.

The winding temperature profile, during a mission, is evaluated via a combined LPTN – CFD approach. The thermal analysis is omitted here for not to divert attention from the main objective (i.e. reliability), but it is reported in Appendix A for completeness.

The thermal simulation outcome, relative to the UAV's mission, is reported in Figure 5.29, where the hot-spot temperature profile for Prototype B is plotted. It is possible to note that the temperature rises up-to 280 °C during the first stage of the mission and then it settles at the steady-state value of 147 °C throughout the cruise flight stage. The thermal profile portion, outlined in the red dashed box of Figure 5.29 and defined hereafter as *TP-UAV*, is above the insulation's thermal class, and it is employed for investigating the impact of thermal overload on the insulation's lifetime.

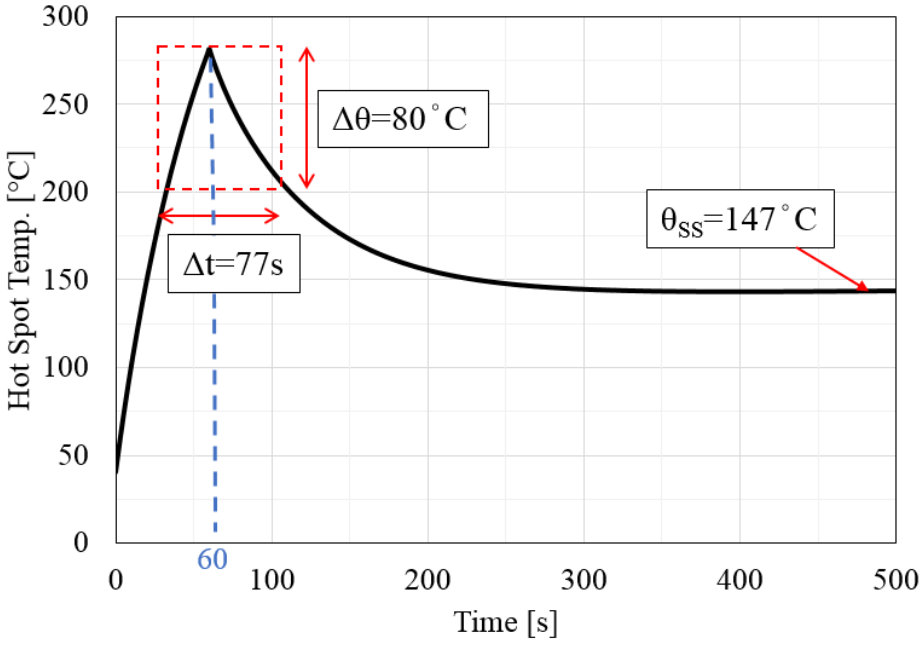

Figure 5.29 – LPTN-estimated hot-spot temperature for Prototype B during a single mission profile.

A total of 12 coils (i.e. specimens) have been wound adopting a Grade 2, class 200 magnet wire (i.e. the same wire used for both prototypes' windings), adopting the layout described in Section 4.2.1. The wire's enamel features a polyester-imide base coat and a polyamide-imide overcoat layer. The specimens are subject to a thermal cycling aging campaign, identical to the one reported in Section 5.3.2 as shown in Figure 5.8. However, in this case, the applied (aging) temperature profile is TP-UAV.

The collected failure times data are post-processed via the Weibull distribution, as reported in Figure 5.30. Considering the probability plot, it is possible to observe that the 1% percentile of the Weibull distribution, corresponds to 8,360 cycles to failure (i.e. UAV missions). Therefore, Prototype B fulfils the reliability requirement (i.e. 5000+ missions) and a wide safety margin is secured. For completeness, the survival function plot (i.e. reliability function), is provided in Figure 5.31. Despite the significant thermal stress, the survival probability is still above 95% after 10,000 overload cycles. It is worth remarking that the selected end of life criterion is highly conservative, since a voltage up-to 500 Vrms is applied to the aged coils during the diagnostic sessions. This approach compensates for having overlooked other insulation stressing factors (e.g. mechanical vibrations) in the introduced study.

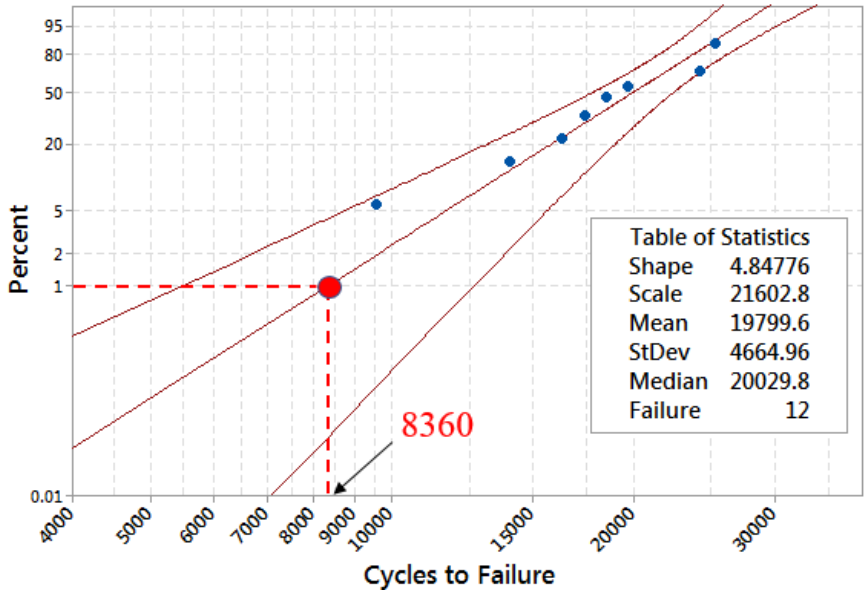

Figure 5.30 – Weibull probability plot of the specimen's time to failure.

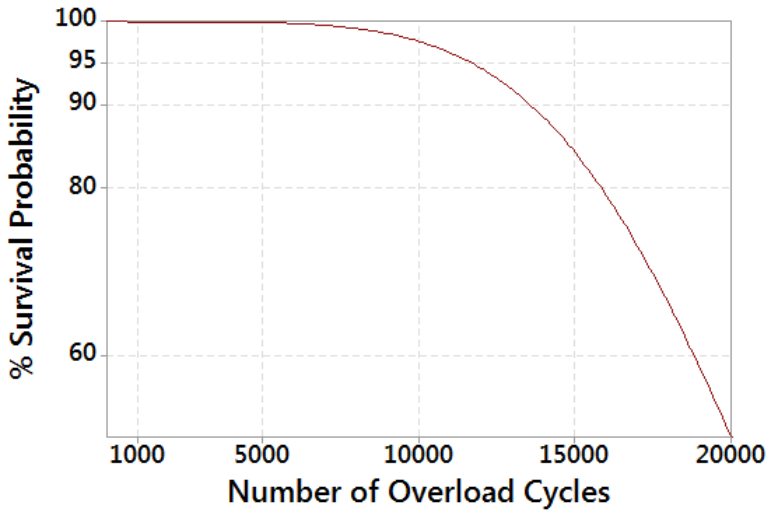

Figure 5.31 – Weibull survival probability plot of the tested specimens.

At this stage, it is important to "remember" that Prototype B is 33% shorter than Prototype A, which was designed according to standard sizing techniques, without any PoF insight. As described above, Prototype B is able to deliver the same torque performance of Prototype A, by having an increased current loading (i.e. much higher thermal losses) to compensate for the "lost" magnetic circuit. Both machines show similar performances in terms of efficiency, when developing the rated torque (≈ 90%). It is true that the higher winding temperature of Prototype B during take-off and climbing causes a Joule loss increment. However, it is worth recalling that the aforementioned flight stage lasts only for 60 s, and thus it represents only a minimum fraction of the full mission profile. On the other hand, all the above clearly indicates that Prototype B can survive the required 5000 cycles, and therefore the increased thermal stresses are still within a range with guarantees a satisfactory life duration. For the Author, this is considered to be the real "beauty" of the proposed reliability-oriented process, where it is clear that the traditional over-engineering in the name of safety has now been stripped away, therefore improving the power density without any compromise whatsoever on the lifetime or reliability of the device.

To fully appreciate this concept, one can consider the difference between Prototype A and Prototype B in Figure 5.32. Based on the presented results, the application's power requirements can be met adopting a machine whose axial length is

33% shorter than the original design, as highlighted in Figure 5.32. In practice, the 33% axial length reduction also leads to a 31.6% weight contraction. In fact, the active weight of Prototype A is equal to 0.308 kg against the 0.211 kg of Prototype B. This translates in a 0.3 kW/kg (i.e. 9.5%) power density improvement (i.e. from 2.8 kW/kg to 3.1 kW/kg). Another perceived advantage of this is of course that related to cost, as a smaller machine usually means a lower financial effort.

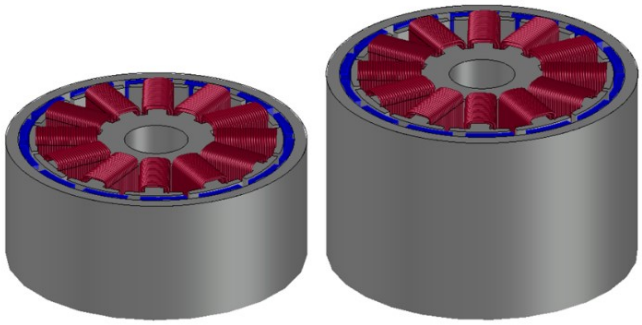

Figure 5.32 – 3D view of the designed prototypes (left-hand side Prototype B and right-hand side Prototype A).

5.7 Concluding Remarks

The main aim of this Chapter was to evaluate if, and under which conditions, the Arrhenius model for thermal aging, combined with the cumulative damage law, can satisfactorily predict the lifetime of variable/short-duty electrical machines. A novel model for the lifetime prediction of the windings of EMs operating in transient-modes was proposed and validated. The results, obtained from the accelerated thermal aging tests at constant temperature, are used for building an insulation lifetime prediction model, for aging originated by variable temperatures. The model has been experimentally validated with excellent accuracy using custom-designed specimens. Two case-studies are presented with the aim of demonstrating how the proposed model can be implemented for assessing the lifetime of real machines. The Chapter concludes with a third case-study, whose aim was to propose a novel design approach, in which reliability and physics of failure concepts play a primary role in the design stage of an electric motor. In this case, the accelerated thermal cycling tests serve for quantifying

the failure probability of the designed prototypes, contrarily to the previous cases (see Sections 5.4 and 5.5) where the reliability assessment was carried out through the Arrhenius-Miner model.

The full impact of the proposed reliability-oriented design process is clear when one observes the potential of design improvement shown in Figure 5.32. The proposed methodology offers the possibility to remove traditional over-engineering without compromising reliability. This breakthrough methodology is visually summarised in Figure 5.33.

This Chapter is considered to be an important one for this Thesis. The work contained in it has resulted in two journal papers [140, 141] and one Conference Paper [142].

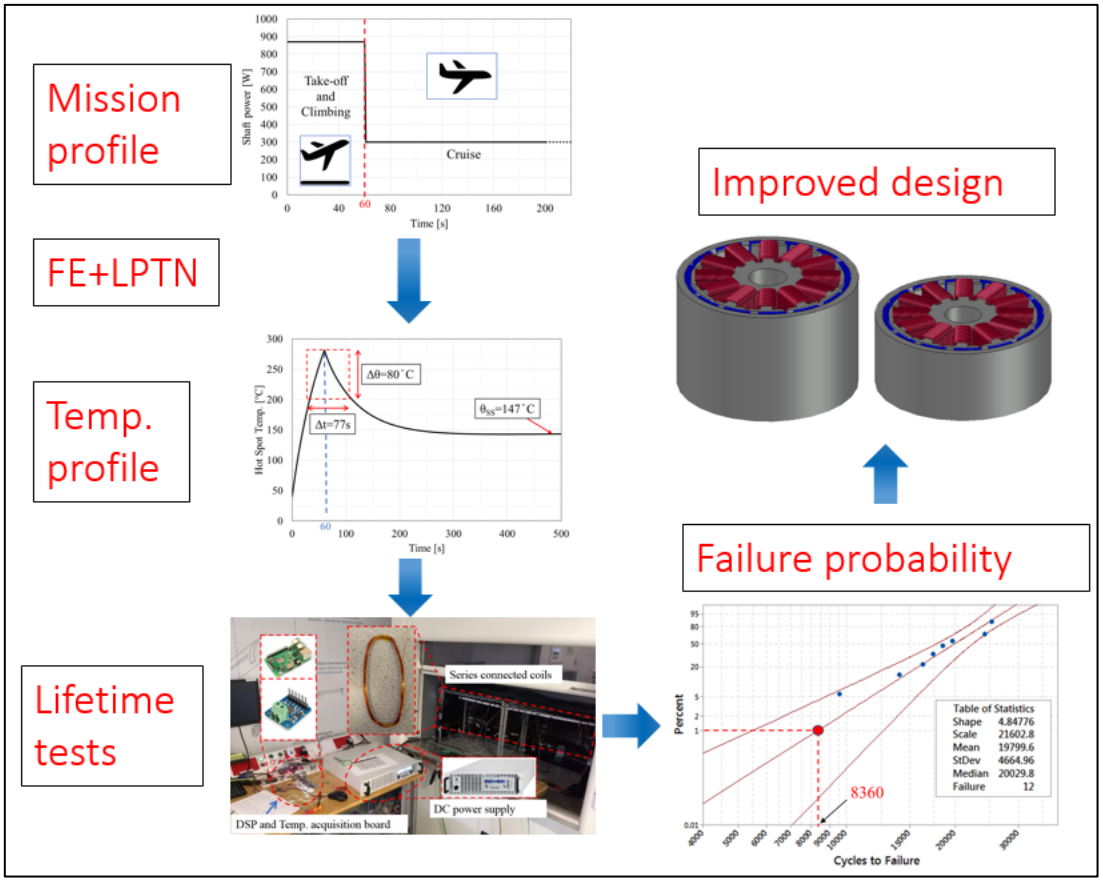

Figure 5.33 – Proposed reliability-oriented design of electrical machines.

Chapter 6 Partial Discharges in Low Voltage Electrical Machines

The core of this Thesis has so far been on insulation failures of electrical nature caused by thermal effects. Indeed, these are widely recognised by the scientific and industrial communities as one of the main causes of premature failure in low voltage EMs (see Chapter 2). In all the presented case-studies, it has been assumed that the winding insulation operates in a PD-free regime. This Chapter defines the boundaries that allow to consider an EM (drive) "safe" from the PDs point of view (i.e. no PDs inception). The analysis does not go in depth in the physics of PDs phenomenology, as this work is not focused on material/dielectric science, and several papers/theses have been published on the topic. However, some basic PD theory and models, necessary for supporting the discussion, are introduced and analysed. These, despite being simplified models, have been adopted for decades in high voltage engineering, and they are accurate enough from an electrical machines designer point of view and for the purpose of this work.

6.1 Problem Statement

Low voltage (i.e. <1000 V) EMs conventionally adopt organic insulating materials (i.e. Type I [32]). PDs are extremely harmful to such kind of insulation. Indeed, once they are incepted, polymeric bonds can be broken with consequent total dielectric breakdown within short time. This might be days/weeks/months depending on the frequency, amplitude and other parameters of the stressing voltage (electric field). It is therefore clear that when a low voltage EM is subject to PDs, these can cause a very rapid degradation leading to a fast "out of service" status. PDs in Type I

insulation are not identified as an intrinsic aging factor, but their inception generally represents the EM's end of life [131]. Thus, PD inception should be avoided at any cost, particularly in safety-critical EMs. However, a PD-free design generally comes with a compromise, that is, the overall drive performance might be subject to "de-rating" to guarantee reliable operation.

EMs designers and manufacturers started to face this problem (i.e. PDs in low voltage EMs) after the introduction and widespread of VSDs adopting solid state PECs. The application of fast switching devices, in PECs, causes a non-negligible voltage enhancement, even in the interturn insulation. This problem is further amplified when wide-bandgap MOSFETs are adopted (i.e. SiC and GaN). The aim of this Chapter is then to investigate how various design choices aimed at a PD-free insulation system, can affect the performance of low voltage EMs.

6.2 Power Electronics and Electrical Machines Insulation

In VSDs, the voltage amplitude seen at the EM terminals can be considerably higher than the one at the inverter side due to waveform reflections. The voltage enhancement is contingent on impedance mismatches between converter, connecting cable (i.e. feeder) and machine. Transient over-voltages occurring in VSDs can be studied relying on basic transmission lines theory. For an accurate description of these phenomena, it is required to have a precise knowledge of the motor and cable equivalent impedances, as a response to high frequency impulses (i.e. surge impedance). However, it has been widely demonstrated in literature [22, 84, 143, 144] and in technical standards [32] that simplified lumped parameter circuital models can precisely estimate the magnitude of the voltage amplification.

By defining the incident wave e_i (i.e. converter side), the resulting voltage at the end of the cable e_m (i.e. machine side) can be calculated as in (6.1), where Z_M is the EM (surge) impedance and Z_C is the cable characteristic surge impedance [145]. In transmission lines theory, the characteristic surge impedance is the ratio between

voltage and current of a single propagating wave without reflections, and depends on the cable properties (i.e. capacitance and inductance per unit length).

$$e_m = \frac{2 \cdot Z_M}{Z_M + Z_C} \cdot e_i \tag{6.1}$$

The maximum voltage amplification (i.e. worst-case) is achieved when $Z_M >> Z_C$ (i.e. approaching an open-circuit line). In this case the voltage is amplified by a factor of 2. Such scenario is not far from reality, as the surge impedance of an EM is generally more than one order of magnitude larger than the cable's one, and it is actually inversely proportional to the EM's rated power [84].

The voltage wave travels along the cable with a speed equal to the speed of light c (i.e. $\approx 3 \cdot 10^8$ m/s) multiplied by the velocity factor VF (<1). The latter can be calculated as in (6.2), where μ_r and ε_r are the cable relative permeability and dielectric constant respectively.

$$VF = \frac{1}{\sqrt{\mu_r \cdot \varepsilon_r}} \tag{6.2}$$

The dielectric constant of a typical three-conductor PVC cable can be assumed equal to 4.5, whilst it is reasonable to fix $\mu_r=1$ [22, 143]. Therefore, the voltage wave travels along the cable at a speed equal to 0.5c (i.e. $1.5 \cdot 10^8$ m/s).

The equivalent circuit of PEC, cable and EM has been implemented in the circuit simulation software LTspice® as shown in Figure 6.1.a. An example of simulation outcome is reported in Figure 6.1.b for a waveform rise time t_r=50 ns and a cable length of 5 m.

The TS IEC 60034-18-41 [32] lists the overvoltage factor *OF* (i.e. ratio between peak voltage at EM and PEC terminals) as a function of the cable length for different rise times ranging from 50 ns to 1 μs. Nonetheless, recent SiC MOSFETs devices feature rise times below 50 ns [146, 147]. Therefore, relying on the equivalent circuit reported in Figure 6.1.a, the *OF* is determined for several cable lengths ranging from 0.1 up to 5.5 m and four rise time values, i.e. 10, 20, 30 and 50 ns. The simulations

outcomes are summarized in Figure 6.2. As expected, for a given cable length, the faster (shorter) is the rise time, the larger is the *OF*.

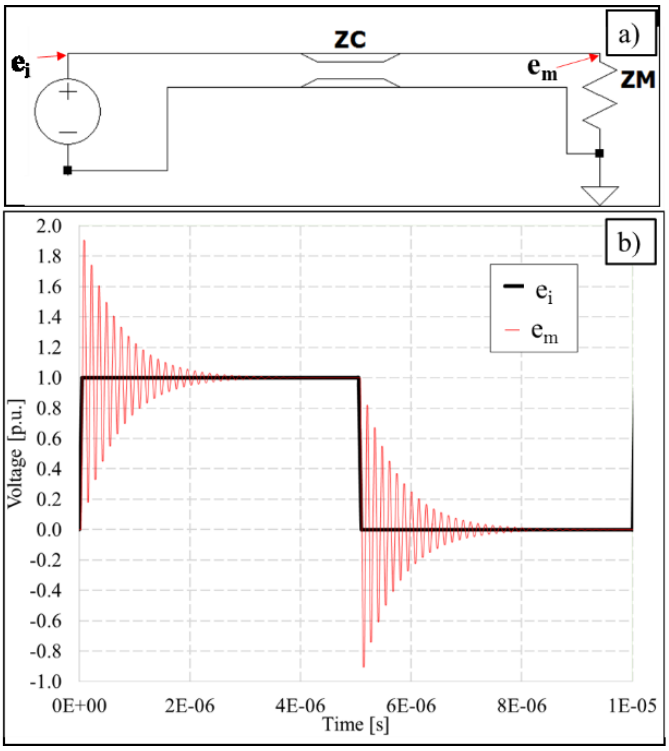

Figure 6.1 – (a) Simplified circuit representation of PEC, cable and EM implemented in LTspice® and (b) simulation outcome for t_r=50 ns and 5 m cable length.

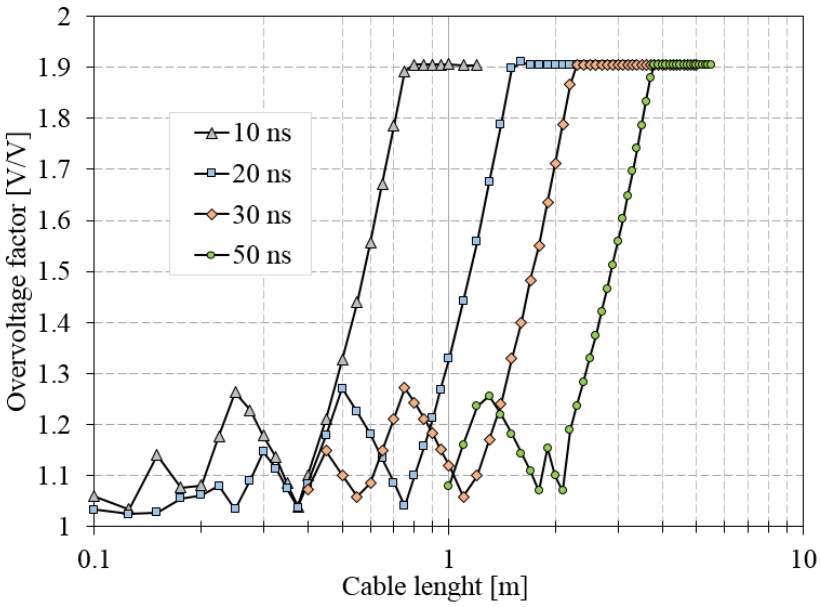

Figure 6.2 – Overvoltage factor vs. cable length for different rise times (10, 20, 30 and 50 ns).

The peak to peak, phase to phase voltage, $V_{p\text{-}p}$, appearing at the terminals of an EM fed by a 2-level converter can be calculated as in (6.3), where V_{DC} is the DC link voltage (voltage drops are neglected because of their modest influence).

$$V_{p-p} = 2(V_{DC} + OF) \tag{6.3}$$

Therefore, the voltage stressing the phase to phase insulation, for a star connected EM, is equal to $V_{p\text{-}p}$. The voltage across the phase to ground insulation, $V_{ph\text{-}g}$ is a fraction of the phase to phase voltage, and is conservatively calculated as in (6.4) [32]. It might, in practice, differ from this value (i.e. 70% $V_{p\text{-}p}$) based on the EM's neutral point voltage.

$$V_{ph-g} = 0.7 \cdot V_{p-p} \tag{6.4}$$

The voltage stressing the turn to turn insulation, $V_{t\text{-}t}$, is closely related to the rise time of the applied voltage waveform through (6.5), where $K(t_r)$ is a coefficient whose value is <1.

$$V_{t-t} = 0.7 \cdot K(t_r) \cdot V_{DC} \cdot OF \tag{6.5}$$

In the worst-case scenario, i.e. short rise time, $K(t_r)$ is ≈ 1. Indeed, in this case, the voltage drop across two adjacent turns approaches the peak value of the phase to ground voltage. In fact, due to waveform propagation delay within the winding, when the steep-fronted voltage appears at the first turn(s), the voltage potential of the adjacent turns might still be equal to zero. Such phenomenon is graphically illustrated in Figure 6.3.

An insulation system in a Type-I EM can be defined as PD-free when the repetitive PDIV (RPDIV) is above the three afore mentioned voltage levels, multiplied by an enhancement factor *EF*. The RPDIV is the minimum peak to peak impulse voltage at which more than five PD pulses occur on ten voltage impulses of same polarity.

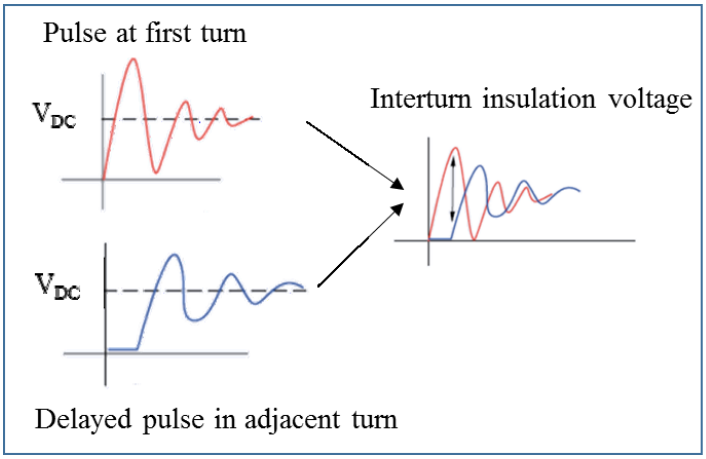

Figure 6.3 – Turn to turn voltage and propagation delay for short rise time PECs.

Various recent publications have argued on the validity/ambiguity of the RPDIV for qualification purposes [148, 149]. However, its definition still holds in technical standards. The *EF* ranges from 1.25 to 1.63 for both $V_{p\text{-}p}$ and $V_{t\text{-}t}$, whereas the interval 1.25 – 1.38 is advised for $V_{ph\text{-}g}$. Three inequalities can be thus introduced, and must be satisfied for guaranteeing PD-free operations in the corresponding insulation sub-system. These are expressed by (6.6), (6.7) and (6.8) for turn to turn, phase to ground and phase to phase insulation sub-systems respectively.

$$(R)PDIV_{t-t} > V_{t-t} \cdot EF \tag{6.6}$$

$$(R)PDIV_{ph-g} > V_{ph-g} \cdot EF \tag{6.7}$$

$$(R)PDIV_{p-p} > V_{p-p} \cdot EF \tag{6.8}$$

6.3 Insulation Sub-Systems Analysis

This Section examines under which conditions the three insulation sub-systems of a low voltage EM can be subject to PD activity. The analysis is carried out relying on the Paschen's law for air. In particular, the curve shown in Figure 2.1, which was experimentally proven by Dakin in 1977 [63], is adopted. The latter shows the breakdown voltage trend as a function of the pressure - electrodes spacing product.

Essentially, when the voltage applied between two electrodes in air is above (i.e. larger than) the breakdown voltage, an electrical arc/spark is incepted. In [63], the validity of the Paschen's law was proven for various electrodes shapes (e.g. cylindrical, planar), materials (i.e. bare metal or coated with an insulation) and applied waveforms (i.e. sinusoidal and impulsive).

6.3.1 Premise on the Paschen's law

The Paschen's law is accurate when modelling stationary (or quasi-stationary), uniform fields and thus it might provide imprecise results if applied to impulsive/PWM regime [89, 150]. However, it must be also pointed out that it predicts accurately the PDIV under sinusoidal regime, and the later (i.e. PDIV under sinusoidal waveform) is generally lower than the impulsive (R)PDIV [148], resulting in a conservative evaluation.

In the Author's opinion, it is not worth the effort to precisely estimate the (R)PDIV to within a few percent of mismatch, if later, when qualifying the insulation system, enhancement factors (ranging from 125 to ≈200%) are adopted according to technical standards [32]. In other words, even if one can predict the precise (R)PDIV value with no error at all, this voltage should be afterwards multiplied by a factor of two that accounts for a) thermal aging, b) EM operating temperature, c) mismatches between PDIV and PDEV. Apart for point c), whose modelling is not trivial at all, in this work, it has been clearly demonstrated how the accurate evaluation of a) and b) can be precisely carried out. Thus, from an EM design perspective, it would make more sense to act on shrinking the EF range rather than striving in modelling something of purely stochastic nature (i.e. (R)PDIV under impulsive regime). To make matters worse, the RPIDV shows a large dependence on the PWM waveform shape (i.e. rise time, pulse width, pulse polarity, etc.), thus making impossible to implement a universal tool to be used during the preliminary design of an EM. Indeed, at this stage, the EM designer can only speculate on the kind of waveform that will appear across the insulation system. The real waveform will be only available after the first EM prototype is built, connected to its PEC, and run in real operating environment.

That said, it should now be clear why in this work it has been preferred to adopt a more conventional (and conservative) approach in modelling the inception of PD in air. This choice is further strengthened and supported by technical standards which allow the use sinusoidal test voltage for insulation qualification purposes, even for PWM-fed EMs [32].

6.3.2 Turn to Turn Insulation

The turn to turn insulation in low voltage EMs is provided by the magnet wire enamel plus, eventually, the addition of impregnating resin. The enamel generally features an organic chemical composition (e.g. polyamide, polyimide, polyester etc.) and its thickness depends on the wire diameter and grade (GR). In the technical standard IEC 600317-0-1 [151], three distinct grades (i.e. GR1, GR2 and GR3) are counted for every conductor diameter and a higher GR corresponds to a thicker enamel layer. High quality impregnation techniques, such as vacuum pressure impregnation (VPI), can reduce the risk of PDs inception, since the majority of the gaps between wires are filled. Nevertheless, the standard procedure for measuring the interturn PDIV is based on the adoption of non-impregnated twisted pairs samples. Such approach, which accounts for the worst-case scenario (i.e. air-filled space between adjacent wires), is chosen in the present work.

The electric field distribution between adjacent turns is evaluated via FE, using the software ANSYS® Maxwell. A custom designed script is used for a) drawing the geometry, b) setting the boundary conditions and c) performing the simulations. The use of a script allows to quickly simulate various configurations of wire diameter, GR and materials. The PDIV is obtained via the analytical post-processing of the FE electric field distribution results. The model developed for the turn to turn insulation analysis is depicted in Figure 6.4, where d is the gap distance between wires, V_{peak} is the applied peak voltage, while D_{in} and D_{out} are the bare copper and the insulated wire diameters respectively. The enamel's relative permeability ε_e can be set in the script according to the simulated material.

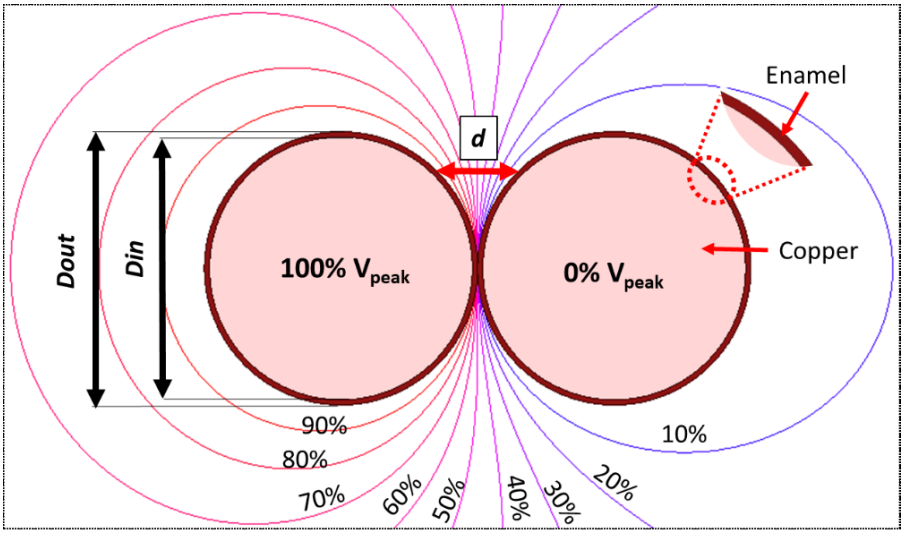

Figure 6.4 – Model employed for the turn to turn insulation analysis.

An example of a simulated electric field distribution map is shown in Figure 6.5, where a 0.4 mm magnet wire with GR1 insulation is excited with a turn to turn peak voltage of 740 V. By plotting the electric field corresponding to V_{peak}=740 V against the wires-gap distance and comparing the obtained field distribution line with the Paschen's curve, it is possible to note that the electric field magnitude exceeds the Paschen's limit, within the distance range of 4.9 – 61 µm, as illustrated in Figure 6.6. This indicates that if such voltage level (i.e. 740 V) were to appear between two adjacent turns, then there would be a high risk of PD inception. Keeping the same combination of wire diameter and grade, the maximum peak voltage, which enables PD-free operations (for the turn to turn insulation), is identified and the corresponding electric field distribution line is shown in Figure 6.6. This voltage level can be interpreted as PDIV, which for the considered case is equal to V_{peak}=520 V. The same analysis will be repeated for various wire configurations in Section 6.4, where the FE-Paschen's model will be also experimentally validated.

It is important to remark that the proposed model, which accounts for two wires in direct contact, represents a worst-case, but still realistic, scenario. In high performance EMs, the slot area needs to be exploited at its best by maximising the fill factor, leading to a high number of turns (i.e. wires) in direct contact.

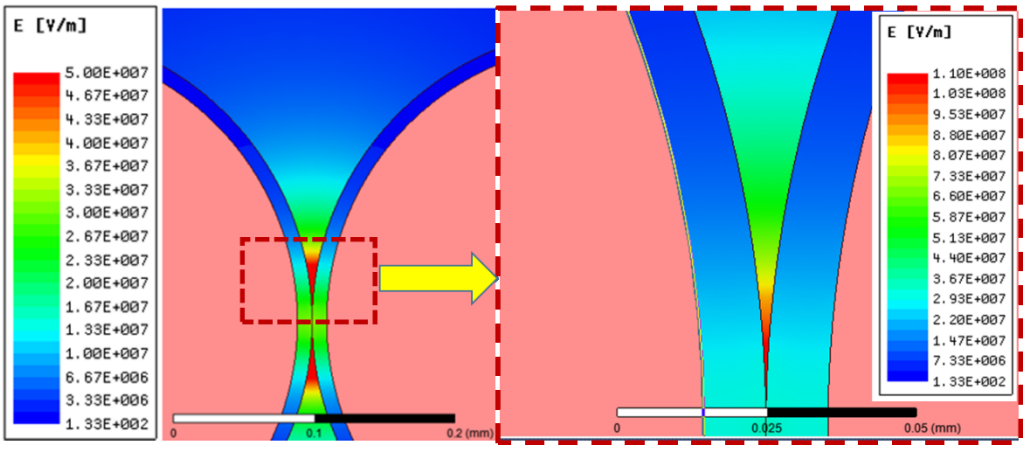

Figure 6.5 – Turn to turn electrostatic FE simulation at V_{peak}=740 V, using a magnet wire with 0.4 mm diameter and GR1 insulation.

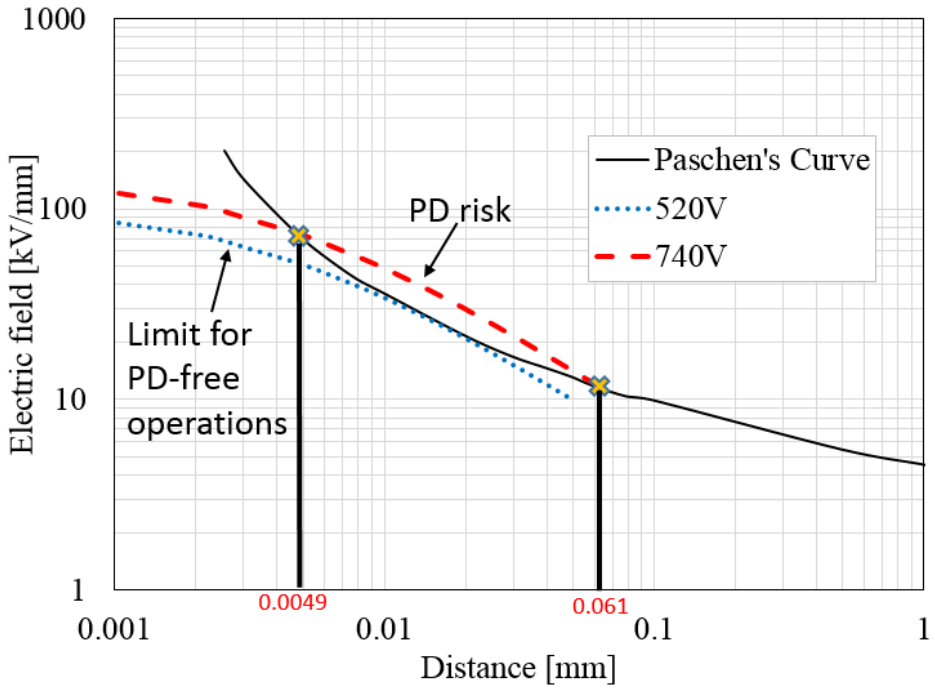

Figure 6.6 – Turn to turn electric field distribution along the wire enamel surface for 1) V_{peak}=740 V and 2) V_{peak}=520 V.

6.3.3 Phase to Phase Insulation

The phase to phase insulation subsystem in a low voltage EM generally comprises the magnet wire enamel plus an additional layer of organic insulation paper (e.g. Nomex®). The proposed model for analysing the PDIV in the phase to phase

insulation subsystem is shown in Figure 6.7. Two wires, belonging to as many different phases, are divided by an insulation paper separator. A preliminary FE electrostatic sensitivity analysis is performed to establish the relative position between the wires, which leads to the worst condition in terms of electric field magnitude in air. As a result, it is found that a displacement of $D_{out}/2$ along the y-axis direction gives the maximum electric field magnitude in the wedge-shaped gaps (i.e. between the wires and the separator). The same approach used for the turn to turn insulation case is adopted for extrapolating the PDIV. That is, plotting the electric field magnitude distribution against the gap distance, and verifying whether or not it is tangent to the Paschen's curve. An example of phase to phase PDIV prediction is reported in Section 6.4, where the model is verified against experimental measurements.

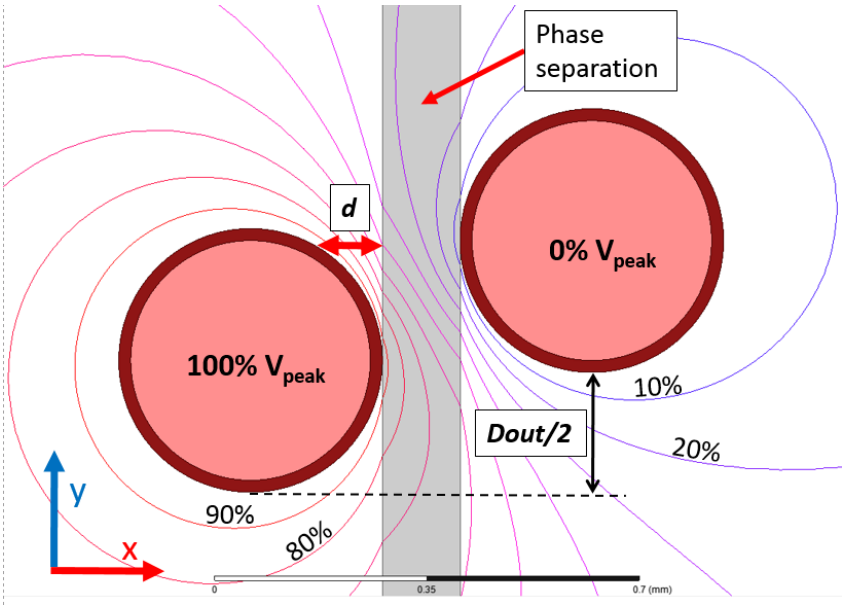

Figure 6.7 – Model employed for the phase to phase insulation analysis.

6.3.4 Phase to Ground Insulation

The phase to ground insulation subsystem is finally assessed using the model illustrated in Figure 6.8. In this case, the galvanic separation between wire's copper core and ground (i.e. stator core) is provided by the wire's enamel plus the addition of the slot liner (i.e. insulating paper) whose thickness is t_{liner}. The PDIV prediction is

carried out as for the turn to turn and phase to phase insulation subsystems, and the model validation is provided in Section 6.4.

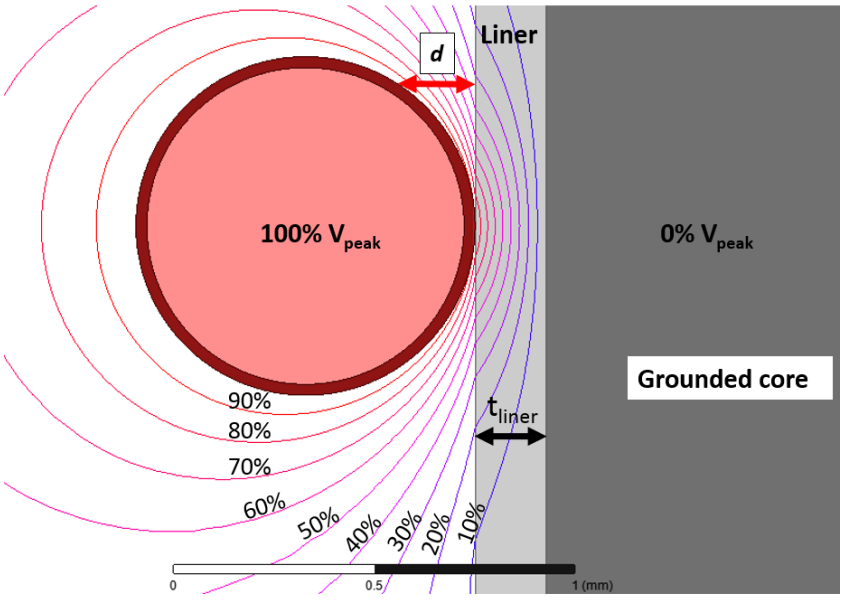

Figure 6.8 – Model employed for the phase to ground insulation analysis.

6.4 Experimental Validation

The three proposed models are verified against experimental measurements of PDIV. The validity of the indirect method, based on the dielectric dissipation factor, for PD measurement in low voltage EMs insulation is also experimentally proven. For what concerns the turn to turn insulation, which is the most critical in a low voltage EM, various combinations of wire diameter and grade are tested, whilst for the two remaining insulation subsystem a single configuration will be experimentally assessed.

6.4.1 Indirect PDIV Measurement in Low Voltage EMs

6.4.1.1 Theory

An ideal insulating material behaves as a lossless capacitor; hence, if a sinusoidal voltage is applied across the insulation, the resulting current leads the voltage

by an angle of 90° (i.e. purely capacitive current). On the other hand, real insulating materials exhibit dielectric losses. Thus, when they are subjected to a sinusoidal voltage, the ensuing current leads the voltage by an angle that is equal to 90 minus δ, where δ is defined as the dielectric loss angle [152, 153].

Assuming a sinusoidal excitation, the non-ideal dielectric is characterised by a complex relative permittivity ε_r^*, described as in (6.9), where ε_r' is the relative permittivity (i.e. real part), which is related to the energy stored inside the insulating material, while ε_r'' (i.e. imaginary part) is the relative loss index, also known as the loss factor, since it is associated with the energy dissipated within the insulating material [153].

$$\varepsilon_r^* = \varepsilon_r' - j\varepsilon_r'' \tag{6.9}$$

The stored energy is an indicator of the material property to be polarised due to the electric field. Both ε_r' and ε_r'' are frequency-dependent through a number of intricate dielectric relaxation and polarization phenomena [154]. All the measurements presented hereafter will refer to 50 Hz frequency.

As shown in Figure 6.9.a, a non-ideal insulation is schematically modelled by an ideal capacitor in parallel to a resistor accounting for the dielectric losses. When this circuit is excited through a sinusoidal voltage, the ensuing vector diagram is similar to the one shown in Figure 6.9.b. The dielectric dissipation factor is defined as the tangent of the dielectric loss angle δ (i.e. tanδ). Hence, it can be calculated as the ratio between the resistive current I_R and the capacitive current I_C, or as the ratio between the imaginary and real parts of the complex relative permittivity. Both these expressions are given by (6.10).

$$tan\delta = \frac{I_R}{I_C} = \frac{\varepsilon_r''}{\varepsilon_r'} \tag{6.10}$$

Further, the dielectric loss is the sum of solid losses (i.e. conduction and polarization losses) and ionization losses (i.e. losses due to the inception of PDs) [152, 155],

therefore for small values of δ, tanδ is determined by (6.11), where $tan\delta_S$ is the term accounting for solid losses, whilst $tan\delta_{PD}$ is the ionization loss term.

$$tan\delta = tan\delta_S + tan\delta_{PD} \tag{6.11}$$

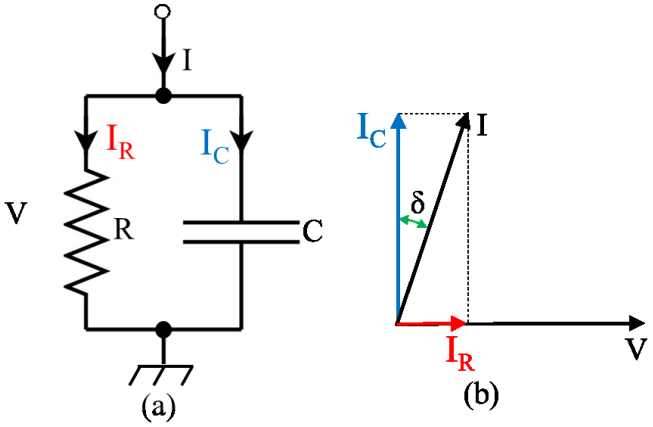

Figure 6.9. Non-ideal insulating material model. a) Circuit schematic, b) Vector diagram.

By applying a potential difference across two electrodes, separated by a solid insulating material, an electric field occurs within the dielectric. If the dielectric is characterised by air inclusions (i.e. voids), and the electric magnitude is below the dielectric strength of air, the ionization process will not arise. As long as the insulation's voids are not ionised, the tanδ value will only be dependent on the solid loss term [156]. Under this condition, the measured tanδ is only slightly influenced by the excitation voltage used during the measurement [155-157]. When the excitation voltage is increased and the developed electric field is such that voids begin to become ionised (i.e. PDs are incepted), the term $tan\delta_{PD}$ will steeply rise along with the excitation voltage, as illustrated in Figure 6.10 [152]. Thus, the voltage level at which the tanδ starts to steeply rise represents the PDIV. Therefore, the dissipation factor test can be used as an indirect PD measurement method. In medium and high voltage EMs, such method is widely employed for assessing the status of the phase to phase and phase to ground insulation, whilst it is practically ignored for low voltage EMs. What follows aims in experimentally proving that the dielectric dissipation factor is a suitable method for PDs detection in materials and insulation systems employed in low voltage EMs.

This is done by apprising the experimental results obtained by both direct (i.e. PD detector) and indirect (i.e. tanδ) methods.

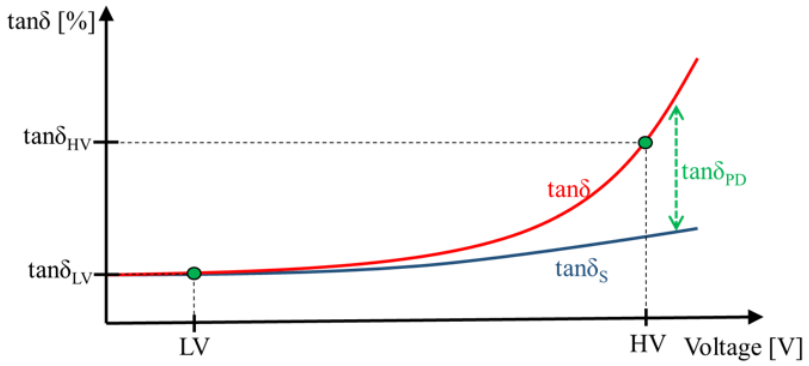

Figure 6.10. Test voltage influence on the tanδ measurement.

6.4.1.2 Validation

The direct PD measurements are carried-out using a commercial PD detector Techimp® PD-Base II coupled with a transverse electromagnetic antenna (TEM), whilst a Megger® delta 4000 is used for the dissipation factor test. For comparing the two PD measurement methods, the three insulation sub-systems commonly found in low voltage EMs are analysed. In particular, the measurements concerning the phase to ground and phase to phase insulation are executed on a 3 phase, 0.75 kW industrial induction motor which is shown in Figure 6.11, whilst the turn to turn insulation is investigated using a population of 10 random wound coils similar to those reported in Figure 4.1.

The experimental results regarding the phase to ground and phase to phase insulation are summarized in Figure 6.12 and Figure 6.13 respectively, where the data relative to the three EM's phases are collected. The measurements were all performed with the same environmental condition, that is 23 °C and 45% relative humidity. For both insulation sub-systems it is possible to note a fair agreement between direct and indirect PDIV measurement methods. In particular, PDs are incepted when the tanδ's trend features a point of discontinuity and starts to steeply rise. This behaviour is less pronounced for the phase to phase insulation, as, in this case, it is possible to note a

larger contribution provided by solid losses (i.e. $\tan\delta_S$). With good probability, this represents a reason why the tanδ method is not popular for the assessment of complete low voltage EMs, where other PD detection techniques can have a higher sensitivity. The sensitivity and precision of the tanδ method for PD detection improves drastically when non-impregnated samples are assessed, as will be shown in Sections 6.4.2, 6.4.3 and 6.4.4.

The data relative to the turn to turn PDIV measurements are shown in Figure 6.14. In this case, being the data collected on a family of 10 specimens, the median and standard deviation are reported for the tanδ measurements, whilst the Weibull probability density function is shown for the directly-measured PDIV values. For this insulation sub-system the matching between the two measurement methods is more marked. This is mainly because there is an imperceptible solid loss contribution, hence, the tanδ trend's discontinuity is easily observable.

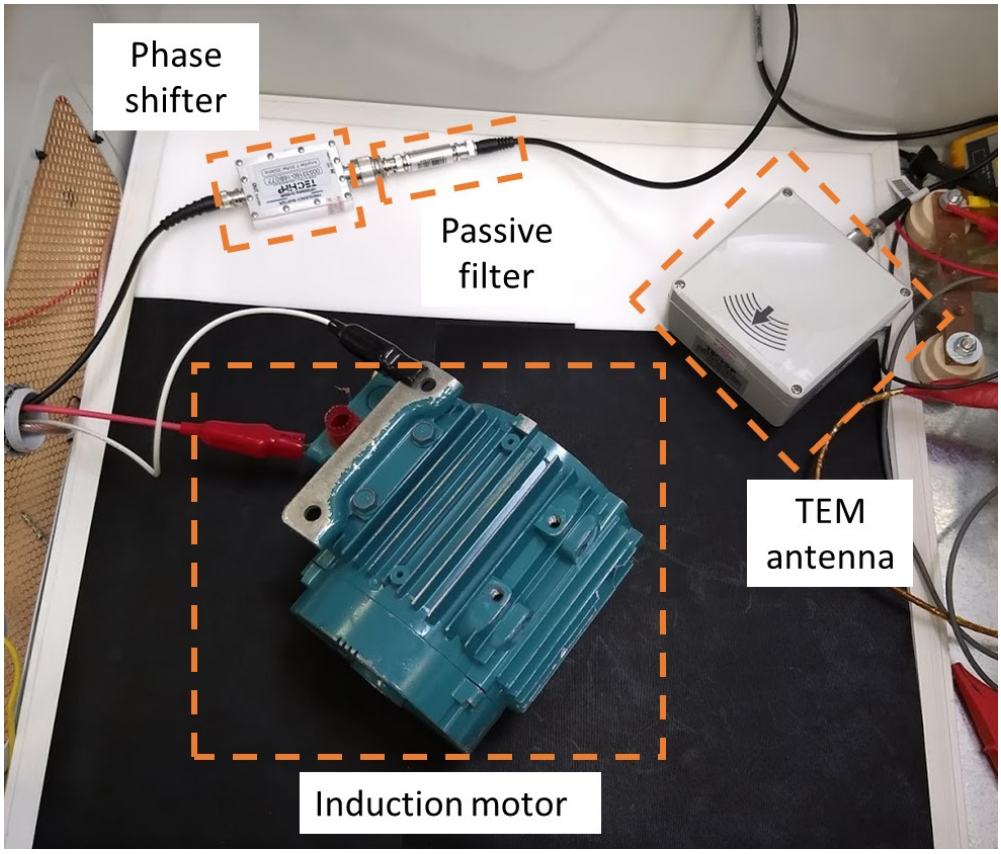

Figure 6.11. Direct PDIV detection on an industrial induction motor.

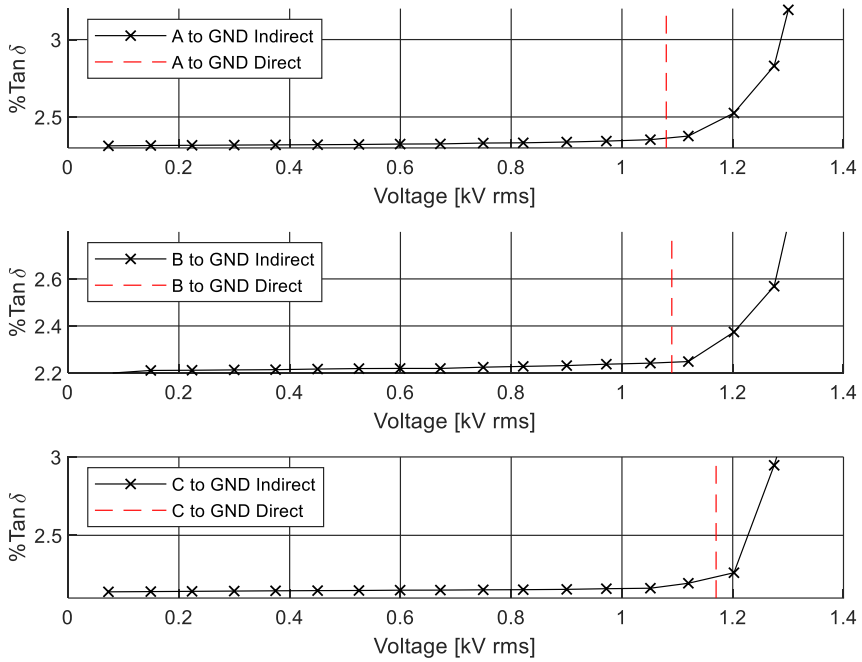

Figure 6.12. Direct vs. indirect PDIV measurement on phase to ground insulation.

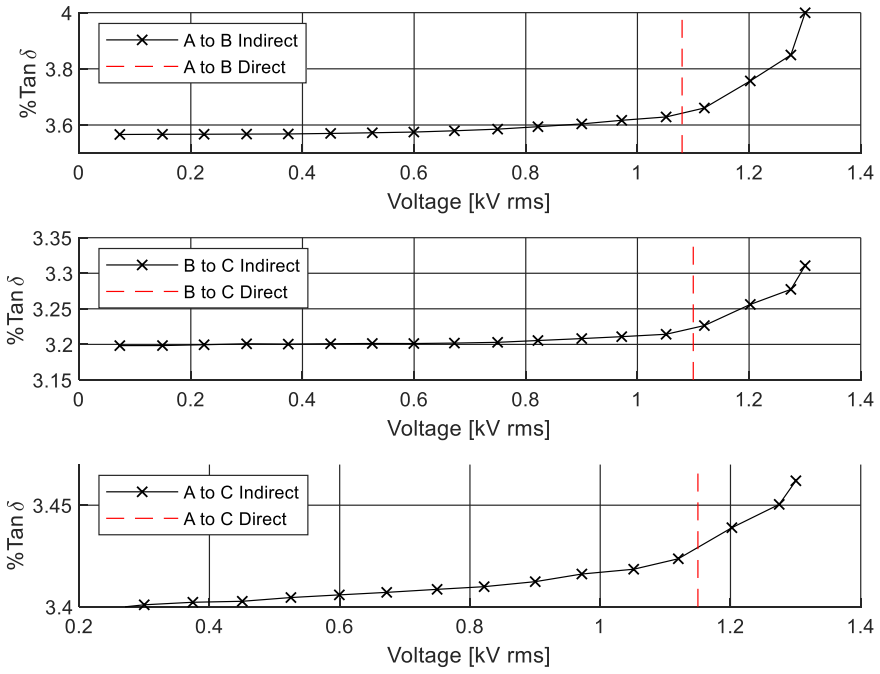

Figure 6.13. Direct vs. indirect PDIV measurement on phase to phase insulation.

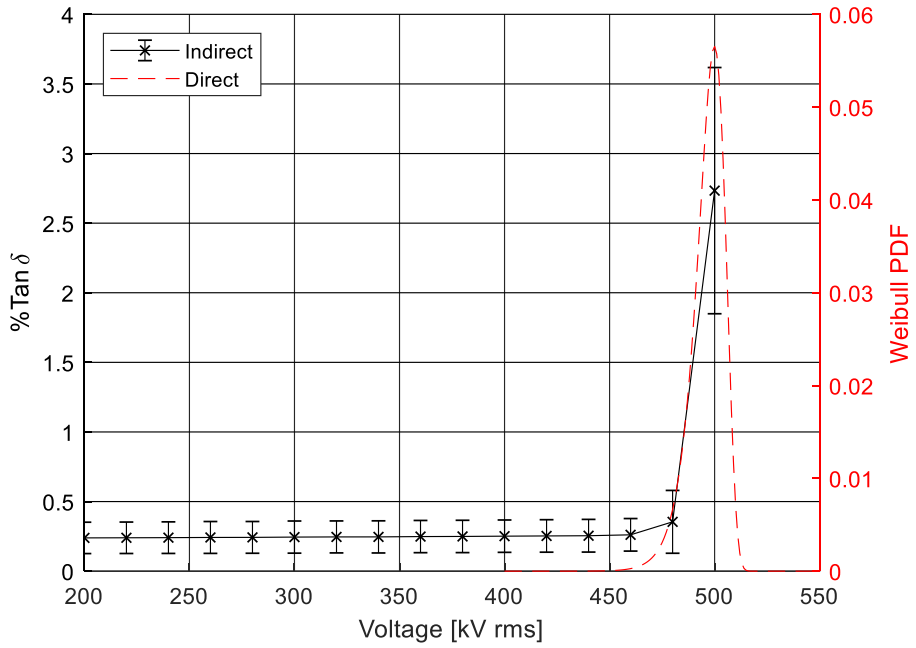

Figure 6.14. Direct vs. indirect PDIV measurement on turn to turn insulation.

In summary, the presented data clearly demonstrate that the tanδ is a suitable and convenient method for PD measurement in low voltage EMs insulation. Contrarily to the direct measurement through a PD detector, for the dissipation factor test an external power supply is not required for exciting the specimens, as the latter is embedded in the testing equipment (i.e. Megger® delta 4000). Further details and additional test results, have been carried-out by this Author and are available in [158].

6.4.2 Turn to Turn PDIV Measurement

For the turn to turn insulation, the PDIV is measured through the direct method, using the commercial PD recorder/processer Techimp® PD-Base II and exciting the specimens via a high voltage power supply (GW-Instek). The test setup is shown in Figure 6.15. The specimens adopted for the experimental assessment are twisted pairs, manufactured according to the TS IEC 60172 [127]. The electromagnetic signals emitted by the PD inception are captured by the high frequency (up-to 2 GHz) TEM antenna. This signal is analogue-filtered and frequency-shifted before being fed to the

PD-Base II, which is connected to a personal computer, equipped with a Techimp® proprietary software for signal analysis and post-processing.

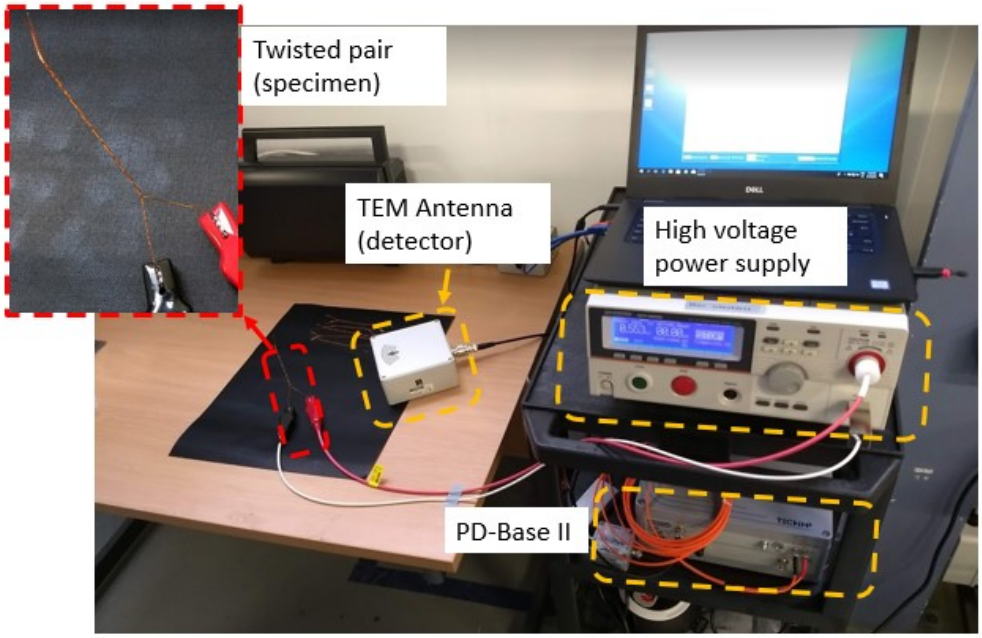

Figure 6.15 – Test setup for the direct measurement of turn to turn PDIV in twisted pairs.

The tested magnet wire configurations are listed in Table 6.1. Such measurement refers to a population of 5 specimens.

The magnet wire identifier reported in Table 6.1 embodies the (bare) wire diameter and GR (e.g. 071G1 identifies a wire whose bare diameter is 0.71 mm featuring a GR1 insulation). For the correct implementation of the FE-Paschen's model for PDIV prediction, it is necessary to measure the actual wire diameter d_{out} as well as the enamel relative permittivity ε_e. Indeed, magnet wire's manufacturers, as well as technical standards, only provide a range of acceptable enamel thicknesses for each GR. For example, in a GR2, 0.4 mm wire the outer diameter can range from 0.44 to 0.459 mm [151].

The wire diameter measurement is a straightforward process, since a simple micrometer is used for carrying out this task. The measured d_{out} (mean ± standard deviation) for each wire configuration are listed in Table 6.1. Such measurement refers to a population of 5 specimens. On the other hand, the ε_e is evaluated through an indirect

measurement. Namely, a wire piece is coated with conductive silver paint as schematised in Figure 6.16 and shown in Figure 6.17.

Table 6.1 – Analysed magnet wire configurations and measured diameter/permittivity.

Magnet wire identifier	D_{in} [mm]	D_{out} [mm]	ε_e
04G2_1	0.400	0.441±0.0005	4.01±0.18
04G2_2	0.400	0.452±0.0008	3.53±0.20
071G1	0.710	0.747±0.0024	2.73±0.24
071G2	0.710	0.773±0.0026	3.19±0.31
08G2	0.800	0.859±0.0007	3.36±0.11

Such specimen's layout can be seen as a cylindrical capacitor, whose capacitance can be calculated as in (6.12) where ε_0 is the vacuum permittivity.

$$C_{cyl} = \frac{2\pi\varepsilon_e\varepsilon_0}{\ln\left(\frac{0.5d_{out}}{0.5d_{in}}\right)} \tag{6.12}$$

Thus, once measured C_{cyl}, the enamels relative permittivity can be readily computed by rearranging (6.12) as in (6.13).

$$\varepsilon_e = \frac{C_{cyl}\ln\left(\frac{0.5d_{out}}{0.5d_{in}}\right)}{2\pi\varepsilon_0} \tag{6.13}$$

The capacitance C_{cyl} has been measured for all the considered wire configurations, adopting 5 specimens for each sample, and the resulting ε_e values are listed in Table 6.1.

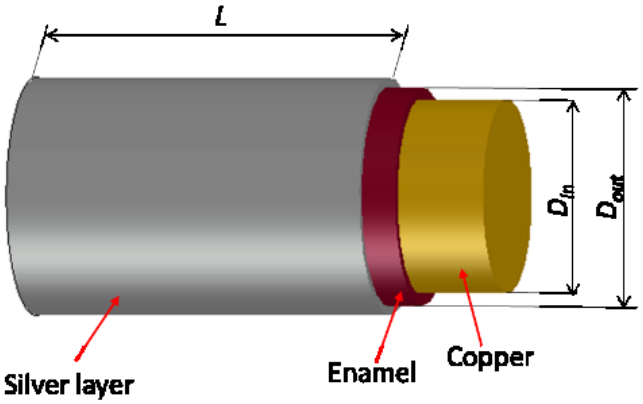

Figure 6.16 – Schematisation of magnet wire coated with a silver layer for capacitance measurement.

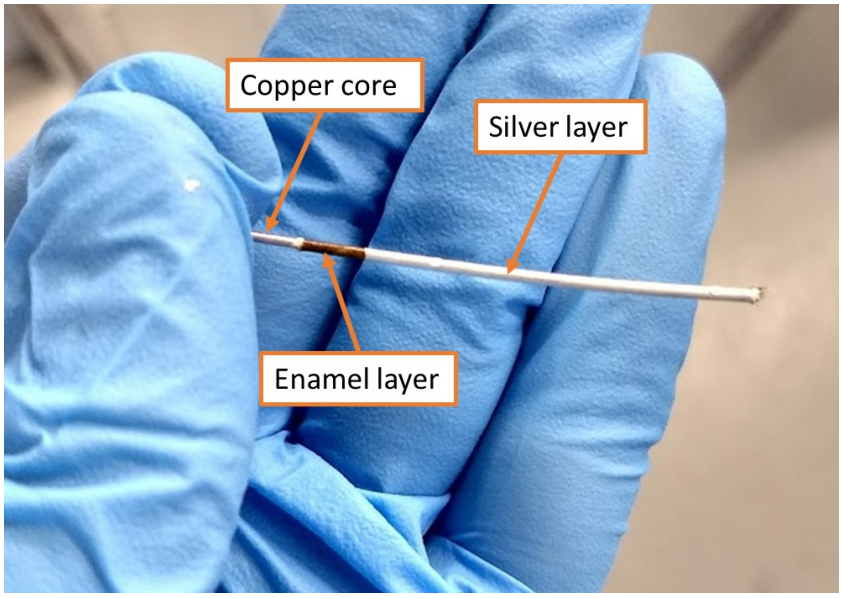

Figure 6.17 – Magnet wire coated with a silver layer for capacitance measurement.

At this point the PDIV can be predicted, for each wire configuration, adopting the model presented in Section 6.3.2. The results are listed in Table 6.2 where the experimentally measured PDIV(s) are also given. These are the mean value of the measured PDIV's Weibull distribution, computed over a sample of five specimens for each wire configuration. The measurements were carried out with an ambient temperature of 25 ± 3°C and relative humidity of 40 ± 10%, and the specimens were cleaned with ethylic alcohol before performing the measurements.

From the obtained results it is possible to note a fair agreement between the model-predicted and the experimental PDIV. It is also worthy noticing how the two 0.4 mm diameter magnet wires (i.e. 04G2_1 and 04G2_2), despite having the same grade, show a non-negligible PDIV mismatch. This result is mainly attributed to their difference in enamel thickness (i.e. wire's outer diameter).

Table 6.2 – Predicted vs measured turn to turn PDIV.

Magnet wire identifier	$PDIV_{pred}$ [V_{peak}]	$PDIV_{meas}$ [V_{peak}]	$\|err\ \%\|$
04G2_1	660	709	6.9 %
04G2_2	760	800	5 %
071G1	720	713	1 %
071G2	840	848	0.94 %
0.8G2	820	807	1.6 %

For the sake of completeness in some wire configurations it was also experimentally verified that the PDIV measured under sinusoidal voltage is lower than the RPDIV measured with PWM excitation. The specimens (i.e. twisted pairs) are connected to a GBS Elektronik® RUP6 pulse generator which allows to set amplitude, rise time, frequency, polarity and width of the applied PWM voltage pulses. The PD inception is again detected using the PD-Base II. In this case the specimens are inserted in a grounded Faraday cage for increasing the antenna's signal to noise ratio, as shown in Figure 6.18.

The features of the applied pulse waveforms are collected in Table 6.3, whilst the measured RPDIV (mean of the Weibull distribution) are reported in

Table 6.4 where the measured PDIV under sinusoidal voltage excitation are also listed. All the voltages in this table refer to the peak to peak value.

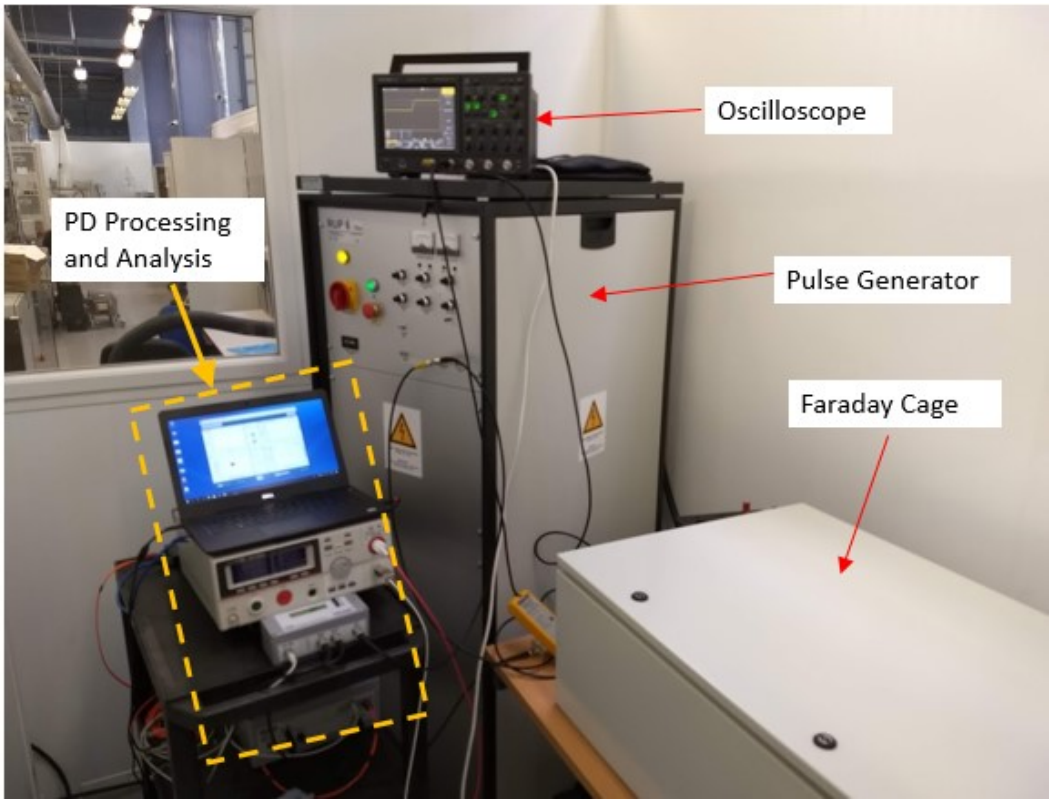

Figure 6.18 – Test setup for the measurement of RPDIV.

Table 6.3 – Characteristics of the PWM pulses used for RPDIV assessment.

Pulse identifier	*f* [kHz]	t_r [µs]	*Pulse width* (P_w) [µs]	*Polarity*
P#A	1	1.4	10	Unip+
P#B	1	1.4	10	Bip
P#C	1	0.3	6	Unip+

Table 6.4 – Measured (R)PDIV over a population of 5 specimens each (mean of the Weibull distribution).

Excitation voltage	*(R)PDIV* [$V_{peak-peak}$]	
	071G1	*071G2*
Sin (50 Hz)	1427	1698
P#A	1463	1614
P#B	1537	1805
P#C	1577	1760

For all the analysed configurations it is verified that the measured PDIV, with sinusoidal excitation voltage, is lower than the RPDIV under impulsive waveforms, except for the specimens 071G2 excited with the waveform P#A. In this case the recorded RPDIV is c.a. 5% lower than the sinusoidal case. However, it should be observed that such waveform has a relatively long rise time (i.e. 1.4 µs), which is unlikely to be observed in modern VSDs. In fact, the IEC 60034-18-41 indicates that the applied impulsive voltage waveform, for qualifying the turn to turn insulation subsystem, should have a rise time of 0.3 µs (i.e. P#C). For such case it is clear that the application of a sinusoidal voltage provides a conservative evaluation, as already mentioned.

6.4.3 Phase to Phase PDIV Measurement

The PDIV of the phase to phase insulation subsystem is measured through the indirect method, since it provides the exact same result as the direct PD measurement.

The specimen chosen for investigating the phase to phase PDIV consists of two random wound coils galvanically separated by a single sheet of Nomex® type 410 and mechanically clamped as shown in Figure 6.19. The wire adopted for the experiments is the one identified as 04G2_1 in Table 6.1, whilst the Nomex® separator features a

0.13 mm thickness. The tanδ measurement is carried out via a Megger® Delta 4000 which embeds the sinusoidal power supply as well as the dissipation factor tester.

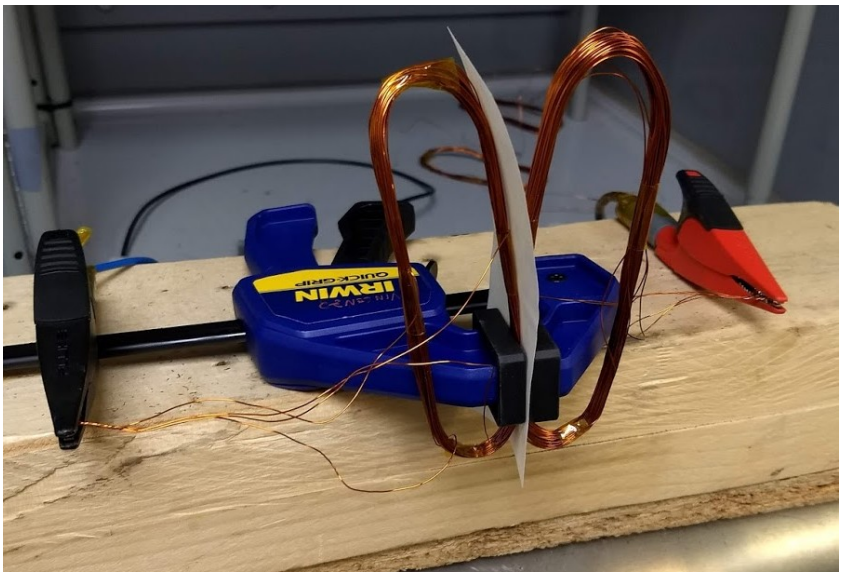

Figure 6.19 – Specimen adopted for the phase to phase PDIV measurement.

The obtained %tanδ trend vs. applied excitation voltage is reported in Figure 6.20. In this plot the mean %tanδ (red dot) and the standard deviation (blue lines) are shown, since 5 specimens are tested. It is possible to observe that the %tanδ steeply rises when the applied voltage is above 1.45 kV, indicating the inception of PDs.

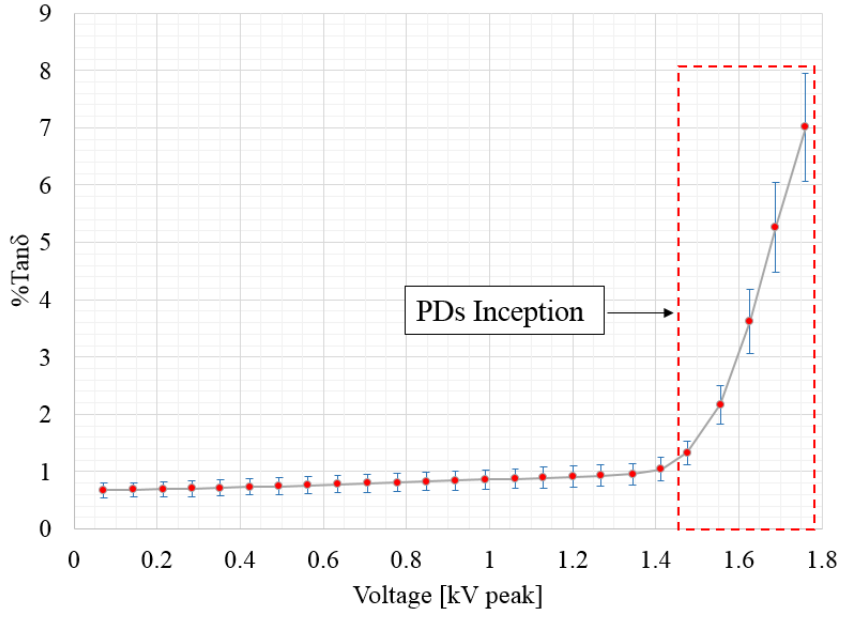

Figure 6.20 – Measured phase to phase dielectric dissipation factor vs. applied voltage.

By exploiting the model introduced in Section 6.3.3 the electric field distribution along the wire's enamel surface vs. the (wire-separator) gap distance is plotted alongside the Paschen's curve for air at sea level pressure in Figure 6.21. The predicted peak phase to phase PDIV is equal to 1.5 kV showing a fair agreement with the experimental result.

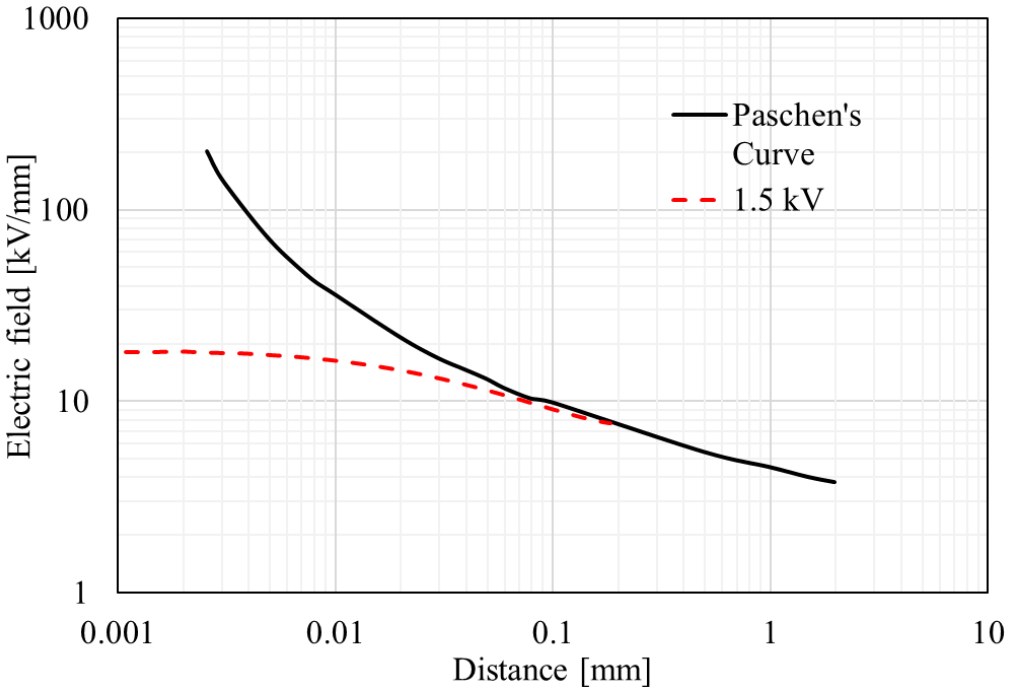

Figure 6.21 – Predicted phase to phase PDIV: electric field distribution vs. Paschen's curve.

6.4.4 Phase to Ground PDIV Measurement

For experimentally measuring the phase to ground PDIV, motorettes, similar to those shown in Figure 4.1, are used as specimen. As for the previous case, the adopted wire is the one identified as 04G2_1 in Table 6.1, whilst the slot liner is a single sheet of 0.13 mm Nomex® type 410 and the motorettes are not impregnated. The experimental setup is captured in Figure 6.22, where the Megger® Delta 4000, used for the indirect PDIV measurement, is also shown. The measured phase to ground %tanδ vs. applied voltage is reported in Figure 6.23, where it is possible to observe that PDs are incepted when the applied peak voltage is above 1.45 kV. In this case, the model proposed in Section 6.3.4 slightly under estimates the PDIV, since the predicted value

is 1.35 kV (i.e. 6.8% error). Nonetheless, it must be pointed out that in such a model, the adopted relative permittivity and thickness for the Nomex® paper are the ones provided by the manufacturer, which might slightly differ from the actual values. Further, the model assumes that the wire (coil) is in perfect contact with the slot liner, and the liner is in perfect contact with the core as can be seen in Figure 6.8.

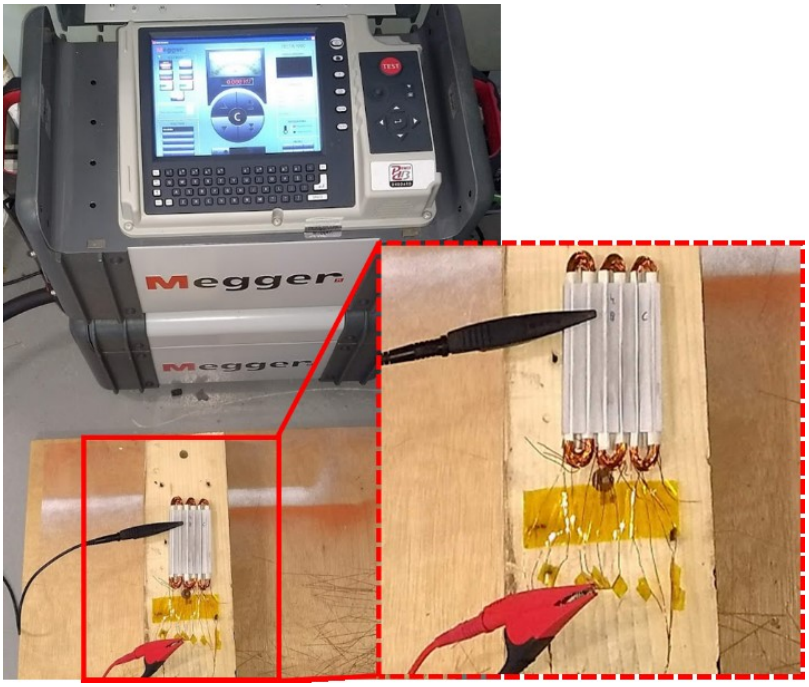

Figure 6.22 – Experimental setup for the indirect measurement of phase to ground PDIV.

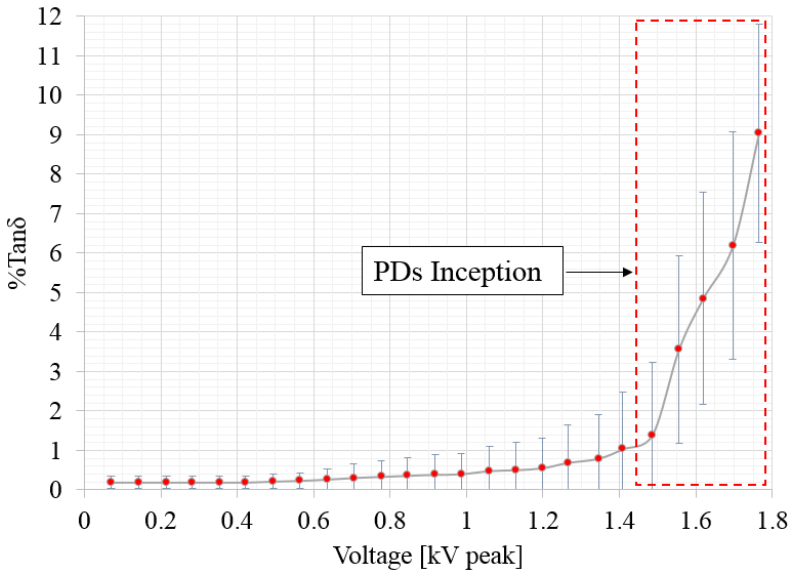

Figure 6.23 – Measured phase to ground dielectric dissipation factor vs. applied voltage.

In the following sub-section, the experimentally-validated PDIV prediction models will be adopted for the the design stage of a case-study, traction EM.

6.5 Case-Study: Rail Traction Motor

This Section shows an application example for the proposed models in the design of a traction EM. In particular, the model presented in Section 6.3.3, and validated in Section 6.4.1 will be used for predicting the turn to turn PDIV and evaluating how the insulation choice can strongly influence the torque-producing performance.

The analysed EM is a liquid cooled, 48 slot / 8 poles V-shaped PMSM co-designed by the Author for an industrial partner, whose cross-sectional view is illustrated in Figure 6.24. The main design parameters of the complete drive are listed in Table 6.5. Considering the application, the machine is designed for continuous duty operations.

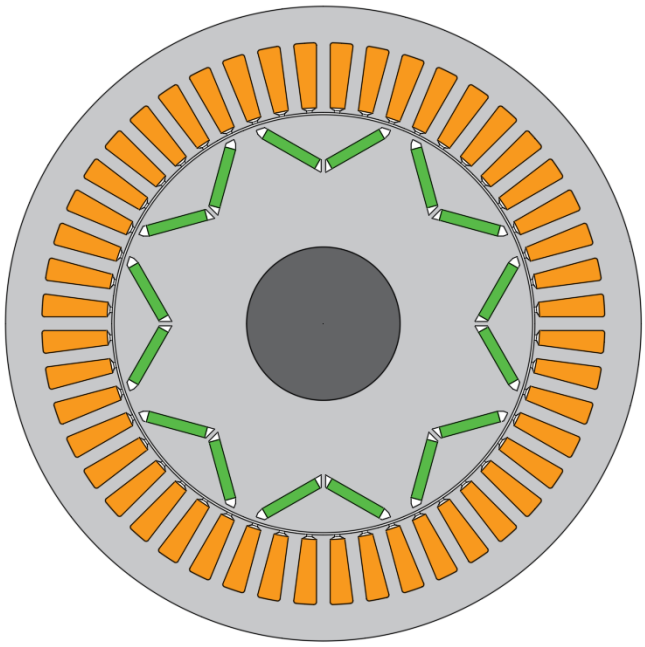

Figure 6.24 – Cross-sectional view of the case-study rail traction PMSM.

According to Figure 6.2, for a cable length of 2 m and a PWM rise time of 30 ns, the ensuing overvoltage factor OF is slightly above 1.7, and thus a value of 1.8 is

conservatively assumed. Fixing the enhancement factor EF equal to 1.63 [32], the minimum PDIV necessary for guaranteeing a PD-free design is calculated as reported in (6.5) and it is equal to 1110 V peak to peak. Therefore, the magnet wire insulation grade must be chosen so that its corresponding PDIV is above such value according to (6.6). The model introduced in Section 6.3.3 is employed for this purpose.

Table 6.5 – Parameters of the rail traction drive.

Design Parameter	Quantity	Unit
Base speed, n	2100	rpm
Pole pairs, p	4	-
Windings layout	Distr.	-
PM grade	N42UH	-
Cooling method	Indirect liquid	-
Outer diameter	290	mm
Axial length	200	mm
Phases	3	-
Turns per coil	12	-
Parallel paths	8	-
Max fill factor (wire), ff_W	50	%
PWM Rise time, t_r	30	ns
DC link voltage	540	V
Current density, J_{Max}	6.3	A/mm^2
Feeder (cable) length	2	m

The maximum current density for continuous operations J_{max} is equal to 6.3 A/mm^2, whereas the wire slot fill factor ff_w (i.e. slot fill factor considering the wire insulation) is constrained to 0.5 for manufacturing limitations. Therefore, the slot copper fill factor (i.e. ratio between copper and net slot surface area) will depend on the adopted magnet wire grade and liner thickness.

Deciding to implement a "design for manufacturability" approach, a 0.8 mm wire is selected for the winding. Indeed, using a thinner wire would require a number of parallel strands higher than 10 (with consequent manufacturability difficulties). Therefore, as J_{max} and ff_w are both constrained, the wire's GR will define the number of parallel strands per turn and the machine's phase current. In order to further underline how the insulation choice can strongly influence the PMSM (torque) performance, only two configurations are analysed, one being the riskier from the PD inception point of view, and the other being the safest. Hereinafter these are named as Configuration 'A', which features a 0.8 mm, GR1 wire and Configuration 'B' which adopts a GR3, 0.8

mm wire. The slot layout for both ‘A’ and ‘B’ configurations is obtained using the commercial software MotorCAD®, as illustrated in Figure 6.25. The thicker insulation employed by configuration ‘B’ reduces the number of conductors fitted in the slot, compared to configuration ‘A’ (i.e. 192 vs. 216). This also means that the copper fill factor is 44.2% for configuration ‘A’ and 34.9% for configuration ‘B’ (whilst the wire fill factor does not exceed 50% for both configurations).

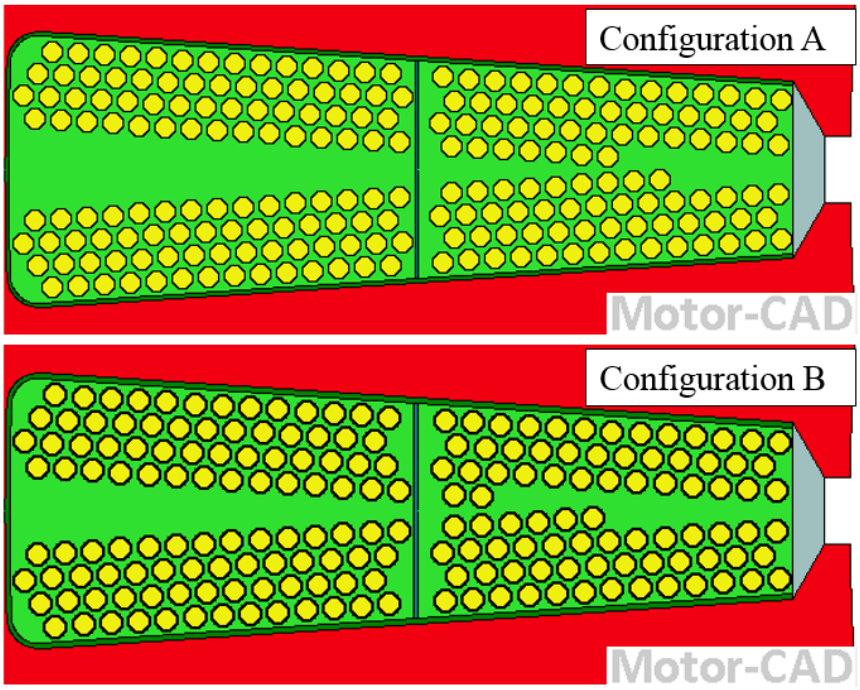

Figure 6.25 – Rail traction PMSM slot layout for the two analysed insulation configurations.

Electromagnetic FE simulations have been performed for both configurations using the commercial software ANSYS® Maxwell 2D. The resulting instantaneous torque plots are shown in Figure 6.26, while a performance summary is reported in Table 6.6.

Configuration ‘A’ develops 10.5 % higher continuous torque (at rated speed) than ‘B’. Nonetheless, the excellent torque density of ‘A’ comes with an enhanced risk of turn to turn PDs inception. In fact, adopting the FE-Paschen’s model introduced in Section 6.3.3, the predicted (turn to turn) peak to peak PDIV values are 1160 and 1760 V for configurations ‘A’ and ‘B’ respectively. Thus, the expected turn to turn voltage for configuration ‘A’ (i.e. 1100 V) is dangerously close to the minimum ‘safe’ PDIV,

necessary for guaranteeing PD-free operations, indicating that such a layout poses the whole drive at a high risk of electric failures. On the other hand, the insulation for configuration 'B' is surely over-engineered, since the predicted PDIV (i.e. 1760 V) is well above the PD-safe voltage. Therefore, a fair compromise between reliability and torque density performance is surely achieved by adopting a GR2 wire insulation, whose thickness is in-between the GR1 and GR3. A prototype of the EM shown in Figure 6.24, adopting such insulation grade, has been manufactured, and at the time of writing this Thesis is being electromechanically tested. Thus, by using the proposed model(s) it was possible to select the insulation layout which guarantees optimal electromagnetic performances without compromising on reliability. Such insulation layout choice was conveniently carried-out by simulations only. This remarkably speeds-up the design process, as, at this stage, there is no need for manufacturing motorettes / formettes for the PDIV measurement. The amount of saved time is even longer in cases where a larger number of insulation configurations/layouts need to be assessed for performing the trade-off studies.

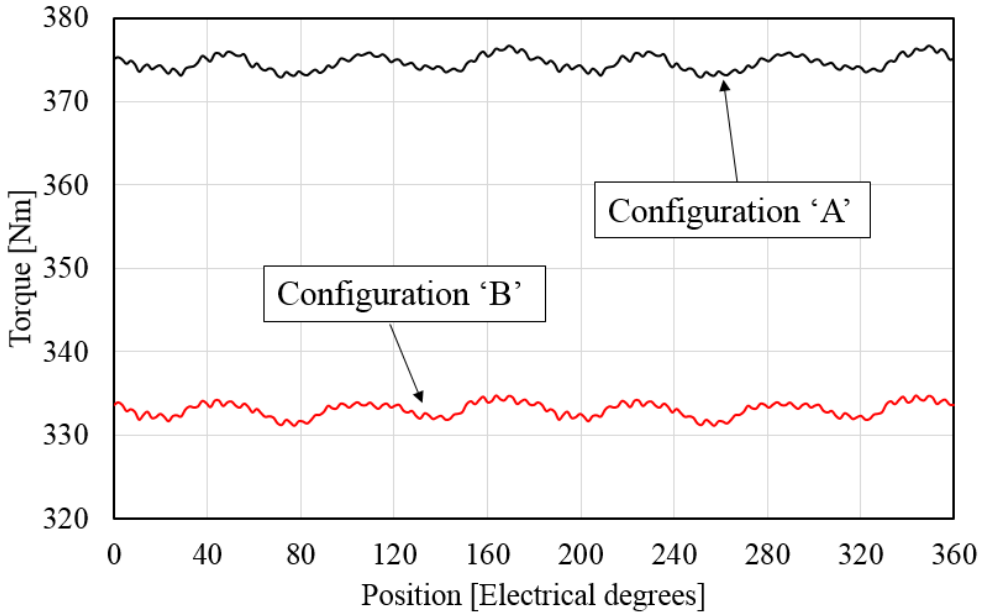

Figure 6.26 – Instantaneous torque plot for the two analysed configurations, obtained through FE.

Table 6.6 – Performances of the case-study traction PMSM according to the chosen insulation configuration.

PMSM conf.	Strands number	ff_C [%]	Phase current [Arms]	Average torque [Nm]
A	9	41.9	228	373.4
B	8	37.7	203	331.9

6.6 Concluding Remarks

In this Chapter the PD problem in low voltage EMs has been analysed. The strong impact that modern power converters can have on EMs reliability has been described using transmission lines theory and equivalent circuit simulations. Three models, one for each insulation subsystem of a typical EM, have been proposed and experimentally validated. The validity of the indirect PDIV measurement method for low voltage EMs insulation was also experimentally proven. The proposed models allow to quickly evaluate under which condition an EM insulation can be considered "safe" from the PD inception point of view. Despite not being the "ultimate" models for PDIV estimation (for these, there is a wide and growing specialised literature), they are however in line with the underlying message of this thesis, namely, the concept of reliability-oriented design aimed at reducing over-engineering and safety factors. These models can be conveniently and easily integrated in the design process of an EM, for performing e.g. trade-off and optimization analyses, given their easy implementation and fast computational time. This is demonstrated practically with the concluding case-study of this Chapter, in which it is verified how the insulation choice can strongly impact the performance of a traction PMSM.

This Chapter has resulted in the publication of 1 journal paper [158] and 2 conference papers [159, 160].

Chapter 7 Conclusions and Future Work

In this final Chapter the main conclusions of the Thesis work are drawn. A summary of the achieved objectives is provided. Some ideas for future work, to which this Author is already involved in, are also listed and briefly discussed.

7.1 Summary

This work represents a first attempt to bridging the gap that today exists among material scientists, insulation manufacturers and electrical machines designers. For the first time (to the Author's knowledge), concepts of reliability and physics of failure are fully integrated in the design process of electrical machines, and treated as a main design objective, on a par with e.g. power density, efficiency etc. This is achieved by the development of theoretical models, supported by experimental investigations that define and describe the insulation system as a design parameter. These models can easily be integrated and embedded into the design process of insulation for high performance, reliable EMs.

7.1.1 Thermal Analysis of Electrical Machines

As a pre-requisite for the correct insulation reliability assessment for electrical machines, some theory behind motors' thermal management and modelling techniques is introduced. The "technical part" of this Thesis thus starts with a Chapter providing an in-depth analysis into lumped parameter thermal networks for accurate temperature prediction purposes. The fulfilment of such task is crucial, since, in this work, the strong impact that temperature can have on a motor's insulation lifetime has been repeatedly demonstrated.

7.1.2 Thermal and Thermally-Induced Insulation Stress

Relatively high temperature has always been a main challenge in various branches of science and engineering. Electrical machines designers are not exempt from this issue, as the thermal constraint (i.e. maximum allowable temperature) limits the torque/power performance that a machine can deliver. For an EM, this limitation is synonymous with the intrinsic "thermal weakness" of insulating materials. The core of this Thesis has therefore focused on insulation stresses of thermal nature. Insulation aging and deterioration are investigated for both constant and variable temperature operations, making the proposed models of general validity. Tips and insides on how to maximise electrical machines performances - by exploiting at its best the insulation properties, although keeping acceptable reliability levels - are also provided. For doing so, each model is supported by a "real-life" case-study, where the introduced concepts are embedded in the electrical machine design workflow.

Thus far, the standard Arrhenius model has been used in existing literature for investigating the thermal aging of EM insulation systems [46, 49, 161-163]. However, these works, despite presenting thorough analyses, were usually aimed at providing the number of hours to failure of the EM's insulation system. This conventional methodology for addressing such a critical factor as it is the thermal aging, despite being the common practice for industrial motors, lacks in providing any trustworthy reliability figure applicable for the design of safety-critical, transportation EMs. This is why, in this Thesis, elements of statistical analysis and reliability engineering are combined to dielectrics physics of failure and accelerated life data. All this with the aim of deriving a comprehensive reliability-assessment tool, based on the EM properties, mission profile and operating environment. This tool is able to actually evaluate and quantify a) the EM's time to failure at any percentile (i.e. probability) and b) the reliability level (or probability of failure) after any number of operating cycles. The case-studies presented at the end of Chapters 4 and 5 serve the purpose of demonstrating how the proposed models and methodologies can be suitably employed when designing an EM. They highlight a main innovation of this work, i.e., the introduction of reliability and physics of failure considerations during the design stage of a machine. Rare, if not

inexistent, are the examples in literature in which the data on dielectrics aging are actually employed for designing and/or performing a comprehensive reliability assessment of a real EM.

7.1.3 Partial Discharges

The final "technical" Chapter of this work is dedicated to the analysis of partial discharges in low voltage electrical machines. As mentioned along the text, the study of partial discharges in this Thesis does not go in-depth in the physics of dielectrics. This is mainly a job for material scientists, physicists, chemists and dielectric experts, which have published, and keep publishing, excellent detailed analyses on the topic. This Thesis is focused on EMs and is aimed to inform EM designers. Therefore, the "partial discharge issue" is mainly treated from an electrical engineer point of view. The problem of voltage enhancement, due to modern, fast-switching power electronics converter is described. The consequent risk of partial discharges inception, in typical low voltage machines, is evaluated through combined empirical-numerical models. As for the thermal case, such models are integrated in to the design procedure of a real traction motor, where the trade-off study "reliability vs. performance" is carried out.

7.2 Main Achievements and Recognition

What presented in this Thesis is a first step towards making reliability and physics of failure an integral part of electrical machines design. The adoption of the proposed models and methodologies allows to exploit at its best the EM's insulation system. This in turn corresponds in enhanced power density and/or extended lifetime as clearly demonstrated through the various presented case-studies.

Most of the technical material presented in throughout this Thesis has already been published in high impact journal papers and top-tier conference proceedings leading to a total of 22 publications (in a three-years PhD programme). This demonstrates the strong interest of the scientific community in the proposed, game-changing design methodologies.

7.3 Future Work

This work is aimed at challenging the decade-old processes of how EMs are designed, where traditionally the machine is first designed and then simply 'checked' after to make sure it survives the required operating cycles. This work can therefore be considered as an initial "pioneering" study on the topic of reliability-oriented design of electrical machines, based on physics of failure methodology. The work produced in the three years of this PhD programme is an excellent step towards a much longer-term goal, where the whole degradation and lifetime prediction of an EM in its entirety, can be fully understood through real representative models, based on the physics of failure concept. However, the reality is that this goal is still far in the future. This Thesis itself with its main focus on thermal stresses for low-voltage, PD-free EMs, has only scratched the surface. Reliability is in itself a truly complex science, where innumerable factors and parameters all have significant effects on the final lifetime value(s). A lot of research, firstly focused on all the other stresses, and then projected to the various types and ratings of EMs (and in turn applications and environments), is required.

However, it must also be said that it is perceived that the break-through work contained in this Thesis can serve as the initial "eye-opener" for other researchers to start considering the potential of the proposed methodologies for future designs of EMs. It is hoped that the content of this Thesis will be developed to encompass other stresses, other applications, other machine types etc… all in the hope of one day achieving a truly reliable and robust EM that has near-zero over-engineering in its design.

In fact, there is still a myriad of research opportunities to be exploited by extending the work carried out in this this Thesis. The list below provides just some of the future work, which the Author is already involved in.

1. Short term objective (for the Author)
    a. Variations of the Arrhenius-Miner model for analysing machines with highly variable duty cycles. This work essentially consists in correcting the Arrhenius-Miner model for thermal cycling lifetime prediction, when high-gradient temperature profiles are

applied. In this case cracks and mechanical delamination might be induced in the winding's enamel insulation.

b. Evaluating the influence of secondary stressing factor on the lifetime of thermally-aged electrical machines. These can be e.g. external mechanical vibrations and the influence of high relative humidity. From the accelerated thermal aging tests it was noticed that, after some aging cycles, the magnet wire insulation becomes brittle and can be easily detached from the copper core. It is necessary to investigate if mechanical vibrations and humidity can 'accelerate' such a detachment process, causing premature failures.

2. Long term objectives (for the Author)
    a. Generalising the proposed models for any type of insulation (including type II, high voltage materials) and winding arrangements employed in electrical machines. This includes e.g. bars for high voltage machines, Litz-type windings, hairpin-type winding etc…
    b. Investigating the influence of high altitude (i.e. low pressure) on the partial discharge inception. Such analysis is necessary for designing electrical drives to be operated in aerospace environment.
    c. Proposing a model able to describe how the combination of high altitude and high voltage can deteriorate and shorten the lifetime of insulating materials for rotating electrical machines.
3. Long term objectives (for the Community)
    a. Developing a multi-stress lifetime prediction model for EMs to be employed in various applications and subject to different stressing factor. Such "super-model" needs to consider the influence of thermal, electrical, ambient and mechanical stress, acting simultaneously on the EM insulation.

b. The EM's insulation multi-stress model, whose focus is on failure of electrical nature, can be combined in a comprehensive reliability-assessment tool which also embeds considerations on failures of mechanical nature (e.g. bearings, shaft, etc…). Additionally, a highly ambitious objective would be that of combining the EM's multi-stress model with that of power electronics converters in order to obtain a system-level reliability assessment tool.

References

[1] B. Bilgin *et al.*, "Making the Case for Electrified Transportation," *IEEE Transactions on Transportation Electrification,* vol. 1, no. 1, pp. 4-17, 2015.

[2] B. Sarlioglu and C. T. Morris, "More Electric Aircraft: Review, Challenges, and Opportunities for Commercial Transport Aircraft," *IEEE Transactions on Transportation Electrification,* vol. 1, no. 1, pp. 54-64, 2015.

[3] A. Emadi, Y. J. Lee, and K. Rajashekara, "Power Electronics and Motor Drives in Electric, Hybrid Electric, and Plug-In Hybrid Electric Vehicles," *IEEE Transactions on Industrial Electronics,* vol. 55, no. 6, pp. 2237-2245, 2008.

[4] P. Wheeler and S. Bozhko, "The More Electric Aircraft: Technology and challenges," *IEEE Electrification Magazine,* vol. 2, no. 4, pp. 6-12, 2014.

[5] NASA, "On-Demand Mobility: Goals, Technical Challenges, and Roadmaps," *Available: https://ntrs.nasa.gov/archive/nasa/casi.ntrs.nasa.gov/20160006950.pdf Accessed: Dec. 2017.*

[6] A. S. Gohardani, G. Doulgeris, and R. Singh, "Challenges of future aircraft propulsion: A review of distributed propulsion technology and its potential application for the all electric commercial aircraft," *Progress in Aerospace Sciences,* vol. 47, no. 5, pp. 369-391, 7// 2011.

[7] E. National Academies of Sciences and Medicine, *Commercial Aircraft Propulsion and Energy Systems Research: Reducing Global Carbon Emissions*. Washington, DC: The National Academies Press, 2016, p. 122.

[8] H. S. McNaughton, "6 - Insulation," in *Electric Motor Handbook*, B. J. Chalmers, Ed.: Butterworth-Heinemann, 1988, pp. 332-392.

[9] V. Madonna, P. Giangrande, and M. Galea, "Electrical Power Generation in Aircraft: Review, Challenges, and Opportunities," *IEEE Transactions on Transportation Electrification,* vol. 4, no. 3, pp. 646-659, 2018.

[10] NASA, "Visions of the Future: Hybrid Electric Aircraft Propulsion," *AIAA Aircraft Electric/Hybrid-Electric Power & Propulsion Workshop, July 28, 2016. Available: https://ntrs.nasa.gov/archive/nasa/casi.ntrs.nasa.gov/20170002633.pdf Accessed: Dec. 2017.*

[11] R. H. Jansen, C. Bowman, A. Jankovsky, R. Dyson, and J. Felder, "Overview of NASA Electrified Aircraft Propulsion Research for Large Subsonic

Transports," *AIAA Propulsion and Energy 2017 Forum; 10-12 Jul. 2017; Atlanta, GA; United States. Available: https://ntrs.nasa.gov/search.jsp?R=20170006235 Accessed: Dec. 2017.*

[12] O. V. Thorsen and M. Dalva, "A survey of faults on induction motors in offshore oil industry, petrochemical industry, gas terminals, and oil refineries," *IEEE Transactions on Industry Applications,* vol. 31, no. 5, pp. 1186-1196, 1995.

[13] Y. Merizalde, L. Hernández-Callejo, and O. Duque-Perez, "State of the Art and Trends in the Monitoring, Detection and Diagnosis of Failures in Electric Induction Motors," *Energies,* vol. 10, no. 7, p. 1056, 2017.

[14] R. Brütsch, M. Tari, K. Fröhlich, T. Weiers, and R. Vogelsang, "Insulation Failure Mechanisms of Power Generators [Feature Article]," *IEEE Electrical Insulation Magazine,* vol. 24, no. 4, pp. 17-25, 2008.

[15] A. J. Bazurto, E. C. Quispe, and R. C. Mendoza, "Causes and failures classification of industrial electric motor," in *2016 IEEE ANDESCON*, 2016, pp. 1-4.

[16] M. G. Danikas and A. Karlis, "A review on electrical machines insulation aging and its relation to the power electronics arrangements with emphasis on wind turbine generators," *Renewable and Sustainable Energy Reviews,* vol. 15, no. 4, pp. 1748-1752, 5// 2011.

[17] L. Sang Bin, K. Tae-June, K. Heedong, K. Taesik, and L. Chaewoong, "Case studies of stator winding turn insulation failures in medium voltage motors," in *2017 Annual Pulp, Paper And Forest Industries Technical Conference (PPFIC)*, 2017, pp. 1-8.

[18] S. Grubic, J. M. Aller, B. Lu, and T. G. Habetler, "A Survey on Testing and Monitoring Methods for Stator Insulation Systems of Low-Voltage Induction Machines Focusing on Turn Insulation Problems," *IEEE Transactions on Industrial Electronics,* vol. 55, no. 12, pp. 4127-4136, 2008.

[19] M. Kaufhold, G. Borner, M. Eberhardt, and J. Speck, "Failure mechanism of the interturn insulation of low voltage electric machines fed by pulse-controlled inverters," *IEEE Electrical Insulation Magazine,* vol. 12, no. 5, pp. 9-16, 1996.

[20] G. M. Joksimovic and J. Penman, "The detection of inter-turn short circuits in the stator windings of operating motors," *IEEE Transactions on Industrial Electronics,* vol. 47, no. 5, pp. 1078-1084, 2000.

[21] Y. Qi, M. Zafarani, B. Akin, and S. E. Fedigan, "Analysis and Detection of Inter-Turn Short-Circuit Fault Through Extended Self-Commissioning," *IEEE Transactions on Industry Applications,* vol. 53, no. 3, pp. 2730-2739, 2017.

[22] E. Persson, "Transient effects in application of PWM inverters to induction motors," *IEEE Transactions on Industry Applications,* vol. 28, no. 5, pp. 1095-1101, 1992.

[23] M. Tozzi, A. Cavallini, and G. C. Montanari, "Monitoring off-line and on-line PD under impulsive voltage on induction motors - part 1: standard procedure," *IEEE Electrical Insulation Magazine,* vol. 26, no. 4, pp. 16-26, 2010.

[24] M. Kaufhold, H. Aninger, M. Berth, J. Speck, and M. Eberhardt, "Electrical stress and failure mechanism of the winding insulation in PWM-inverter-fed low-voltage induction motors," *IEEE Transactions on Industrial Electronics,* vol. 47, no. 2, pp. 396-402, 2000.

[25] J. W. Bennett, B. C. Mecrow, D. J. Atkinson, and G. J. Atkinson, "Safety-critical design of electromechanical actuation systems in commercial aircraft," *IET Electric Power Applications,* vol. 5, no. 1, pp. 37-47, 2011.

[26] A. Boglietti, A. Cavagnino, A. Tenconi, and S. Vaschetto, "The safety critical electric machines and drives in the more electric aircraft: A survey," in *2009 35th Annual Conference of IEEE Industrial Electronics*, 2009, pp. 2587-2594.

[27] J. A. Weimer, "The role of electric machines and drives in the more electric aircraft," in *Electric Machines and Drives Conference, 2003. IEMDC'03. IEEE International*, 2003, vol. 1, pp. 11-15 vol.1.

[28] G. Qiao, G. Liu, Z. Shi, Y. Wang, S. Ma, and T. C. Lim, "A review of electromechanical actuators for More/All Electric aircraft systems," *Proceedings of the Institution of Mechanical Engineers, Part C: Journal of Mechanical Engineering Science,* vol. 232, no. 22, pp. 4128-4151, 2018.

[29] P. Giangrande *et al.*, "Considerations on the Development of an Electric Drive for a Secondary Flight Control Electromechanical Actuator," *IEEE Transactions on Industry Applications,* vol. 55, no. 4, pp. 3544 - 3554, 2019.

[30] J. W. Bennett, B. C. Mecrow, A. G. Jack, and D. J. Atkinson, "A Prototype Electrical Actuator for Aircraft Flaps," *IEEE Transactions on Industry Applications,* vol. 46, no. 3, pp. 915-921, 2010.

[31] J. W. Bennet, "Fault tolerant electromechanical actuators for aircraft," PhD, Newcastle University, http://hdl.handle.net/10443/990, 2010.

[32] "IEC 60034-18-41:2014 - "Rotating electrical machines - Part 18-41: Partial discharge free electrical insulation systems (Type I) used in rotating electrical machines fed from voltage converters - Qualification and quality control tests"," ed, 2014.

[33] E. Levi, R. Bojoi, F. Profumo, H. A. Toliyat, and S. Williamson, "Multiphase induction motor drives - a technology status review," *IET Electric Power Applications,* vol. 1, no. 4, pp. 489-516, 2007.

[34] M. Villani, M. Tursini, G. Fabri, and L. Castellini, "High Reliability Permanent Magnet Brushless Motor Drive for Aircraft Application," *IEEE Transactions on Industrial Electronics,* vol. 59, no. 5, pp. 2073-2081, 2012.

[35] B. A. Welchko, T. A. Lipo, T. M. Jahns, and S. E. Schulz, "Fault tolerant three-phase AC motor drive topologies: a comparison of features, cost, and limitations," *IEEE Transactions on Power Electronics,* vol. 19, no. 4, pp. 1108-1116, 2004.

[36] B. C. Mecrow, A. G. Jack, J. A. Haylock, and J. Coles, "Fault-tolerant permanent magnet machine drives," *IEE Proceedings - Electric Power Applications,* vol. 143, no. 6, pp. 437-442, 1996.

[37] G. C. Montanari and L. Simoni, "Aging phenomenology and modeling," *IEEE Transactions on Electrical Insulation,* vol. 28, no. 5, pp. 755-776, 1993.

[38] *IEC 60505:2011 Evaluation and qualification of electrical insulation systems*, 2011.

[39] *IEC 60034-18-42:2017 Rotating Electrical Machines - Part 18-42: Partial discharge resistant electrical insulation systems (Type II) used in rotating electrical machines fed from voltage converters - Qualification tests*, 2017.

[40] G. C. Stone, I. Culbert, E. A. Boulter, and H. Dhirani, *Electrical Insulation for Rotating Machines: Design, Evaluation, Aging, Testing, and Repair*. Wiley, 2014.

[41] H. Zhe, "Modeling and Testing of Insulation Degradation due to Dynamic Thermal Loading of Electrical Machines," PhD, Lund University, 2017.

[42] Y. Da, X. Shi, and M. Krishnamurthy, "Health monitoring, fault diagnosis and failure prognosis techniques for Brushless Permanent Magnet Machines," in *2011 IEEE Vehicle Power and Propulsion Conference*, 2011, pp. 1-7.

[43] J. Faiz, H. Nejadi-Koti, and Z. Valipour, "Comprehensive review on inter-turn fault indexes in permanent magnet motors," *IET Electric Power Applications,* vol. 11, no. 1, pp. 142-156, 2017.

[44] V. M. Montsinger, "Loading Transformers By Temperature," *Transactions of the American Institute of Electrical Engineers,* vol. 49, no. 2, pp. 776-790, 1930.

[45] T. W. Dakin, "Electrical Insulation Deterioration Treated as a Chemical Rate Phenomenon," *Transactions of the American Institute of Electrical Engineers,* vol. 67, no. 1, pp. 113-122, 1948.

[46] C. Han, "Lifetime evaluation of class E electrical insulation for small induction motors," *IEEE Electrical Insulation Magazine,* vol. 27, no. 3, pp. 14-19, 2011.

[47] G. C. Montanari and G. Pattini, "Thermal Endurance Evaluation of Insulating Materials: A Theoretical and Experimental Analysis," *IEEE Transactions on Electrical Insulation,* vol. EI-21, no. 1, pp. 69-77, 1986.

[48] G. C. Montanari, G. Mazzanti, and L. Simoni, "Progress in electrothermal life modeling of electrical insulation during the last decades," *IEEE Transactions on Dielectrics and Electrical Insulation,* vol. 9, no. 5, pp. 730-745, 2002.

[49] R. Rothe and K. Hameyer, "Life expectancy calculation for electric vehicle traction motors regarding dynamic temperature and driving cycles," in *2011 IEEE International Electric Machines & Drives Conference (IEMDC)*, 2011, pp. 1306-1309.

[50] E. L. Brancato, "Estimation of lifetime expectancies of motors," *IEEE Electrical Insulation Magazine,* vol. 8, no. 3, pp. 5-13, 1992.

[51] K. Tshiloz, A. C. Smith, A. Mohammed, S. Djurović, and T. Feehally, "Real-time insulation lifetime monitoring for motor windings," in *2016 XXII International Conference on Electrical Machines (ICEM)*, 2016, pp. 2335-2340.

[52] G. Mazzanti, "Analysis of the Combined Effects of Load Cycling, Thermal Transients, and Electrothermal Stress on Life Expectancy of High-Voltage AC Cables," *IEEE Transactions on Power Delivery,* vol. 22, no. 4, pp. 2000-2009, 2007.

[53] M. A. Miner, "Cumulative damage in fatigue," *Journal of Applied Mechanics,* vol. 12, no. 3, pp. 159-164, 1945.

[54] G. C. Stone, J. F. Lyles, J. M. Braun, and C. L. Kaul, "A thermal cycling type test for generator stator winding insulation," *IEEE Transactions on Energy Conversion,* vol. 6, no. 4, pp. 707-713, 1991.

[55] B. K. Gupta and W. T. Fink, "A proposed type test for interturn insulation in multi-turn coils," in *Conference Record of the 1996 IEEE International Symposium on Electrical Insulation*, 1996, vol. 1, pp. 235-238 vol.1.

[56] Z. Jia, X. Peng, Z. Guan, L. Wang, and B. Yue, "Evaluation of the Degradation of Generator Stator Ground Wall Insulation Under Multistresses Aging," *IEEE Transactions on Energy Conversion,* vol. 23, no. 2, pp. 474-483, 2008.

[57] Z. Huang, A. Reinap, and M. Alaküla, "Degradation and fatigue of epoxy impregnated traction motors due to thermal and thermal induced mechanical stress - part I: Thermal mechanical simulation of single wire due to evenly distributed temperature," in *8th IET International Conference on Power Electronics, Machines and Drives (PEMD 2016)*, 2016, pp. 1-6.

[58] Z. Huang, A. Reinap, and M. Alaküla, "Degradation and fatigue of epoxy impregnated traction motors due to thermal and thermal induced mechanical stress - part II: Thermal mechanical simulation of multiple wires due to evenly and unevenly distributed temperature," in *8th IET International Conference on Power Electronics, Machines and Drives (PEMD 2016)*, 2016, pp. 1-5.

[59] C. Sciascera, M. Galea, P. Giangrande, and C. Gerada, "Lifetime consumption and degradation analysis of the winding insulation of electrical machines," in *8th IET International Conference on Power Electronics, Machines and Drives (PEMD 2016)*, 2016, pp. 1-5.

[60] D. E. Moghadam, J. Speck, S. Grossmann, and J. Stahl, "Parameters affecting the turn insulation lifetime and durability," *IEEE Transactions on Dielectrics and Electrical Insulation,* vol. 25, no. 2, pp. 516-523, 2018.

[61] G. C. Crichton, P. W. Karlsson, and A. Pedersen, "Partial discharges in ellipsoidal and spheroidal voids," *IEEE Transactions on Electrical Insulation,* vol. 24, no. 2, pp. 335-342, 1989.

[62] B. Fruth and L. Niemeyer, "The importance of statistical characteristics of partial discharge data," *IEEE Transactions on Electrical Insulation,* vol. 27, no. 1, pp. 60-69, 1992.

[63] T. W. Dakin *et al.*, "Breakdown of gases in uniform fields," *Proc. Int. Conf. Large High Voltage Electric Systems, CIGRE, SC 15,* pp. 1-42, 1977.

[64] H. Okubo, N. Hayakawa, and G. C. Montanari, "Technical Development on Partial Discharge Measurement and Electrical Insulation Techniques for Low

Voltage Motors Driven by Voltage Inverters," *IEEE Transactions on Dielectrics and Electrical Insulation,* vol. 14, no. 6, pp. 1516-1530, 2007.

[65] T. Wakimoto, H. Kojima, and N. Hayakawa, "Measurement and evaluation of partial discharge inception voltage for enameled rectangular wires under AC voltage," *IEEE Transactions on Dielectrics and Electrical Insulation,* vol. 23, no. 6, pp. 3566-3574, 2016.

[66] N. Hayakawa and H. Okubo, "Partial discharge characteristics of inverter-fed motor coil samples under ac and surge voltage conditions," *IEEE Electrical Insulation Magazine,* vol. 21, no. 1, pp. 5-10, 2005.

[67] I. Cotton, A. Nelms, and M. Husband, "Higher voltage aircraft power systems," *IEEE Aerospace and Electronic Systems Magazine,* vol. 23, no. 2, pp. 25-32, 2008.

[68] D. Bogh, J. Coffee, G. Stone, and J. Custodio, "Partial-discharge-inception testing on low-voltage motors," *IEEE Transactions on Industry Applications,* vol. 42, no. 1, pp. 148-154, 2006.

[69] P. Wang, G. C. Montanari, and A. Cavallini, "Partial Discharge Phenomenology and Induced Aging Behavior in Rotating Machines Controlled by Power Electronics," *IEEE Transactions on Industrial Electronics,* vol. 61, no. 12, pp. 7105-7112, 2014.

[70] A. Cavallini, "Reliability of low voltage inverter-fed motors: What have we learned, perspectives, open points," in *2017 International Symposium on Electrical Insulating Materials (ISEIM)*, 2017, vol. 1, pp. 13-22.

[71] A. Cavallini, D. Fabiani, and G. C. Montanari, "Power electronics and electrical insulation systems - Part 1: Phenomenology overview," *IEEE Electrical Insulation Magazine,* vol. 26, no. 3, pp. 7-15, 2010.

[72] A. Cavallini, D. Fabiani, and G. C. Montanari, "Power electronics and electrical insulation systems - part 2: life modeling for insulation design," *IEEE Electrical Insulation Magazine,* vol. 26, no. 4, pp. 33-39, 2010.

[73] A. Cavallini, D. Fabiani, and G. C. Montanari, "Power electronics and electrical insulation systems - Part 3: Diagnostic properties," *IEEE Electrical Insulation Magazine,* vol. 26, no. 5, pp. 30-40, 2010.

[74] J. Rodriguez, R. M. Kennel, J. R. Espinoza, M. Trincado, C. A. Silva, and C. A. Rojas, "High-Performance Control Strategies for Electrical Drives: An Experimental Assessment," *IEEE Transactions on Industrial Electronics,* vol. 59, no. 2, pp. 812-820, 2012.

[75] J. W. Finch and D. Giaouris, "Controlled AC Electrical Drives," *IEEE Transactions on Industrial Electronics,* vol. 55, no. 2, pp. 481-491, 2008.

[76] D. Casadei, F. Profumo, G. Serra, and A. Tani, "FOC and DTC: two viable schemes for induction motors torque control," *IEEE Transactions on Power Electronics,* vol. 17, no. 5, pp. 779-787, 2002.

[77] J. Nerg, M. Rilla, V. Ruuskanen, J. Pyrhönen, and S. Ruotsalainen, "Direct-Driven Interior Magnet Permanent-Magnet Synchronous Motors for a Full

Electric Sports Car," *IEEE Transactions on Industrial Electronics,* vol. 61, no. 8, pp. 4286-4294, 2014.

[78] F. Parasiliti, M. Villani, S. Lucidi, and F. Rinaldi, "Finite-Element-Based Multiobjective Design Optimization Procedure of Interior Permanent Magnet Synchronous Motors for Wide Constant-Power Region Operation," *IEEE Transactions on Industrial Electronics,* vol. 59, no. 6, pp. 2503-2514, 2012.

[79] F. Yan, J. Wang, and K. Huang, "Hybrid Electric Vehicle Model Predictive Control Torque-Split Strategy Incorporating Engine Transient Characteristics," *IEEE Transactions on Vehicular Technology,* vol. 61, no. 6, pp. 2458-2467, 2012.

[80] J. O. Estima and A. J. M. Cardoso, "Efficiency Analysis of Drive Train Topologies Applied to Electric/Hybrid Vehicles," *IEEE Transactions on Vehicular Technology,* vol. 61, no. 3, pp. 1021-1031, 2012.

[81] W. Cao, B. C. Mecrow, G. J. Atkinson, J. W. Bennett, and D. J. Atkinson, "Overview of Electric Motor Technologies Used for More Electric Aircraft (MEA)," *IEEE Transactions on Industrial Electronics,* vol. 59, no. 9, pp. 3523-3531, 2012.

[82] M. Lukic *et al.*, "State of the Art of Electric Taxiing Systems," in *2018 IEEE ESARS-ITEC*, 2018, pp. 1-6.

[83] D. Fabiani, "Accelerated degradation of ac-motor winding insulation due to voltage waveforms generated by adjustable speed drives," PhD, University of Bologna, Bologna, Italy, 2003.

[84] A. Morya and H. A. Toliyat, "Insulation design for Wide Bandgap (WBG) device based voltage source converter fed motors," in *2017 IEEE 5th Workshop on Wide Bandgap Power Devices and Applications (WiPDA)*, 2017, pp. 74-79.

[85] P. Wang, H. Xu, J. Wang, W. Wang, and A. Cavallini, "Effect of repetitive impulsive voltage duty cycle on partial discharge features and insulation endurance of enameled wires for inverter-fed low voltage machines," *IEEE Transactions on Dielectrics and Electrical Insulation,* vol. 24, no. 4, pp. 2123-2131, 2017.

[86] L. Benmamas, P. Teste, E. Odic, G. Krebs, and T. Hamiti, "Contribution to the analysis of PWM inverter parameters influence on the partial discharge inception voltage," *IEEE Transactions on Dielectrics and Electrical Insulation,* vol. 26, no. 1, pp. 146-152, 2019.

[87] M. Denk and M. M. Bakran, "Partial Discharge Measurement in a Motor Winding Fed by a SiC Inverter - How Critical is High dV/dt Really?," in *PCIM Europe 2018; International Exhibition and Conference for Power Electronics, Intelligent Motion, Renewable Energy and Energy Management*, 2018, pp. 1-6.

[88] T. J. Å. Hammarström, "Partial discharge characteristics at ultra-short voltage risetimes," *IEEE Transactions on Dielectrics and Electrical Insulation,* vol. 25, no. 6, pp. 2241-2249, 2018.

[89] L. Lusuardi, A. Cavallini, M. G. d. l. Calle, J. M. Martínez-Tarifa, and G. Robles, "Insulation design of low voltage electrical motors fed by PWM inverters," *IEEE Electrical Insulation Magazine,* vol. 35, no. 3, pp. 7-15, 2019.

[90] T. J. Å. Hammarström, "Partial discharge characteristics within motor insulatioi exposed to multi-level PWM waveforms," *IEEE Transactions on Dielectrics and Electrical Insulation,* vol. 25, no. 2, pp. 559-567, 2018.

[91] C. Abadie, T. Billard, and T. Lebey, "Partial Discharges in Motor Fed by Inverter: From Detection to Winding Configuration," *IEEE Transactions on Industry Applications,* vol. 55, no. 2, pp. 1332-1341, 2019.

[92] *IEC 60270:2015 High-voltage test techniques - Partial discharge measurements*, 2015.

[93] M. Tozzi, A. Cavallini, and G. C. Montanari, "Monitoring off-line and on-line PD under impulsive voltage on induction motors - Part 2: testing*," *IEEE Electrical Insulation Magazine,* vol. 27, no. 1, pp. 14-21, 2011.

[94] B. Taghia, T. Billard, J. Carayon, D. Malec, H. Piquet, and A. Belinger, "Investigations on Partial Discharges Risk in Aeronautical Rotating Machine Fed by HVDC 540VDC Network," in *2018 IEEE Electrical Insulation Conference (EIC)*, 2018, pp. 491-494.

[95] A. Boglietti, A. Cavagnino, D. Staton, M. Shanel, M. Mueller, and C. Mejuto, "Evolution and Modern Approaches for Thermal Analysis of Electrical Machines," *IEEE Transactions on Industrial Electronics,* vol. 56, no. 3, pp. 871-882, 2009.

[96] N. Bianchi, E. Fornasiero, and S. Bolognani, "Thermal Analysis of a Five-Phase Motor Under Faulty Operations," *IEEE Transactions on Industry Applications,* vol. 49, no. 4, pp. 1531-1538, 2013.

[97] P. H. Mellor, D. Roberts, and D. R. Turner, "Lumped parameter thermal model for electrical machines of TEFC design," *IEE Proceedings B - Electric Power Applications,* vol. 138, no. 5, pp. 205-218, 1991.

[98] C. Sciascera, P. Giangrande, L. Papini, C. Gerada, and M. Galea, "Analytical Thermal Model for Fast Stator Winding Temperature Prediction," *IEEE Transactions on Industrial Electronics,* vol. 64, no. 8, pp. 6116-6126, 2017.

[99] M. Galea, C. Gerada, T. Raminosoa, and P. Wheeler, "A Thermal Improvement Technique for the Phase Windings of Electrical Machines," *IEEE Transactions on Industry Applications,* vol. 48, no. 1, pp. 79-87, 2012.

[100] J. Godbehere, R. Wrobel, D. Drury, and P. H. Mellor, "Experimentally Calibrated Thermal Stator Modeling of AC Machines for Short-Duty Transient Operation," *IEEE Transactions on Industry Applications,* vol. 53, no. 4, pp. 3457-3466, 2017.

[101] A. Boglietti, A. Cavagnino, and D. Staton, "Determination of Critical Parameters in Electrical Machine Thermal Models," *IEEE Transactions on Industry Applications,* vol. 44, no. 4, pp. 1150-1159, 2008.

[102] R. Wrobel, S. J. Williamson, J. D. Booker, and P. H. Mellor, "Characterizing the in situ Thermal Behavior of Selected Electrical Machine Insulation and Impregnation Materials," *IEEE Transactions on Industry Applications,* vol. 52, no. 6, pp. 4678-4687, 2016.

[103] V. Madonna, P. Giangrande, C. Gerada, and M. Galea, "Thermal analysis of fault-tolerant electrical machines for aerospace actuators," *IET Electric Power Applications,* vol. 13, no. 7, pp. 843-852, 2019.

[104] P. Giangrande, V. Madonna, S. Nuzzo, and M. Galea, "Design of Fault-Tolerant Dual Three-Phase Winding PMSM for Helicopter Landing Gear EMA," presented at the 2018 IEEE ESARS-ITEC, Nottingham UK, 2018.

[105] A. Boglietti, E. Carpaneto, M. Cossale, and S. Vaschetto, "Stator-Winding Thermal Models for Short-Time Thermal Transients: Definition and Validation," *IEEE Transactions on Industrial Electronics,* vol. 63, no. 5, pp. 2713-2721, 2016.

[106] L. Idoughi, X. Mininger, F. Bouillault, L. Bernard, and E. Hoang, "Thermal Model With Winding Homogenization and FIT Discretization for Stator Slot," *IEEE Transactions on Magnetics,* vol. 47, no. 12, pp. 4822-4826, 2011.

[107] N. Simpson, R. Wrobel, and P. H. Mellor, "Estimation of Equivalent Thermal Parameters of Impregnated Electrical Windings," *IEEE Transactions on Industry Applications,* vol. 49, no. 6, pp. 2505-2515, 2013.

[108] J. Pyrhonen, T. Jokinen, and V. Hrabovcova, *Design of rotating electrical machines*. John Wiley & Sons, 2009.

[109] W. Tong, *Mechanical Design of Electric Motors*. Taylor & Francis, 2014.

[110] S. Ayat, H. Liu, F. Chauvicourt, and R. Wrobel, "Experimental Derivation of Thermal Parameters of the Stator- Winding Region in Thermal Analysis of PM Electrical Machines," in *IECON 2018 - 44th Annual Conference of the IEEE Industrial Electronics Society*, 2018, pp. 496-501.

[111] Z. Li, J. Guo, D. Fu, G. Gu, and B. Xiong, "Research on heat transfer of spraying evaporative cooling technique for large electrical machine," in *2009 International Conference on Electrical Machines and Systems*, 2009, pp. 1-4.

[112] C. Liu *et al.*, "Experimental Investigation on Oil Spray Cooling with Hairpin Windings," *IEEE Transactions on Industrial Electronics,* pp. 1-1, 2019.

[113] S. Bozhko *et al.*, "Development of Aircraft Electric Starter–Generator System Based on Active Rectification Technology," *IEEE Transactions on Transportation Electrification,* vol. 4, no. 4, pp. 985-996, 2018.

[114] P. Lindh *et al.*, "Performance of a Direct-Liquid-Cooled Motor in an Electric Bus Under Different Load Cycles," *IEEE Access,* vol. 7, pp. 86897-86905, 2019.

[115] Y. Gai *et al.*, "Cooling of Automotive Traction Motors: Schemes, Examples, and Computation Methods," *IEEE Transactions on Industrial Electronics,* vol. 66, no. 3, pp. 1681-1692, 2019.

[116] M. Popescu, D. A. Staton, A. Boglietti, A. Cavagnino, D. Hawkins, and J. Goss, "Modern Heat Extraction Systems for Power Traction Machines - A Review," *IEEE Transactions on Industry Applications,* vol. 52, no. 3, pp. 2167-2175, 2016.

[117] V. Madonna, A. Walker, P. Giangrande, G. Serra, C. Gerada, and M. Galea, "Improved Thermal Management and Analysis for Stator End-Windings of Electrical Machines," *IEEE Transactions on Industrial Electronics,* vol. 66, no. 7, pp. 5057-5069, 2019.

[118] A. Walker, M. Galea, C. Gerada, A. Mebarki, and D. Gerada, "Design considerations for high performance traction machines: Aiming for the FreedomCar 2020 targets," in *2015 International Conference on Electrical Systems for Aircraft, Railway, Ship Propulsion and Road Vehicles (ESARS)*, 2015, pp. 1-6.

[119] V. Madonna, P. Giangrande, C. Gerada, and M. Galea, "Thermal analysis of fault-tolerant electrical machines for more electric aircraft applications," *The Journal of Engineering,* vol. 2018, no. 13, pp. 461-467, 2018.

[120] P. Giangrande, V. Madonna, S. Nuzzo, C. Gerada, and M. Galea, "Braking Torque Compensation Strategy and Thermal Behavior of a Dual Three-Phase Winding PMSM During Short-Circuit Fault," presented at the IEMDC 2019 - International Electric Machines and Drives Conference, 2019.

[121] P. Giangrande, V. Madonna, S. Nuzzo, C. Spagnolo, C. Gerada, and M. Galea, "Reduced Order Lumped Parameter Thermal Network for Dual Three-Phase Permanent Magnet Machines," presented at the IEEE WEMDCD'19 - Workshop on Electrical Machines Design, Control and Diagnostics, 2019.

[122] V. Madonna, P. Giangrande, A. Walker, and M. Galea, "On the Effects of Advanced End-Winding Cooling on the Design and Performance of Electrical Machines," in *2018 XIII International Conference on Electrical Machines (ICEM)*, 2018, pp. 311-317.

[123] A. Bellini, F. Filippetti, C. Tassoni, and G. Capolino, "Advances in Diagnostic Techniques for Induction Machines," *IEEE Transactions on Industrial Electronics,* vol. 55, no. 12, pp. 4109-4126, 2008.

[124] W. B. Nelson, *Accelerated testing: statistical models, test plans, and data analysis*. John Wiley & Sons, 2009.

[125] "IEEE Standard Test Procedure for Thermal Evaluation of Systems of Insulating Materials for Random-Wound AC Electric Machinery," *IEEE Std 117-2015 (Revision of IEEE Std 117-1974),* pp. 1-34, 2016.

[126] *IEC 60034 18-21: Functional evaluation of insulation systems - Test procedures for wire-wound windings - Thermal Evaluation and classification*, 2012.

[127] *IEC 60172:2015 Test procedure for the determination of the temperature index of enamelled and tape wrapped winding wires*, 2015.

[128] V. Madonna, P. Giangrande, G. Migliazza, G. Buticchi, and M. Galea, "A Time-Saving Approach for the Thermal Lifetime Evaluation of Low Voltage

Electrical Machines," *IEEE Transactions on Industrial Electronics,* pp. 1-1, 2019.

[129] F. N. Nwobi and C. A. Ugomma, "A comparison of methods for the estimation of Weibull distribution parameters," *Metodoloski zvezki,* vol. 11, no. 1, p. 65, 2014.

[130] *ASTM International - D1676-17 Standard Test Methods for Film-Insulated Magnet Wire*, 2017.

[131] P. Mancinelli, S. Stagnitta, and A. Cavallini, "Qualification of Hairpin Motors Insulation for Automotive Applications," *IEEE Transactions on Industry Applications,* vol. 53, no. 3, pp. 3110-3118, 2017.

[132] V. Madonna, G. Migliazza, P. Giangrande, E. Lorenzani, G. Buticchi, and M. Galea, "The Rebirth of the Current Source Inverter: Advantages for Aerospace Motor Design," *IEEE Industrial Electronics Magazine,* vol. 13, no. 4, pp. 65-76, 2019.

[133] *Certification Specifications and Acceptable Means of Compliance for Large Aeroplanes (CS-25) (Amendment 23)*, 2019.

[134] V. Madonna, P. Giangrande, W. Zhao, Y. Wang, H. Zhang, and M. Galea, "Insulation Capacitance as Diagnostic Marker for Thermally Aged, Low Voltage Electrical Machines," in *2019 22nd International Conference on Electrical Machines and Systems (ICEMS)*, 2019, pp. 1-5.

[135] V. Madonna, P. Giangrande, G. Migliazza, G. Buticchi, and M. Galea, "On the Thermal Insulation Qualification of Low Voltage Electrical Machines," in *IECON 2019 - 45th Annual Conference of the IEEE Industrial Electronics Society*, 2019, vol. 1, pp. 7115-7120.

[136] Solvay, "Torlon PAI Design Guide," ed. www.solvay.com, 2015.

[137] T. J. Barlow, *A Reference Book of Driving Cycles for Use in the Measurement of Road Vehicle Emissions: Version 3*. IHS, 2009.

[138] P. Yedamale, "Brushless DC (BLDC) motor fundamentals," *Microchip Technology Inc,* vol. 20, pp. 3-15, 2003.

[139] T. Lee, M. Seo, Y. Kim, and S. Jung, "Motor Design and Characteristics Comparison of Outer-Rotor-Type BLDC Motor and BLAC Motor Based on Numerical Analysis," *IEEE Transactions on Applied Superconductivity,* vol. 26, no. 4, pp. 1-6, 2016.

[140] V. Madonna, P. Giangrande, L. Lusuardi, A. Cavallini, C. Gerada, and M. Galea, "Thermal Overload and Insulation Aging of Short Duty Cycle, Aerospace Motors," *IEEE Transactions on Industrial Electronics,* vol. 67, no. 4, pp. 2618-2629, 2020.

[141] M. Galea, P. Giangrande, V. Madonna, and G. Buticchi, "Insulation systems for electrical machines: Reliability MUST become a main design objective," *IEEE Industrial Electronics Magazine,* vol. 14, no. 1, 2020.

[142] V. Madonna, P. Giangrande, L. Lusuardi, A. Cavallini, and M. Galea, "Impact of thermal overload on the insulation aging in short duty cycle motors for

aerospace," in *2018 IEEE International Conference on Electrical Systems for Aircraft, Railway, Ship Propulsion and Road Vehicles & International Transportation Electrification Conference (ESARS-ITEC)*, 2018, pp. 1-6.

[143] B. Taghia, B. Cougo, H. Piquet, D. Malec, A. Belinger, and J.-P. Carayon, "Overvoltage at motor terminals in SiC-based PWM drives," *Mathematics and Computers in Simulation,* 2018/09/27/ 2018.

[144] M. F. Rahman, T. Haider, E. Haque, T. R. Blackburn, and C. Grantham, "Modelling and experimental studies of effects of steep fronted inverter waveforms on motor and supply cabling and their remedies," in *Proceedings of the IEEE 1999 International Conference on Power Electronics and Drive Systems. PEDS'99 (Cat. No.99TH8475)*, 1999, vol. 1, pp. 519-524 vol.1.

[145] L. V. Bewley, "Traveling Waves on Transmission Systems," *Transactions of the American Institute of Electrical Engineers,* vol. 50, no. 2, pp. 532-550, 1931.

[146] CREE. *E3M0065090D Datasheet, Available: https://www.wolfspeed.com/downloads/dl/file/id/1305/product/358/e3m0065090d.pdf.*

[147] CREE. (12/2018). *CAS120M12BM2, 1.2kV All-Silicon Carbide Half-Bridge Module. Available: https://www.wolfspeed.com/cas120m12bm2*.

[148] G. C. Montanari and P. Seri, "About the Definition of PDIV and RPDIV in Designing Insulation Systems for Rotating Machines Controlled by Inverters," in *2018 IEEE Electrical Insulation Conference (EIC)*, 2018, pp. 554-557.

[149] K. Kimura, "The role of IEC 60034-27-5 for IEC 60034-18-41: Offline PD test methods with repetitive impulse voltage," in *2017 International Symposium on Electrical Insulating Materials (ISEIM)*, 2017, vol. 1, pp. 155-158.

[150] N. Hayakawa, F. Shimizu, and H. Okubo, "Estimation of partial discharge inception voltage of magnet wires under inverter surge voltage by volume-time theory," *IEEE Transactions on Dielectrics and Electrical Insulation,* vol. 19, no. 2, pp. 550-557, 2012.

[151] *IEC 60317-0-1:2013 Specifications for particular types of winding wires - Part 0-1: General requirements - Enamelled round copper wire*, 2013.

[152] "IEEE Recommended Practice for Measurement of Power Factor Tip-Up of Electric Machinery Stator Coil Insulation," *IEEE Std 286-2000,* pp. i-29, 2001.

[153] *D150-18, Standard Test Methods for AC Loss Characteristics and Permittivity (Dielectric Constant) of Solid Electrical Insulation*, 2018.

[154] K. J. Andrew, "Dielectric relaxation in solids," *Journal of Physics D: Applied Physics,* vol. 32, no. 14, p. R57, 1999.

[155] M. Farahani, H. Borsi, and E. Gockenbach, *Study of Capacitance and Dissipation Factor Tip-Up to Evaluate the Condition of Insulating Systems for High Voltage Rotating Machines*. 2007, pp. 263-270.

[156] F. T. Emery, "Partial discharge, dissipation factor, and corona aspects for high voltage electric generator stator bars and windings," *IEEE Transactions on Dielectrics and Electrical Insulation,* vol. 12, no. 2, pp. 347-361, 2005.

[157] M. Farahani, H. Borsi, E. Gockenbach, and M. Kaufhold, "Partial discharge and dissipation factor behavior of model insulating systems for high voltage rotating machines under different stresses," *IEEE Electrical Insulation Magazine,* vol. 21, no. 5, pp. 5-19, 2005.

[158] V. Madonna, P. Giangrande, and M. Galea, "Evaluation of Strand-to-Strand Capacitance and Dissipation Factor in Thermally Aged Enameled Coils for Low voltage Electrical Machines," *IET Science, Measurement & Technology,* vol. 13, no. 8, pp. 1170-1777, 2019.

[159] V. Madonna, P. Giangrande, W. Zhao, H. Zhang, C. Gerada, and M. Galea, "On the Design of Partial Discharge-Free Low Voltage Electrical Machines," presented at the IEMDC 2019 - International Electric Machines & Drives Conference, 2019.

[160] V. Madonna *et al.*, "Reliability vs. Performances of Electrical Machines: Partial Discharges Issue," presented at the IEEE WEMDCD'19 - Workshop on Electrical Machines Design, Control and Diagnosis, Athens, Greece, 2019.

[161] N. Lahoud, M. Q. Nguyen, P. Maussion, D. Malec, and D. Mary, "Lifetime model of the inverter-fed motors secondary insulation by using a design of experiments," *IEEE Transactions on Dielectrics and Electrical Insulation,* vol. 22, no. 6, pp. 3170-3176, 2015.

[162] M. Farahani, E. Gockenbach, H. Borsi, K. Schafer, and M. Kaufhold, "Behavior of machine insulation systems subjected to accelerated thermal aging test," *IEEE Transactions on Dielectrics and Electrical Insulation,* vol. 17, no. 5, pp. 1364-1372, 2010.

[163] D. Huger and D. Gerling, "An advanced lifetime prediction method for permanent magnet synchronous machines," in *2014 International Conference on Electrical Machines (ICEM)*, 2014, pp. 686-691.

Appendix A Thermal Analysis of an Outer Rotor BLDC Motor

The temperature profile of the BLDC motor presented in Chapter 5 (i.e. propulsion motor for light UAV) is obtained through an LPTN. The latter considers axial and radial heat transfers and it is built in Matlab® Simscape environment. Its layout is shown in Fig. A.1. Each active node consists of a heat source, whose power magnitude is calculated according to the EM power loss distribution, and a thermal mass (i.e. capacitance) necessary for transient thermal simulations. The computation of thermal elements in the LPTN follows the standard procedure reported in Chapter 3.

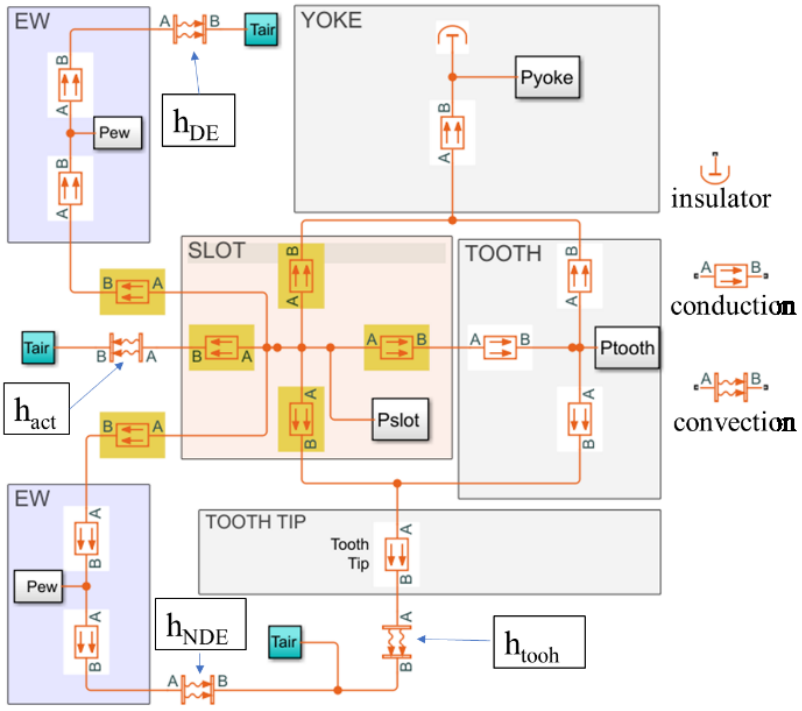

Fig. A.1 BLDC LPTN which considers radial and axial heat transfer.

As the hot-spot temperature is expected to be in the winding, the rotor has not been included in the LPTN. This assumption is valid since the heat produced within the stator is mainly transferred to the ambient air due to the open end caps arrangement. Also, the solid power losses (i.e. core and PMs) within the rotor are one order of magnitude lower than those of the stator, as can be observed in Fig. A.2, where the solid losses per unit mass are computed using the commercial software MotorCAD®. Furthermore, given the EM arrangement (i.e. outer rotor) and the relatively high rotational speed, the loss generated within the rotor are dissipated towards the ambient air through forced convection.

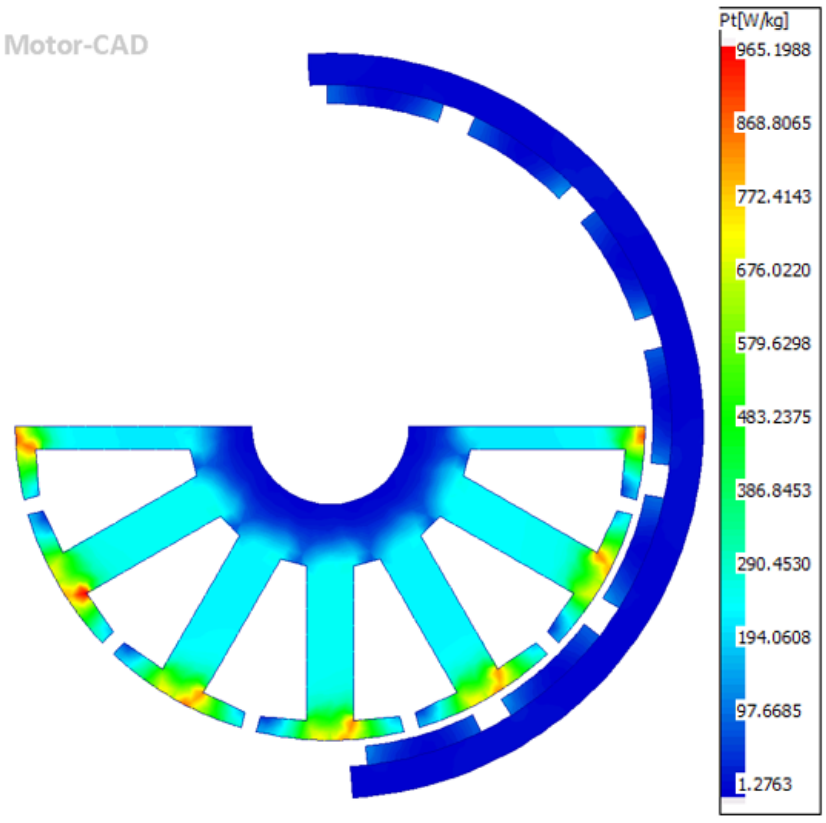

Fig. A.2 BLDC core and PMs power loss per unit weight.

The stator surfaces considered in the computation of forced convection coefficients are shown in Fig. A.3. For the sake of clarity, the 3D view of the EM (including the front end cap and the direction of the airflow) is depicted in Fig. A.4.

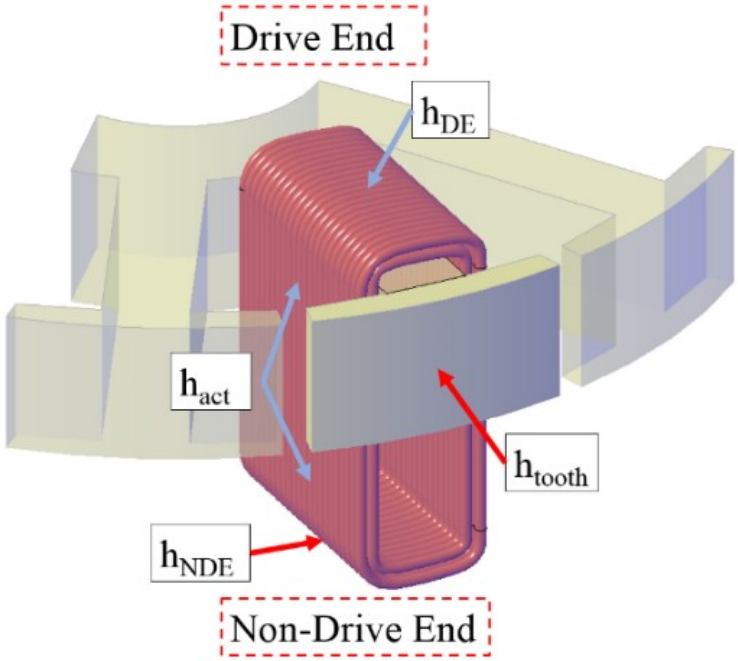

Fig. A.3 Coefficients of forced convection and relative external surfaces.

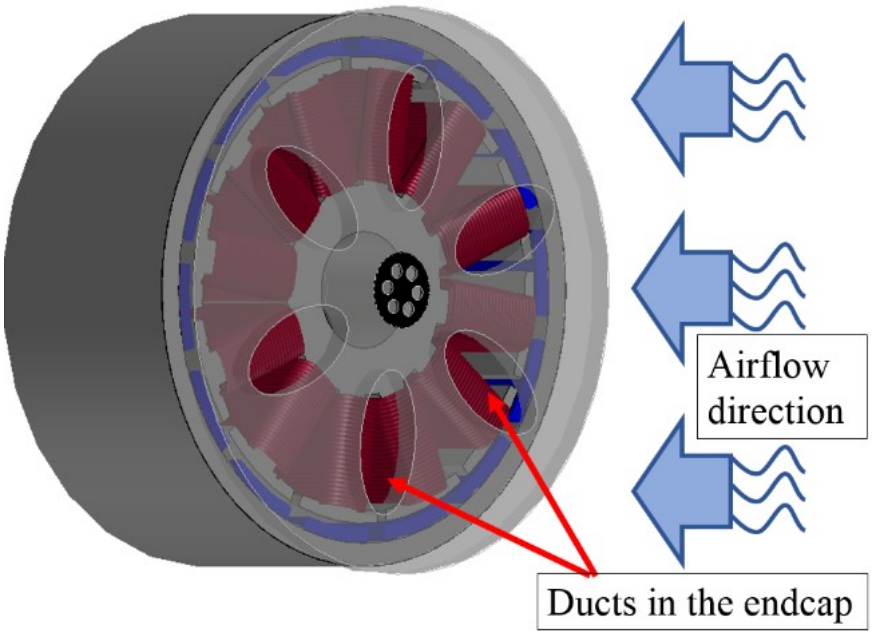

Fig. A.4 BLDC 3D view including end cap and airflow direction.

Given the complex airflow distribution, it is relatively complicated to analytically determine the forced convection coefficients. For this reason, a CFD

simulation has been performed for completing the aforementioned task. The air-velocity pathline plot for the EM's internal air, obtained with ANSYS® Fluent, is reported in Fig. A.5. For this simulation, it has been assumed that the airflow entering the front end cap has a velocity of 28 m/s (i.e. UAV cruising at ≈100 km/h). The cross sectional area considered for the CFD simulation (i.e. AA' – BB') is the one reported in Fig. A.6.

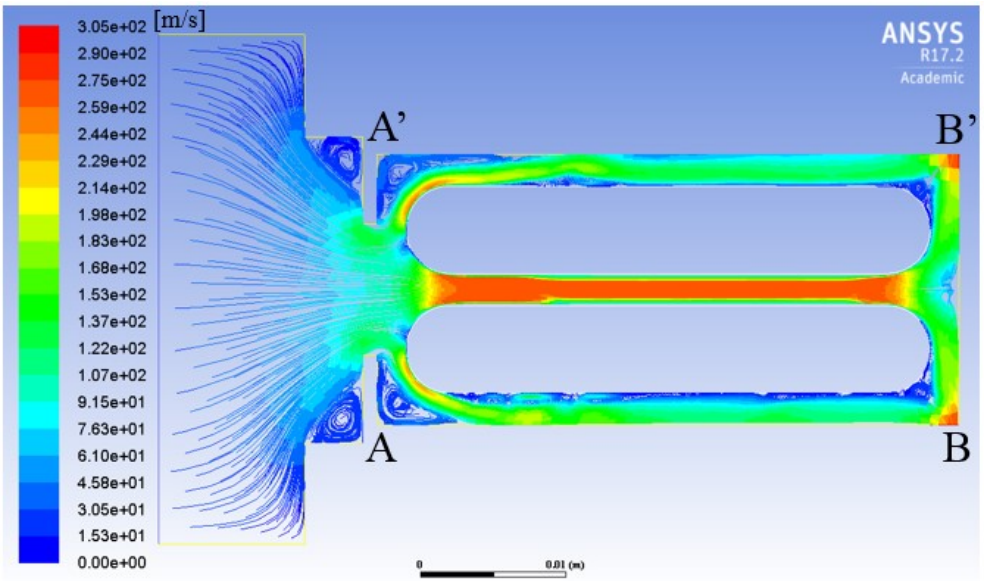

Fig. A.5 BLDC air velocity pathline plot computed with ANSYS®.

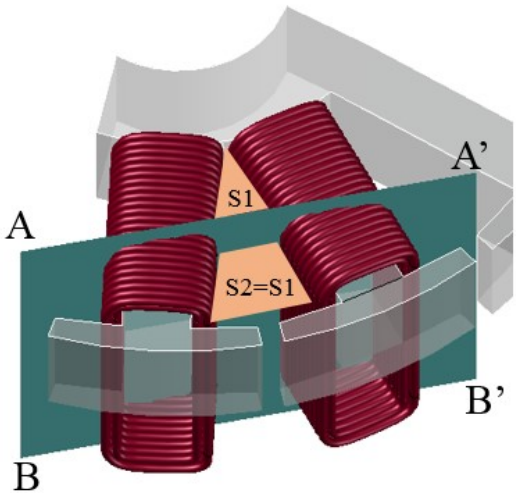

Fig. A.6 Cross sectional area considered for the CFD computation.

As outcome of the CFD analysis, the (surface average) convection heat transfer coefficients have been calculated and they are listed in Table A.1. The coefficient h_{tooth} was not computed through CFD and its value has been assumed conservatively equal to $h_{act.}$ Since the machine is not impregnated, the windings' thermal conductivity in the radial direction is set to 1.5 W/m/K, while in the axial direction it is equal to 400 W/m/K (i.e. pure copper). The heat axially flowing through the iron lamination stack is neglected, because the lamination thermal conduction coefficient in the axial direction is two orders of magnitude lower than the copper one.

Table A.1 – Convection heat transfer coefficients from CFD.

Heat transfer coeff.	**Value [W/m^2/K]**
h_{DE}	279.8
h_{NDE}	231.6
h_{act}	104.8
h_{tooth}	104.8